

Dihadron azimuthal correlations in Au+Au collisions at $\sqrt{s_{NN}} = 200$ GeV

A. Adare,⁸ S. Afanasiev,²² C. Aidala,⁹ N.N. Ajitanand,⁴⁹ Y. Akiba,^{43,44} H. Al-Bataineh,³⁸ J. Alexander,⁴⁹ A. Al-Jamel,³⁸ K. Aoki,^{28,43} L. Aphecetche,⁵¹ R. Armendariz,³⁸ S.H. Aronson,³ J. Asai,⁴⁴ E.T. Atomssa,²⁹ R. Averbeck,⁵⁰ T.C. Awes,³⁹ B. Azmoun,³ V. Babintsev,¹⁸ G. Baksay,¹⁴ L. Baksay,¹⁴ A. Baldissieri,¹¹ K.N. Barish,⁴ P.D. Barnes,³¹ B. Bassalleck,³⁷ S. Bathe,⁴ S. Batsouli,^{9,39} V. Baublis,⁴² F. Bauer,⁴ A. Bazilevsky,³ S. Belikov,^{3,21,*} R. Bennett,⁵⁰ Y. Berdnikov,⁴⁶ A.A. Bickley,⁸ M.T. Bjornndal,⁹ J.G. Boissevain,³¹ H. Borel,¹¹ K. Boyle,⁵⁰ M.L. Brooks,³¹ D.S. Brown,³⁸ D. Bucher,³⁴ H. Buesching,³ V. Bumazhnov,¹⁸ G. Bunce,^{3,44} J.M. Burward-Hoy,³¹ S. Butsyk,^{31,50} S. Campbell,⁵⁰ J.-S. Chai,²³ B.S. Chang,⁵⁸ J.-L. Charvet,¹¹ S. Chernichenko,¹⁸ J. Chiba,²⁴ C.Y. Chi,⁹ M. Chiu,^{9,19} I.J. Choi,⁵⁸ T. Chujo,⁵⁵ P. Chung,⁴⁹ A. Churnyn,¹⁸ V. Cianciolo,³⁹ C.R. Clevelin,¹⁶ Y. Cobigo,¹¹ B.A. Cole,⁹ M.P. Comets,⁴⁰ P. Constantin,^{21,31} M. Csanád,¹³ T. Csörgő,²⁵ T. Dahms,⁵⁰ K. Das,¹⁵ G. David,³ M.B. Deaton,¹ K. Dehmelt,¹⁴ H. Delagrangé,⁵¹ A. Denisov,¹⁸ D. d'Enterria,⁹ A. Deshpande,^{44,50} E.J. Desmond,³ O. Dietzsch,⁴⁷ A. Dion,⁵⁰ M. Donadelli,⁴⁷ J.L. Drachenberg,¹ O. Drapier,²⁹ A. Drees,⁵⁰ A.K. Dubey,⁵⁷ A. Durum,¹⁸ V. Dzhordzhadze,^{4,52} Y.V. Efremenko,³⁹ J. Egdemir,⁵⁰ F. Ellinghaus,⁸ W.S. Emam,⁴ A. Enokizono,^{17,30} H. En'yo,^{43,44} B. Espagnon,⁴⁰ S. Esumi,⁵⁴ K.O. Eyser,⁴ D.E. Fields,^{37,44} M. Finger,^{5,22} M. Finger, Jr.,^{5,22} F. Fleuret,²⁹ S.L. Fokin,²⁷ B. Forestier,³² Z. Fraenkel,⁵⁷ J.E. Frantz,^{9,50} A. Franz,³ A.D. Frawley,¹⁵ K. Fujiwara,⁴³ Y. Fukao,^{28,43} S.-Y. Fung,⁴ T. Fusayasu,³⁶ S. Gadrat,³² I. Garishvili,⁵² F. Gastineau,⁵¹ M. Germain,⁵¹ A. Glenn,^{8,52} H. Gong,⁵⁰ M. Gonin,²⁹ J. Gosset,¹¹ Y. Goto,^{43,44} R. Granier de Cassagnac,²⁹ N. Grau,²¹ S.V. Greene,⁵⁵ M. Grosse Perdekamp,^{19,44} T. Gunji,⁷ H.-Å. Gustafsson,³³ T. Hachiya,^{17,43} A. Hadj Henmi,⁵¹ C. Haegemann,³⁷ J.S. Haggerty,³ M.N. Hagiwara,¹ H. Hamagaki,⁷ R. Han,⁴¹ H. Harada,¹⁷ E.P. Hartouni,³⁰ K. Haruna,¹⁷ M. Harvey,³ E. Haslum,³³ K. Hasuko,⁴³ R. Hayano,⁷ M. Heffner,³⁰ T.K. Hemmick,⁵⁰ T. Hester,⁴ J.M. Heuser,⁴³ X. He,¹⁶ H. Hiejima,¹⁹ J.C. Hill,²¹ R. Hobbs,³⁷ M. Hohlmann,¹⁴ M. Holmes,⁵⁵ W. Holzmann,⁴⁹ K. Homma,¹⁷ B. Hong,²⁶ T. Horaguchi,^{43,53} D. Hornback,⁵² M.G. Hur,²³ T. Ichihara,^{43,44} K. Imai,^{28,43} M. Inaba,⁵⁴ Y. Inoue,^{45,43} D. Isenhowe,¹ L. Isenhowe,¹ M. Ishihara,⁴³ T. Isobe,⁷ M. Issah,⁴⁹ A. Isupov,²² B.V. Jacak,^{50,†} J. Jia,⁹ J. Jin,⁹ O. Jinnouchi,⁴⁴ B.M. Johnson,³ K.S. Joo,³⁵ D. Jouan,⁴⁰ F. Kajihara,^{7,43} S. Kametani,^{7,56} N. Kamihara,^{43,53} J. Kamin,⁵⁰ M. Kaneta,⁴⁴ J.H. Kang,⁵⁸ H. Kanou,^{43,53} T. Kawagishi,⁵⁴ D. Kwall,⁴⁴ A.V. Kazantsev,²⁷ S. Kelly,⁸ A. Khanzadeev,⁴² J. Kikuchi,⁵⁶ D.H. Kim,³⁵ D.J. Kim,⁵⁸ E. Kim,⁴⁸ Y.-S. Kim,²³ E. Kinney,⁸ A. Kiss,¹³ E. Kistenev,³ A. Kiyomichi,⁴³ J. Klay,³⁰ C. Klein-Boesing,³⁴ L. Kochenda,⁴² V. Kochetkov,¹⁸ B. Komkov,⁴² M. Konno,⁵⁴ D. Kotchetkov,⁴ A. Kozlov,⁵⁷ A. Král,¹⁰ A. Kravitz,⁹ P.J. Kroon,³ J. Kubart,^{5,20} G.J. Kunde,³¹ N. Kurihara,⁷ K. Kurita,^{45,43} M.J. Kweon,²⁶ Y. Kwon,^{52,58} G.S. Kyle,³⁸ R. Lacey,⁴⁹ Y.-S. Lai,⁹ J.G. Lajoie,²¹ A. Lebedev,²¹ Y. Le Bornec,⁴⁰ S. Leckey,⁵⁰ D.M. Lee,³¹ M.K. Lee,⁵⁸ T. Lee,⁴⁸ M.J. Leitch,³¹ M.A.L. Leite,⁴⁷ B. Lenzi,⁴⁷ H. Lim,⁴⁸ T. Liška,¹⁰ A. Litvinenko,²² M.X. Liu,³¹ X. Li,⁶ X.H. Li,⁴ B. Love,⁵⁵ D. Lynch,³ C.F. Maguire,⁵⁵ Y.I. Makdisi,³ A. Malakhov,²² M.D. Malik,³⁷ V.I. Manko,²⁷ Y. Mao,^{41,43} L. Mašek,^{5,20} H. Masui,⁵⁴ F. Matathias,^{9,50} M.C. McCain,¹⁹ M. McCumber,⁵⁰ P.L. McGaughey,³¹ Y. Miake,⁵⁴ P. Mikeš,^{5,20} K. Miki,⁵⁴ T.E. Miller,⁵⁵ A. Milov,⁵⁰ S. Mioduszewski,³ G.C. Mishra,¹⁶ M. Mishra,² J.T. Mitchell,³ M. Mitrovski,⁴⁹ A. Morreale,⁴ D.P. Morrison,³ J.M. Moss,³¹ T.V. Moukhanova,²⁷ D. Mukhopadhyay,⁵⁵ J. Murata,^{45,43} S. Nagamiya,²⁴ Y. Nagata,⁵⁴ J.L. Nagle,⁸ M. Naglis,⁵⁷ I. Nakagawa,^{43,44} Y. Nakamiya,¹⁷ T. Nakamura,¹⁷ K. Nakano,^{43,53} J. Newby,³⁰ M. Nguyen,⁵⁰ B.E. Norman,³¹ A.S. Nyanin,²⁷ J. Nystrand,³³ E. O'Brien,³ S.X. Oda,⁷ C.A. Ogilvie,²¹ H. Ohnishi,⁴³ I.D. Ojha,⁵⁵ H. Okada,^{28,43} K. Okada,⁴⁴ M. Oka,⁵⁴ O.O. Omiwade,¹ A. Oskarsson,³³ I. Otterlund,³³ M. Ouchida,¹⁷ K. Ozawa,⁷ R. Pak,³ D. Pal,⁵⁵ A.P.T. Palounek,³¹ V. Pantuev,⁵⁰ V. Papavassiliou,³⁸ J. Park,⁴⁸ W.J. Park,²⁶ S.F. Pate,³⁸ H. Pei,²¹ J.-C. Peng,¹⁹ H. Pereira,¹¹ V. Peresedov,²² D.Yu. Peressounko,²⁷ C. Pinkenburg,³ R.P. Pisani,³ M.L. Purschke,³ A.K. Purwar,^{31,50} H. Qu,¹⁶ J. Rak,^{21,37} A. Rakotozafindrabe,²⁹ I. Ravinovich,⁵⁷ K.F. Read,^{39,52} S. Rembeczki,¹⁴ M. Reuter,⁵⁰ K. Reygers,³⁴ V. Riabov,⁴² Y. Riabov,⁴² G. Roche,³² A. Romana,^{29,*} M. Rosati,²¹ S.S.E. Rosendahl,³³ P. Rosnet,³² P. Rukoyatkin,²² V.L. Rykov,⁴³ S.S. Ryu,⁵⁸ B. Sahlmueller,³⁴ N. Saito,^{28,43,44} T. Sakaguchi,^{3,7,56} S. Sakai,⁵⁴ H. Sakata,¹⁷ V. Samsonov,⁴² H.D. Sato,^{28,43} S. Sato,^{3,24,54} S. Sawada,²⁴ J. Seele,⁸ R. Seidl,¹⁹ V. Semenov,¹⁸ R. Seto,⁴ D. Sharma,⁵⁷ T.K. Shea,³ I. Shein,¹⁸ A. Shevel,^{42,49} T.-A. Shibata,^{43,53} K. Shigaki,¹⁷ M. Shimomura,⁵⁴ T. Shohjoh,⁵⁴ K. Shoji,^{28,43} A. Sickles,⁵⁰ C.L. Silva,⁴⁷ D. Silvermyr,³⁹ C. Silvestre,¹¹ K.S. Sim,²⁶ C.P. Singh,² V. Singh,² S. Skutnik,²¹ M. Slunečka,^{5,22} W.C. Smith,¹ A. Soldatov,¹⁸ R.A. Soltz,³⁰ W.E. Sondheim,³¹ S.P. Sorensen,⁵² I.V. Sourikova,³ F. Staley,¹¹ P.W. Stankus,³⁹ E. Stenlund,³³ M. Stepanov,³⁸ A. Ster,²⁵ S.P. Stoll,³ T. Sugitate,¹⁷ C. Suire,⁴⁰ J.P. Sullivan,³¹ J. Sziklai,²⁵ T. Tabaru,⁴⁴ S. Takagi,⁵⁴ E.M. Takagui,⁴⁷ A. Taketani,^{43,44} K.H. Tanaka,²⁴ Y. Tanaka,³⁶ K. Tanida,^{43,44} M.J. Tannenbaum,³ A. Taranenko,⁴⁹ P. Tarján,¹² T.L. Thomas,³⁷ M. Togawa,^{28,43} A. Toia,⁵⁰ J. Tojo,⁴³ L. Tomášek,²⁰ H. Torii,⁴³ R.S. Towell,¹ V.-N. Tram,²⁹ I. Tserruya,⁵⁷ Y. Tsuchimoto,^{17,43} S.K. Tuli,² H. Tydesjö,³³ N. Tyurin,¹⁸ C. Vale,²¹ H. Valle,⁵⁵ H.W. van Hecke,³¹

J. Velkovska,⁵⁵ R. Vertesi,¹² A.A. Vinogradov,²⁷ M. Virius,¹⁰ V. Vrba,²⁰ E. Vznuzdaev,⁴² M. Wagner,^{28,43} D. Walker,⁵⁰ X.R. Wang,³⁸ Y. Watanabe,^{43,44} J. Wessels,³⁴ S.N. White,³ N. Willis,⁴⁰ D. Winter,⁹ C.L. Woody,³ M. Wysocki,⁸ W. Xie,^{4,44} Y.L. Yamaguchi,⁵⁶ A. Yanovich,¹⁸ Z. Yasin,⁴ J. Ying,¹⁶ S. Yokkaichi,^{43,44} G.R. Young,³⁹ I. Younus,³⁷ I.E. Yushmanov,²⁷ W.A. Zajc,⁹ O. Zaudtke,³⁴ C. Zhang,^{9,39} S. Zhou,⁶ J. Zimányi,^{25,*} and L. Zolin²²

(PHENIX Collaboration)

¹Abilene Christian University, Abilene, TX 79699, USA

²Department of Physics, Banaras Hindu University, Varanasi 221005, India

³Brookhaven National Laboratory, Upton, NY 11973-5000, USA

⁴University of California - Riverside, Riverside, CA 92521, USA

⁵Charles University, Ovocný trh 5, Praha 1, 116 36, Prague, Czech Republic

⁶China Institute of Atomic Energy (CIAE), Beijing, People's Republic of China

⁷Center for Nuclear Study, Graduate School of Science, University of Tokyo, 7-3-1 Hongo, Bunkyo, Tokyo 113-0033, Japan

⁸University of Colorado, Boulder, CO 80309, USA

⁹Columbia University, New York, NY 10027 and Nevis Laboratories, Irvington, NY 10533, USA

¹⁰Czech Technical University, Zikova 4, 166 36 Prague 6, Czech Republic

¹¹Dapnia, CEA Saclay, F-91191, Gif-sur-Yvette, France

¹²Debrecen University, H-4010 Debrecen, Egyetem tér 1, Hungary

¹³ELTE, Eötvös Loránd University, H - 1117 Budapest, Pázmány P. s. 1/A, Hungary

¹⁴Florida Institute of Technology, Melbourne, FL 32901, USA

¹⁵Florida State University, Tallahassee, FL 32306, USA

¹⁶Georgia State University, Atlanta, GA 30303, USA

¹⁷Hiroshima University, Kagamiyama, Higashi-Hiroshima 739-8526, Japan

¹⁸IHEP Protvino, State Research Center of Russian Federation, Institute for High Energy Physics, Protvino, 142281, Russia

¹⁹University of Illinois at Urbana-Champaign, Urbana, IL 61801, USA

²⁰Institute of Physics, Academy of Sciences of the Czech Republic, Na Slovance 2, 182 21 Prague 8, Czech Republic

²¹Iowa State University, Ames, IA 50011, USA

²²Joint Institute for Nuclear Research, 141980 Dubna, Moscow Region, Russia

²³KAERI, Cyclotron Application Laboratory, Seoul, Korea

²⁴KEK, High Energy Accelerator Research Organization, Tsukuba, Ibaraki 305-0801, Japan

²⁵KFKI Research Institute for Particle and Nuclear Physics of the Hungarian Academy of Sciences (MTA KFKI RMKI), H-1525 Budapest 114, POBox 49, Budapest, Hungary

²⁶Korea University, Seoul, 136-701, Korea

²⁷Russian Research Center "Kurchatov Institute", Moscow, Russia

²⁸Kyoto University, Kyoto 606-8502, Japan

²⁹Laboratoire Leprince-Ringuet, Ecole Polytechnique, CNRS-IN2P3, Route de Saclay, F-91128, Palaiseau, France

³⁰Lawrence Livermore National Laboratory, Livermore, CA 94550, USA

³¹Los Alamos National Laboratory, Los Alamos, NM 87545, USA

³²LPC, Université Blaise Pascal, CNRS-IN2P3, Clermont-Fd, 63177 Aubiere Cedex, France

³³Department of Physics, Lund University, Box 118, SE-221 00 Lund, Sweden

³⁴Institut für Kernphysik, University of Muenster, D-48149 Muenster, Germany

³⁵Myongji University, Yongin, Kyonggido 449-728, Korea

³⁶Nagasaki Institute of Applied Science, Nagasaki-shi, Nagasaki 851-0193, Japan

³⁷University of New Mexico, Albuquerque, NM 87131, USA

³⁸New Mexico State University, Las Cruces, NM 88003, USA

³⁹Oak Ridge National Laboratory, Oak Ridge, TN 37831, USA

⁴⁰IPN-Orsay, Université Paris Sud, CNRS-IN2P3, BP1, F-91406, Orsay, France

⁴¹Peking University, Beijing, People's Republic of China

⁴²PNPI, Petersburg Nuclear Physics Institute, Gatchina, Leningrad region, 188300, Russia

⁴³RIKEN, The Institute of Physical and Chemical Research, Wako, Saitama 351-0198, Japan

⁴⁴RIKEN BNL Research Center, Brookhaven National Laboratory, Upton, NY 11973-5000, USA

⁴⁵Physics Department, Rikkyo University, 3-34-1 Nishi-Ikebukuro, Toshima, Tokyo 171-8501, Japan

⁴⁶Saint Petersburg State Polytechnic University, St. Petersburg, Russia

⁴⁷Universidade de São Paulo, Instituto de Física, Caixa Postal 66318, São Paulo CEP05315-970, Brazil

⁴⁸System Electronics Laboratory, Seoul National University, Seoul, Korea

⁴⁹Chemistry Department, Stony Brook University, Stony Brook, SUNY, NY 11794-3400, USA

⁵⁰Department of Physics and Astronomy, Stony Brook University, SUNY, Stony Brook, NY 11794, USA

⁵¹SUBATECH (Ecole des Mines de Nantes, CNRS-IN2P3, Université de Nantes) BP 20722 - 44307, Nantes, France

⁵²University of Tennessee, Knoxville, TN 37996, USA

⁵³Department of Physics, Tokyo Institute of Technology, Oh-okayama, Meguro, Tokyo 152-8551, Japan

⁵⁴Institute of Physics, University of Tsukuba, Tsukuba, Ibaraki 305, Japan

⁵⁵Vanderbilt University, Nashville, TN 37235, USA

⁵⁶Waseda University, Advanced Research Institute for Science and Engineering, 17 Kikui-cho, Shinjuku-ku, Tokyo 162-0044, Japan

⁵⁷Weizmann Institute, Rehovot 76100, Israel

⁵⁸Yonsei University, IPAP, Seoul 120-749, Korea

(Dated: February 3, 2008)

Azimuthal angle ($\Delta\phi$) correlations are presented for a broad range of transverse momentum ($0.4 < p_T < 10$ GeV/c) and centrality (0-92%) selections for charged hadrons from di-jets in Au+Au collisions at $\sqrt{s_{NN}} = 200$ GeV. With increasing p_T , the away-side $\Delta\phi$ distribution evolves from a broad and relatively flat shape to a concave shape, then to a convex shape. Comparisons to $p + p$ data suggest that the away-side distribution can be divided into a partially suppressed “head” region centered at $\Delta\phi \sim \pi$, and an enhanced “shoulder” region centered at $\Delta\phi \sim \pi \pm 1.1$. The p_T spectrum for the associated hadrons in the head region softens toward central collisions. The spectral slope for the shoulder region is independent of centrality and trigger p_T . The properties of the near-side distributions are also modified relative to those in $p + p$ collisions, reflected by the broadening of the jet shape in $\Delta\phi$ and $\Delta\eta$, and an enhancement of the per-trigger yield. However, these modifications seem to be limited to $p_T \lesssim 4$ GeV/c, above which both the hadron pair shape and per-trigger yield become similar to $p + p$ collisions. These observations suggest that both the away- and near-side distributions contain a jet fragmentation component which dominates for $p_T \gtrsim 5$ GeV and a medium-induced component which is important for $p_T \lesssim 4$ GeV/c. We also quantify the role of jets at intermediate and low p_T through the yield of jet-induced pairs in comparison to binary scaled $p + p$ pair yield. The yield of jet-induced pairs is suppressed at high pair proxy energy (sum of the p_T magnitudes of the two hadrons) and is enhanced at low pair proxy energy. The former is consistent with jet quenching; the latter is consistent with the enhancement of soft hadron pairs due to transport of lost energy to lower p_T .

PACS numbers: 25.75.Dw

Contents		
I. INTRODUCTION	3	A. Insights from Identified Particle and Energy Dependent Correlations 24
		B. Comparison with models 24
II. JET AZIMUTHAL CORRELATIONS	4	VI. SUMMARY AND CONCLUSIONS 25
III. EXPERIMENTAL ANALYSIS	6	VII. ACKNOWLEDGEMENTS 26
A. Dataset and Centrality	6	A. DIHADRON CORRELATION METHOD 26
B. Tracking and Background Estimation	6	B. THE ROLE OF REACTION PLANE 27
C. Jet Signal Extraction	7	C. SIMULATION STUDY OF THE NON-FLOW EFFECT FROM JETS 28
D. Elliptic Flow Measurement	8	
E. Combinatoric Background Subtraction	9	D. COMPREHENSIVE DATA PLOTS AND DATA TABLES 29
F. Systematic Uncertainties	11	References 43
IV. RESULTS	11	
A. Jet-induced Dihadron Azimuthal ($\Delta\phi$) Distributions	11	
B. Medium Modification of Away-side Jets	12	
1. Away-side jet shape	12	
2. Away-side jet per-trigger yield	14	
C. Medium Modification of Near-side Jets	16	
1. Near-side jet shape	16	
2. Near-side jet per-trigger yield	17	
D. Away- and Near-side Spectral Slopes	19	
E. Medium Modification of Hadron Pair Yield	21	
V. DISCUSSION	24	

*Deceased

†PHENIX Spokesperson: jacak@skipper.physics.sunysb.edu

High transverse momentum (p_T) partons are informative probes of the high energy density matter created in nuclear collisions at the Relativistic Heavy-Ion Collider (RHIC). These partons lose a large fraction of their energy in the matter prior to forming final state hadrons. Such an energy loss is predicted to lead to a reduction of both single hadron and correlated dihadron yields at high p_T [1, 2, 3], a phenomenon known as jet-quenching. Indeed, current results for high p_T have revealed a strong

suppression of inclusive hadron yields [5, 6, 7], as well as the suppression of correlated away-side hadron pairs [8].

Despite this strong suppression, particle production for $p_T \gtrsim 5$ GeV/ c appears to have a significant contribution from in-vacuum jet fragmentation. This is suggested by a p_T -independent suppression factor for single hadrons [4, 5, 6, 7], which implies a p -like power law spectral shape in Au+Au collisions, and similar π^0 to η meson [9, 10] and proton to pion [7, 11] ratios between Au+Au and p + p collisions. More direct evidence has been provided by high- p_T dihadron azimuthal angle ($\Delta\phi$) correlations measurements. In particular, our current measurements, as well as prior ones [12, 13], reveal characteristic jet-like peaks for the near-side ($\Delta\phi \sim 0$) and the away-side ($\Delta\phi \sim \pi$) at high p_T .

In most energy loss models, the stopping power of the medium is normally characterized by the transport coefficient \hat{q} , defined as the squared average momentum transfer from the medium to the hard parton per unit path length. However, due to the steeply falling parton spectra and strong jet quenching, the observed high- p_T single hadrons and hadron pairs mainly come from (di)jets that suffer minimal interaction with the medium. Thus, the overall suppression factor is sensitive to the full energy loss probability distribution instead of just the average energy loss itself. In fact, simple calculations [14] with different energy loss probability distributions have been shown to match the data quite well. However, the extracted $\langle\hat{q}\rangle$ values are sensitive to the theoretical models and their associated assumptions [15]. Additional experimental constraints on the dynamics of the energy loss processes are clearly needed.

In order to improve our understanding of the parton-medium interactions, it is important to study the fate of partons that suffer energy loss in the medium. These partons are quenched by the medium and their energy is believed to be transported to lower- p_T hadrons ($p_T \lesssim 4$ GeV/ c). Prior measurements [8, 16, 17, 18, 19, 20] in this p_T region, as well as the present study, indicate strong modifications of the near- and the away-side $\Delta\phi$ distributions. The near-side jet-induced pairs peak at $\Delta\phi \sim 0$, but the peak is broadened and enhanced with respect to $p + p$ collisions. The away-side jet-induced pairs are observed to peak at $\Delta\phi \sim \pi \pm 1.1$ [13, 18, 19] with a local minimum at $\Delta\phi \sim \pi$. These modification patterns reflect characteristics of the energy transport of the quenched partons in both p_T and $\Delta\phi$. Many mechanisms for this energy transport have been proposed for the near-side [21, 22, 23, 24, 25, 26, 27, 28] and away-side [23, 24, 25, 29, 30, 31, 32, 33, 34, 35, 36].

Such energy transport is expected to enhance jet contributions to the production of low- p_T hadrons. However, jet-induced hadron pair correlations can be affected by soft processes such as hydrodynamical flow [37] and quark coalescence [38, 39, 40, 41], which dominate the hadron production in the intermediate p_T region. The coupling of partons with hydrodynamical flow could modify the jet shape and yield. Similarly, quark coalescence could

modify the particle composition in the near- and away-side jets [42, 43]. Therefore, detailed correlation studies for $p_T \lesssim 4$ GeV/ c can improve our knowledge of the interplay between soft and hard processes for hadron production.

In this paper we present a detailed survey of the trigger p_T , partner p_T and centrality dependence of the near- and away-side jet shapes and yields from Au+Au collisions. These measurements provide a comprehensive overview of the different physical features that come into play for different p_T ranges, and provide new insights on the interplay between the processes leading to jet energy loss and the response of the medium to the lost energy. In addition, they allow a detailed study of the similarities and differences between the correlation patterns for the near- and away-side jets. When coupled with inclusive hadron production, these measurements also allow quantification of the role of jets at intermediate p_T , where the particle production is believed to be dominated by the soft processes.

The results reported here comprise significant extensions to results published earlier [13, 19]. In Section II, we introduce variables used to quantify the jet properties and their in-medium modifications. In Section III, we present data analysis details, jet signal extraction and background subtraction, and several sources of systematic errors related to the measurements. The main results are presented in Section IV and model comparisons and discussions are given in Section V. Several technical issues related to the correlation analysis are addressed in Appendices A-C, and tabulated data are given in Appendix D.

II. JET AZIMUTHAL CORRELATIONS

The defining characteristic of a jet is the collimated production of hadrons in the direction of a fragmenting parton. Traditionally, such energetic jets have been identified using standard jet reconstruction algorithms. However, direct jet reconstruction in heavy ion collisions is difficult due to the large amount of soft background. Measurements in a relatively limited acceptance also pose additional challenges because of a possible leakage of the jet fragments outside of the detectors acceptance.

The two-particle (dihadron) relative azimuthal angle ($\Delta\phi$) correlation technique provides an alternative approach for accessing the properties of jets. Two classes of hadrons, trigger hadrons (denoted as type a) and partner hadrons (denoted as type b), typically from different p_T ranges, are correlated with each other. Jet properties are extracted on a statistical basis from the $\Delta\phi$ distribution built of many events. This approach overcomes problems due to background and limited acceptance, and allows the study of jets to be extended to low p_T where soft processes dominate.

To leading order in QCD, high- p_T jets are produced back-to-back in azimuth. This back-to-back correlation

is, however, smeared by the fragmentation process and initial and final state radiation, to give a characteristic $\Delta\phi$ distribution schematically shown in Fig. 1 [44]. Hadron pairs from the same jet (near-side) dominates at $\Delta\phi = \phi^a - \phi^b \sim 0$ and those from back-to-back dijets (away-side) tend to appear at $\Delta\phi \sim \pi$.

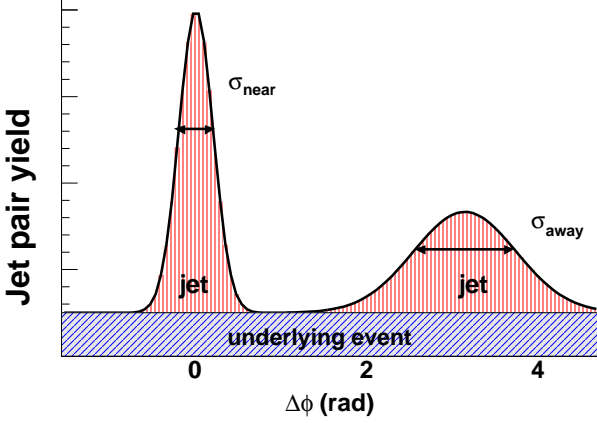


FIG. 1: (Color online) Cartoon of hadron pair distribution in $\Delta\phi$ for $p + p$ collisions. It has two peaks corresponding to near- and away-side jet, and a flat component representing the underlying event pairs.

Two observables which are commonly exploited in di-hadron correlation studies are the hadron-pair yield (the rate of jet-induced hadron pairs per-event, JPY) and the per-trigger yield (jet-induced hadron-pair yield divided by trigger yield, $Y_{\text{jet_ind}}$) in a given event sample. The former is related to the two-particle cross-section for jet production; the latter is related to the ratio of the two-particle to single-particle cross-sections:

$$\begin{aligned} \text{JPY}(p_T^a, p_T^b, \Delta\phi) &\equiv \frac{1}{N_{\text{evts}}} \frac{d^3 N^{ab}}{dp_T^a dp_T^b d\Delta\phi} \\ &= \frac{1}{\sigma_{\text{tot}}} \frac{d^3 \sigma_{\text{jet_ind}}}{dp_T^a dp_T^b d\Delta\phi}, \end{aligned} \quad (1)$$

$$\begin{aligned} Y_{\text{jet_ind}}(p_T^a, p_T^b, \Delta\phi) &\equiv \text{JPY}(p_T^a, p_T^b, \Delta\phi) \Big/ \frac{dN^a}{N_{\text{evts}} dp_T^a} \\ &= \frac{d^3 \sigma_{\text{jet_ind}}}{dp_T^a dp_T^b d\Delta\phi} \Big/ \frac{d\sigma}{dp_T^a}, \end{aligned} \quad (2)$$

where N^{ab} is the number of jet-induced hadron pairs, N_{evts} is the number of events and σ_{tot} is the semi-inclusive cross-section for that event sample. Thus, JPY is simply the product of the per-trigger yield and the number of triggers. To first order, the two-particle cross-section for the near-side jet is governed by the di-hadron fragmentation function. By contrast, the cross-section for the away-side jet is governed by two independent fragmentation functions, i.e one parton produces a hadron with p_T^a and the other scattered parton produces a hadron with p_T^b .

In A+A collisions, the single and dihadron cross-sections can be modified by the medium. This modification can be quantified by comparing the yield in A+A collisions to that for $p + p$ collisions. Thus, modification to the single hadron cross-section is characterized by the nuclear modification factor, R_{AA}

$$R_{AA}(p_T) = \frac{1/\sigma_{A+A} d\sigma^{A+A}/dp_T}{\langle N_{\text{coll}} \rangle / \sigma_{p+p} d\sigma^{p+p}/dp_T} \quad (3)$$

where σ_{A+A} and σ_{p+p} are the semi-inclusive cross-section in A+A and $p + p$ collisions, respectively. $\langle N_{\text{coll}} \rangle$ is the average number of binary collisions for a given centrality selection in A+A collisions. Modification of the dihadron cross-section can be characterized by J_{AA} , which is defined as,

$$\begin{aligned} J_{AA}(p_T^a, p_T^b, \Delta\phi) &= \frac{\text{JPY}^{A+A}}{\langle N_{\text{coll}} \rangle \text{JPY}^{p+p}} \\ &= \frac{1}{\sigma_{A+A}} \frac{d^3 \sigma_{\text{jet_ind}}^{A+A}}{dp_T^a dp_T^b d\Delta\phi} \Big/ \frac{\langle N_{\text{coll}} \rangle}{\sigma_{p+p}} \frac{d^3 \sigma_{\text{jet_ind}}^{p+p}}{dp_T^a dp_T^b d\Delta\phi} \end{aligned} \quad (4)$$

In the absence of nuclear effects, both the single and dihadron cross-sections from jets are expected to scale with $\langle N_{\text{coll}} \rangle$. Therefore, R_{AA} and J_{AA} should be equal to unity.

The medium modifications of jets are also characterized by the per-trigger yield and its corresponding modification factor, I_{AA} .

$$I_{AA}(p_T^a, p_T^b) = \frac{Y_{\text{jet_ind}}^{A+A}(p_T^a, p_T^b)}{Y_{\text{jet_ind}}^{p+p}(p_T^a, p_T^b)}. \quad (5)$$

In general, the value of I_{AA} depends on modifications to both the hadron-pair yield and the trigger yield. For high- p_T correlation measurements, the per-trigger yield is a convenient choice since each jet typically produces at most one high- p_T trigger. Because of the steeply falling parton spectrum, the probability of having a high- p_T parton that produces multiple trigger hadrons is small. Thus the per-trigger yield effectively represents the per-jet yield in $p + p$ collisions, and I_{AA} represents the modification of the partner yield per-jet. For intermediate and low p_T , however, jet fragmentation is not the only source of triggers, and this can lead to an artificial reduction of the per-trigger yield (see discussion in Section IV.E). For such situations, J_{AA} is a more robust variable for correlation analysis since it is only sensitive to the modification of jet-induced hadron pairs.

JPY and J_{AA} are symmetric with respect to p_T^a and p_T^b . By contrast, the per-trigger yield and I_{AA} are not, due to the appearance of the normalization factor N^a in Eq. 2. This normalization factor is the only distinction between triggers and the partners in this analysis. In addition, JPY can be expressed in terms of the per-trigger yield and the inclusive yield as

$$\text{JPY}(p_T^a, p_T^b) = Y_{\text{jet_ind}}(p_T^a, p_T^b) \frac{dN^a}{N_{\text{evts}} dp_T^a} \quad (6)$$

$$= Y_{\text{jet_ind}}(p_T^b, p_T^a) \frac{dN^b}{N_{\text{evts}} dp_T^b}$$

Similarly, J_{AA} can be expressed in terms of R_{AA} and I_{AA} as

$$\begin{aligned} J_{AA}(p_T^a, p_T^b) &= I_{AA}(p_T^a, p_T^b) R_{AA}(p_T^a) \\ &= I_{AA}(p_T^b, p_T^a) R_{AA}(p_T^b) \end{aligned} \quad (7)$$

Thus, $I_{AA}(p_T^b, p_T^a)$ can be calculated from $I_{AA}(p_T^a, p_T^b)$, $R_{AA}(p_T^a)$ and $R_{AA}(p_T^b)$.

In the current analysis, the in-medium modifications of the jet shape and yield are characterized via comparisons of the per-trigger yield and hadron-pair yield in Au+Au and $p+p$ collisions i.e. via I_{AA} and J_{AA} . As discussed earlier, these quantities are defined in their differential form in $\Delta\phi$, p_T^a and p_T^b . Operationally, this means that the hadron-pair yields and the per-trigger yields are measured in a finite p_T range and/or integrated over a limited $\Delta\phi$ range. I_{AA} and J_{AA} are then obtained from these integrated yields.

III. EXPERIMENTAL ANALYSIS

A. Dataset and Centrality

The results presented in this article are based on three datasets collected with the PHENIX detector [45] at $\sqrt{s_{NN}}=200$ GeV, during the 2004-2005 RHIC running periods. The first is comprised of a minimum-bias (MB) Au+Au dataset triggered by the Beam-Beam Counters (BBC) and the Zero-Degree Calorimeters (ZDC) and taken in 2004. The second is a MB $p+p$ dataset triggered by the BBC and taken in 2005, and the third is a level-1 triggered (LVL1) $p+p$ dataset also obtained in 2005. The level-1 trigger requirement is an energy threshold of 1.4 GeV in 4×4 electromagnetic calorimeter (EMC) towers in coincidence with the BBC trigger [46]. The MB and LVL1 $p+p$ datasets serve as baseline measurements for the Au+Au dataset; they are used to select triggers for $p_T < 5$ and $p_T > 5$ GeV/ c , respectively.

The collision vertex along the beam direction, z , was measured by the BBCs. After an offline vertex cut of $|z| < 30$ cm and selecting good runs, a total of 840 million or $136 \mu\text{b}^{-1}$ Au+Au events were obtained. This is a factor $\times 30$ higher than obtained in a previous analysis [18]. The total statistics for MB $p+p$ and LVL1 $p+p$ datasets are equivalent to 73nb^{-1} and 2.5pb^{-1} sampled luminosities respectively.

The event centrality was determined via cuts in the space of BBC charge versus ZDC energy [47]. The efficiency of the MB triggered events is estimated to be $92.2^{+2.5}_{-3.0}\%$ of the total Au+Au inelastic cross section (6.9 barn) [7]. To optimize the p_T reach of our results, relatively *coarse* centrality selections of 0-20%, 20-40%, 40-60%, 60-92.2% were chosen. However for $p_T < 4$ GeV/ c ,

TABLE I: Average number of nucleon-nucleon collisions $\langle N_{\text{coll}} \rangle$ and participant nucleons $\langle N_{\text{part}} \rangle$ for several centrality classes. $\langle N_{\text{coll}} \rangle$ and $\langle N_{\text{part}} \rangle$ are obtained from a Glauber Monte-Carlo simulation of the response of the BBC and ZDC in Au+Au collisions at $\sqrt{s_{NN}} = 200$ GeV. The errors for these centrality classes are correlated.

Centrality	$\langle N_{\text{coll}} \rangle$	$\langle N_{\text{part}} \rangle$
0 - 5%	1065 ± 105.5	351.4 ± 2.9
5 - 10%	854.4 ± 82.1	299 ± 3.8
10 - 20%	602.6 ± 59.3	234.6 ± 4.7
20 - 30%	373.8 ± 39.6	166.6 ± 5.4
30 - 40%	219.8 ± 22.6	114.2 ± 4.4
40 - 50%	120.3 ± 13.7	74.4 ± 3.8
50 - 60%	61.0 ± 9.9	45.5 ± 3.3
60 - 70%	28.5 ± 7.6	25.7 ± 3.8
70 - 92%	8.3 ± 2.4	9.5 ± 1.9
min. bias	257.8 ± 25.4	109.1 ± 4.1
0 - 20%	779 ± 75.2	279.9 ± 4.0
20 - 40%	297 ± 30.8	140.4 ± 4.9
40 - 60%	90.6 ± 11.8	60 ± 3.5
60 - 92%	14.5 ± 4	14.5 ± 2.5

excellent statistical significance of the measurements allows the results to be presented in *fine* centrality selections of 0-5%, 5-10%, 10-20%, 20-30%, 30-40%, 40-50%, 50-60%, 60-70%, 70-92.2%.

A Glauber model Monte-Carlo simulation [48, 49] that includes the responses of the BBC and ZDC was used to estimate the average number of binary collisions $\langle N_{\text{coll}} \rangle$, and participating nucleons $\langle N_{\text{part}} \rangle$ for each centrality class. These values are listed in Table. I.

B. Tracking and Background Estimation

Charged hadrons were reconstructed in the two central arms of PHENIX, each covering -0.35 to 0.35 in pseudo-rapidity and 90° in azimuth. Tracks were measured outside the PHENIX central magnetic field by the drift chambers, located at a radius of 2.0 m from the vertex, and two layers of multi-wire proportional chamber (PC1 and PC3), located 2.5 and 5.0 m, respectively, from the vertex [47]. The momentum resolution was determined to be $0.7\% \oplus 1.0\% p$ (GeV/ c) [7].

To reduce background particles that do not originate from the event vertex, such as weak decays and conversion electrons, tracks were required to have a matching hit within a $\pm 2.3\sigma$ window in PC3. For $p_T > 4$ GeV/ c , an additional matching hit at the EMC was required to suppress background tracks that randomly associate with a hit in PC3 [7]. For triggers with $p_T > 5$ GeV/ c , a p_T -dependent energy cut in the EMC and a tight $\pm 1.5\sigma$ matching cut at the PC3 were applied to reduce the physical background from post-field photon conversions and weak decays to a level $< 10\%$ of real tracks [50]. This energy cut helps to suppress any level-1 bias for the LVL1 $p+p$ dataset. We checked the consistency between the

MB and LVL1 $p + p$ dataset for triggers with $p_T > 5$ GeV/ c by performing the same analysis separately on the two $p + p$ datasets. Any remaining biases due to level-1 trigger selection were found to be within the quoted errors. With these cuts, the background level for triggers was estimated to be $\lesssim 5\%$ for $p_T \lesssim 3$ GeV/ c , and increases to $\sim 10\%$ for $p_T > 4$ GeV/ c [7]. A p_T -dependent correction to the per-trigger yield was used to account for this background.

For partner hadrons, the same matching cuts used for trigger hadrons were applied. However, the p_T -dependent energy cut for 5 – 10 GeV/ c partners was found to be unnecessary. The jet associated partner charged hadron spectrum is much flatter than that for the trigger hadrons. Thus, the background contamination of partners is much reduced relative to that for the trigger hadrons. In addition, the background tracks contributing to combinatoric pairs do not affect the jet signal and can be subtracted out.

A full GEANT simulation of PYTHIA jet events in the PHENIX detector, as detailed in [50], was used to evaluate the effects of this high- p_T background for partner hadrons. Partner yields were extracted following the same procedures used for the actual data analysis. These were then compared to the input partner hadron spectra. For high- p_T triggered events, the background contributions to the partner hadrons were found to be less than 10% for integrated partner yields in the 5-10 GeV/ c cut.

The single particle efficiency for triggers and partners, ϵ^a and ϵ^b in Eq. 15 and Eq. 17, were determined such that the single unidentified hadron p_T spectra reproduce the previously published data for Au+Au [7] and $p + p$ [51]. It includes detector acceptance, reconstruction efficiency, occupancy, and background [7]. The detector acceptance and reconstruction efficiency were estimated with a Monte-Carlo simulation in which simulated single tracks were reconstructed in the PHENIX detector, using the same analysis chain employed for the real data. The efficiency loss due to detector occupancy in Au+Au collisions was estimated by reconstructing simulated single tracks embedded into real events. More details can be found in Au + Au [7] and $p + p$ [51] analyses.

C. Jet Signal Extraction

The dihadron correlation technique is commonly employed in PHENIX for jet measurements because it surmounts the challenges posed by the detector's limited azimuthal acceptance for single hadrons. Even so, physical correlations due to anisotropic production of hadrons relative to the reaction plane in Au+Au collisions, i.e the elliptic flow, need to be distinguished from the jet correlations. In what follows, we layout the framework for our correlation analysis and an associated decomposition procedure used to separate the elliptic flow and jet correlation contributions.

We define the azimuthal correlation function as

$$C(\Delta\phi) \equiv \frac{N^{\text{same}}(\Delta\phi)}{N^{\text{mixed}}(\Delta\phi)} \quad (8)$$

where $N^{\text{same}}(\Delta\phi)$ and $N^{\text{mixed}}(\Delta\phi)$ are pair distributions from the same- and mixed-events, respectively. Each mixed-event is constructed by combining triggers from a real event with partners from a different, randomly selected event with similar centrality and collision vertex as the real event.

The shape of the mixed-event pair distribution reflects the pair $\Delta\phi$ acceptance of PHENIX detector, but it does not contain physical correlations. The integral of mixed-event pairs reflects the rate of the combinatoric pairs,

$$\int d\Delta\phi N^{\text{mixed}}(\Delta\phi) = N_{\text{evts}} \langle n^a \rangle \langle n^b \rangle \quad (9)$$

where N_{evts} is the number of events and $\langle n^a \rangle$, $\langle n^b \rangle$ represent the average number of triggers and partners per event in the PHENIX acceptance. Both $N^{\text{same}}(\Delta\phi)$ and $N^{\text{mixed}}(\Delta\phi)$ are affected by the pair efficiency, which cancels out in the ratio (see Appendix A). Therefore, the correlation function Eq. 8 contains only physical correlations.

The elliptic flow correlation leads to a harmonic modulation of the combinatoric pair distribution by a factor that is proportional to $(1 + 2v_2^a v_2^b \cos 2\Delta\phi)$, where v_2^a and v_2^b are the average elliptic flow values for triggers and partners respectively. To extract the jet-induced pairs, we follow a two-source ansatz where each particle is assumed to come from a jet-induced source and an underlying event containing elliptic flow. The pair distribution can be expressed as

$$N^{\text{same}}(\Delta\phi) = \xi(1 + 2v_2^a v_2^b \cos 2\Delta\phi) N^{\text{mixed}}(\Delta\phi) + \text{Jet}(\Delta\phi) \quad (10)$$

Where the $\text{Jet}(\Delta\phi)$ represents all pairs from (di-)jets. The integral of N^{same} can be written as,

$$\int d\Delta\phi N^{\text{same}}(\Delta\phi) = N_{\text{evts}} \langle n^a n^b \rangle + \int d\Delta\phi \text{Jet}(\Delta\phi) \quad (11)$$

Comparing to Eq. 9, we obtain

$$\xi = \frac{\langle n^a n^b \rangle}{\langle n^a \rangle \langle n^b \rangle}. \quad (12)$$

Thus, ξ is simply the ratio of the trigger-partner combinatoric rate in the same-event to that in mixed-events, which can be bigger than one due to centrality smearing (see discussion in Section III E). An alternative approach used to fix ξ is to assume that the jet function has zero yield at its minimum $\Delta\phi_{\text{min}}$ (ZYAM) [18, 67].

Finally, the ratio of jet-induced pairs to combinatoric pairs from mixed events, JPR (jet-induced hadron-pair

ratio) is given by,

$$\begin{aligned} \text{JPR}(\Delta\phi) &\equiv \frac{\text{Jet}(\Delta\phi)}{N^{\text{mixed}}(\Delta\phi)} \\ &= \frac{N^{\text{same}}(\Delta\phi)}{N^{\text{mixed}}(\Delta\phi)} - \xi(1 + 2v_2^a v_2^b \cos 2\Delta\phi) \end{aligned} \quad (13)$$

A representative correlation function is given in Fig. 2 for 0-5% Au+Au collisions and for triggers and partners in 2-3 and 1-2 GeV/c, respectively. It shows a peak around $\Delta\phi \sim 0$ and a broad structure around $\Delta\phi \sim \pi$. The dashed line indicates the estimated elliptic flow modulated background via ZYAM method. The area between the data points and the dashed line reflects the jet-induced pair ratio. It is only a few percent relative to the background level.

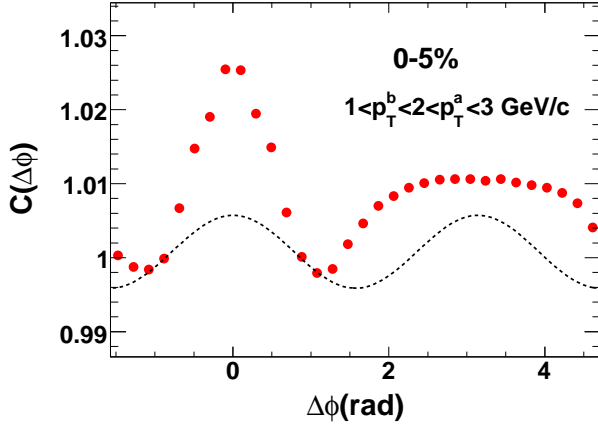


FIG. 2: (Color online) The correlation function for $2 < p_T^a < 3$, $1 < p_T^b < 2$ GeV/c in 0-5% Au+Au collisions. The dashed line represents the estimated elliptic flow modulated combinatoric background using zero yield at minimum (ZYAM) method (see Section.III E).

We define $\varepsilon^a, \varepsilon^b$ as the single particle efficiency within the PHENIX pseudo-rapidity acceptance ($|\eta| < 0.35$). The true numbers of triggers and partners are given by

$$\langle n_0^a \rangle = \langle n^a \rangle / \varepsilon^a ; \quad \langle n_0^b \rangle = \langle n^b \rangle / \varepsilon^b \quad (14)$$

For uncorrelated sources, the triggers and partners are uniform in azimuth. Thus the true combinatoric pair distribution for mixed events is flat with $\Delta\phi$ with a density of $\langle n_0^a \rangle \langle n_0^b \rangle / (2\pi)$. The yield of jet-induced pairs per event, JPY, is given as the product of the combinatoric pair rate and the hadron-pair ratio,

$$\begin{aligned} \text{JPY}(\Delta\phi) &= \frac{\langle n_0^a \rangle \langle n_0^b \rangle}{2\pi} \text{JPR}(\Delta\phi) = \frac{\langle n^a \rangle \langle n^b \rangle}{2\pi \varepsilon^a \varepsilon^b} \text{JPR}(\Delta\phi) \\ &= \frac{\int d\Delta\phi N^{\text{mixed}}(\Delta\phi)}{2\pi N_{\text{evts}} \varepsilon^a \varepsilon^b} \\ &\times \left[\frac{N^{\text{same}}(\Delta\phi)}{N^{\text{mixed}}(\Delta\phi)} - \xi(1 + 2v_2^a v_2^b \cos 2\Delta\phi) \right] \end{aligned} \quad (15)$$

Thus far, we have not made any distinction between trigger and partner hadrons. As discussed earlier in Section II, the correlation function, hadron-pair ratio and hadron-pair yield are symmetric between the trigger and partner p_T , i.e.

$$\begin{aligned} C(p_T^a, p_T^b) &= C(p_T^b, p_T^a) , \\ \text{JPR}(p_T^a, p_T^b) &= \text{JPR}(p_T^b, p_T^a) , \quad \text{and} \\ \text{JPY}(p_T^a, p_T^b) &= \text{JPY}(p_T^b, p_T^a). \end{aligned} \quad (16)$$

The associated partner yield per trigger, $Y_{\text{jet_ind}}(\Delta\phi)$ is obtained by dividing the hadron-pair yield per event with the number of triggers per event,

$$\begin{aligned} Y_{\text{jet_ind}}(\Delta\phi) &= \frac{\text{JPY}(\Delta\phi)}{n_0^a} = \frac{\int d\Delta\phi N^{\text{mixed}}(\Delta\phi)}{2\pi N^a \varepsilon^b} \\ &\times \left[\frac{N^{\text{same}}(\Delta\phi)}{N^{\text{mixed}}(\Delta\phi)} - \xi(1 + 2v_2^a v_2^b \cos 2\Delta\phi) \right] \end{aligned} \quad (17)$$

$Y_{\text{jet_ind}}$ is often referred to as the per-trigger yield or conditional yield. It is clearly not invariant to the exchange of trigger and partner p_T .

The analysis proceeds in the following steps. We first measure the correlation function Eq. 8. We then obtain the efficiency for partner hadrons (ε^b) and the elliptic flow coefficients for the two hadron categories (v_2^a, v_2^b). We then determine the background level (ξ) via ZYAM background subtraction method (see Section.III E), followed by a calculation of the per-trigger yield according to Eq. 17. Subsequently, we obtain the hadron-pair yield by multiplying the per-trigger yield with the inclusive charged hadron yield [7] integrated in the corresponding trigger p_T range.

According to Eq. 6, the hadron-pair yields calculated from the per-trigger yields are independent of which hadron, from the pair, is used as trigger. We have used this fact to cross check the efficacy of our analysis. Figure 3 compares the hadron-pair yields obtained when the trigger and partner p_T is exchanged in $p + p$ collisions (in $p_T^a \otimes p_T^b$). The open symbols indicate the results for low- p_T trigger hadrons in association with high- p_T partners. The filled symbols show the converse. A similar comparison for 0-20% Au+Au collisions is shown in Fig. 4. Overall good agreement is indicated by these distributions. It is important to emphasize here that there is no a priori reason for these distributions to be identical, since the cuts on trigger and partner hadrons are a little different (cf. Section. III B) and therefore could lead to somewhat different systematic errors for each measurement.

D. Elliptic Flow Measurement

The differential elliptic flow measurements for charged hadrons were carried out with the reaction plane method [52]. The event plane (EP), which is the experimental estimate of the reaction plane (RP), is determined via the two BBCs positioned symmetrically along the

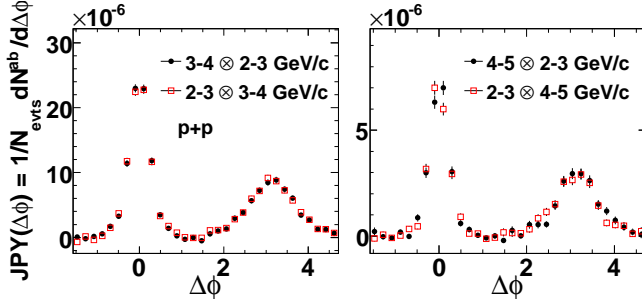


FIG. 3: (Color online) The $p + p$ jet-induced hadron-pair yield $\Delta\phi$ distributions calculated from the per-trigger yield using low- p_T hadrons as triggers (solid symbols) and high- p_T hadrons as triggers (open symbols).

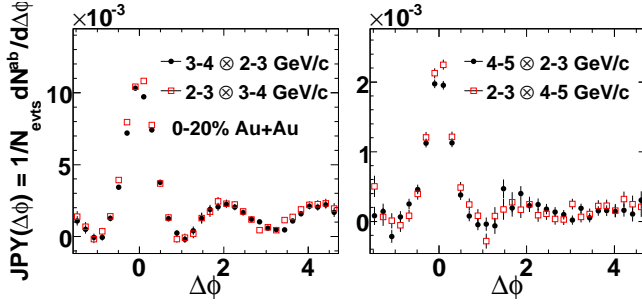


FIG. 4: (Color online) The 0-20% Au+Au jet-induced hadron-pair yield $\Delta\phi$ distributions calculated from the per-trigger yield using low- p_T hadrons as triggers (solid symbols) and high- p_T hadrons as triggers (open symbols).

beam line. They cover full azimuth and $3 < |\eta| < 3.9$ in pseudo-rapidity. The BBCs allow an unbiased measurement of the event plane, and ensures that there are no residual distortions on the correlation function that could result from the limited azimuthal coverage of PHENIX central arms. A detailed analytical proof of this latter point is provided in Appendix B.

We determine the value of elliptic flow, v_2 , as

$$v_2 = \frac{v_{2,\text{raw}}}{c_{v_2}} = \frac{\langle \langle \cos 2(\phi - \Phi_{\text{EP}}) \rangle \rangle}{\langle \cos 2(\Phi_{\text{EP}} - \Phi_{\text{RP}}) \rangle} \quad (18)$$

where Φ_{EP} is the event plane angle and Φ_{RP} is the true reaction plane angle, $v_{2,\text{raw}} = \langle \langle \cos 2(\phi - \phi_{\text{EP}}) \rangle \rangle$ is the raw v_2 and $c_{v_2} = \langle \cos 2(\Phi_{\text{EP}} - \Phi_{\text{RP}}) \rangle$ is the estimated reaction plane resolution. The former is obtained by averaging over all tracks and all events, the latter is obtained by averaging over all events. The resolution is estimated from the event plane angle of the north and south BBC as $c_{v_2} = \sqrt{2 \langle \cos 2(\Phi_{\text{EP},\text{North}} - \Phi_{\text{EP},\text{South}}) \rangle}$ [53, 54]. It is 0.3 for minimum bias events, and reaches a maximum of 0.42 in the 20-30% centrality bin. Further details are given in [54].

Reliable extraction of the jet signal requires accurate determination of v_2^a and v_2^b . To this end, non-flow effects that lead to azimuthal correlations unrelated to

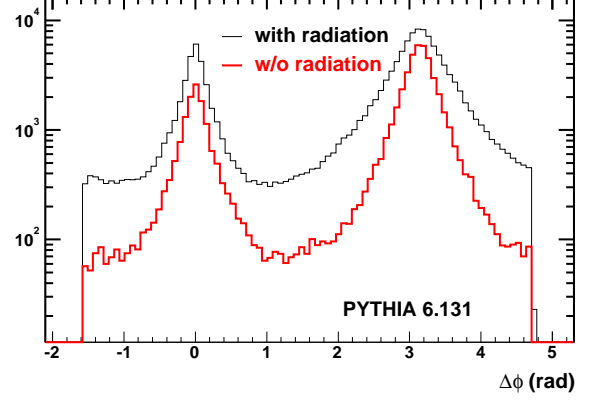


FIG. 5: (Color online) PYTHIA simulation showing jet-induced hadron pair $\Delta\phi$ distribution for $3 < p_T^a, p_T^b < 5$ GeV/c with (top histogram) and without (bottom histogram) initial and final state radiation. The radiation accounts for the increase of the background level.

the true RP direction, need to be studied. These effects include various long- or short-range correlations among clusters of particles, such as momentum conservation effects, resonance decays, HBT correlations and jets [55, 56]. While jets potentially bias the v_2 measurement at high p_T , other non-flow effects may be important at low and intermediate p_T . The values of v_2 are also sensitive to event by event fluctuations of the collision geometry [57, 58, 59, 60] (so called v_2 fluctuations), which affect all p_T regions.

A bias to v_2 resulting from jets has been reported for high- p_T hadrons [61]. However, the relative significance of other non-flow effects and v_2 fluctuations is still under debate. Recent studies from PHOBOS [62] and STAR [63] suggest that the fluctuations dominate over the non-flow effects for the p_T integral v_2 .

Following the two-source assumption in Eq. 11, any correlations other than jets are attributed to the background term, i.e. $1 + 2v_2^a v_2^b \cos 2\Delta\phi$. These naturally include most non-flow correlations and v_2 fluctuations. In order to estimate the potential biases from jets and dijets, we carried out a detailed study in Appendix C, in which we embedded dijet PYTHIA events into flow modulated HIJING events. Our study shows that the large rapidity separation between the PHENIX BBCs and central arms greatly reduces the influence of jets on our v_2 measurements. Consequently, we use the BBC reaction plane v_2 measurements to evaluate and subtract the elliptic flow modulated background.

E. Combinatoric Background Subtraction

The background level ξ can be determined precisely if we know the exact functional form for the near- and away-side jets, or if we can independently measure the

underlying event rate. However, due to in-medium modifications, the near- and away-side jets are not necessarily Gaussian, especially for $\Delta\phi$ values away from 0 and π . Even in $p + p$ collisions, the underlying event can include contributions from multiple-parton interaction, beam remnants, initial and final state radiation [64], which are related to the hard-scattering but not necessarily correlated in $\Delta\phi$. Such effects have been studied at the Tevatron [64, 65] and RHIC [44] energies. For illustration purposes, Figure 5 shows the dihadron correlation from PYTHIA [66] with and without initial and final state radiation effects. The difference between the two is clearly significant.

Rigorous decomposition of the jet from its underlying event currently requires assumptions about the jet shape or the physics of the underlying event. As discussed earlier, a simple approach to fix ξ is to follow the subtraction procedure outlined in Refs. [18, 67]. That is, one assumes that the jet function has zero yield at its minimum $\Delta\phi_{\min}$ (ZYAM), after subtraction of the underlying event. The uncertainty on ξ from this procedure is related to the statistical accuracy of the data around $\Delta\phi_{\min}$. In the present analysis, this uncertainty is negligible at low p_T , but becomes important for $p_T^{A,B} > 4$ GeV/c in central collisions.

The ZYAM procedure, by definition, provides only a lower limit on the jet yield. To estimate the possible over-subtraction of jet yield at $\Delta\phi_{\min}$, we also made independent estimates of ξ via an absolute combinatoric background subtraction method (ABS) [68] and by a fitting method. In the ABS method, ξ , as defined by Eq. 12, is assumed to reflect only a residual multiplicity smearing effect caused by intrinsic positive correlations between the n_0^a and n_0^b in real events, i.e. a larger n_0^a implies a larger n_0^b and vice versa. Because of this positive correlation, the average of the product can become larger than the product of the average, i.e. $\langle n_0^a n_0^b \rangle > \langle n_0^a \rangle \langle n_0^b \rangle$ or $\xi > 1$.

To estimate ξ , we parameterize the centrality dependence of the trigger and partner rate from the measured single particle spectra in relevant momentum range, as a function of either N_{part} or N_{coll}

$$\langle n_0^{a,b} \rangle = f(N_{\text{part}}) = g(N_{\text{coll}}). \quad (19)$$

We then assume the event-by-event fluctuation of trigger and partner hadrons to follow a Poisson distribution around their mean values,

$$n_0^{a,b} = \text{Poisson}(\langle n_0^{a,b} \rangle). \quad (20)$$

However, we have verified that that our estimates are not very sensitive to the functional forms of the fluctuations.

For each centrality bin, we determine the distribution of N_{part} and N_{coll} from standard PHENIX Glauber calculation [48, 49]. For each simulated event, we sample randomly from the N_{part} distribution, calculate the corresponding mean value $\langle n_0^{a,b} \rangle$ and then the actual value $n_0^{a,b}$ after taking into account the fluctuation. The same

exercise is repeated for the N_{coll} distributions. The final ξ is given by the average of the two and their difference is taken as the systematic error. The correction modifies the background level by 0.2% in the most central and 25% in 60-92% centrality bin. The ABS method and ZYAM methods give consistent ξ values in central collisions, but the ABS method gives somewhat lower values in peripheral collisions.

In the fit method, $Y_{\text{jet,ind}}(\Delta\phi)$ is fitted with a function comprised of one near- and two symmetric away-side Gaussians, following a procedure similar to that reported in Ref. [19]. One important difference is that a region around π ($|\Delta\phi - \pi| < 1$) is excluded to avoid the punch-through jet contributions (see Fig. 6). Thus, the fit uses the near-side and the falling edge of the away-side to estimate the overlap of the near- and away-side Gaussians at $\Delta\phi_{\min}$. This approach gives systematically lower ξ values than those obtained from the ZYAM and ABS methods.

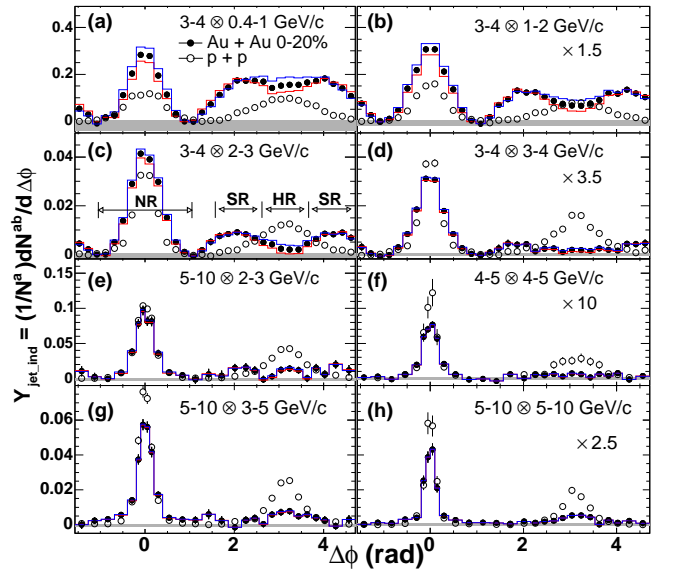


FIG. 6: (Color online) Per-trigger yield versus $\Delta\phi$ for various trigger and partner p_T ($p_T^a \otimes p_T^b$), arranged by increasing pair proxy energy (sum of p_T^a and p_T^b), in $p + p$ and 0-20% Au+Au collisions. The data in several panels are scaled as indicated. Solid histograms (shaded bands) indicate elliptic flow (ZYAM) uncertainties. Arrows in Fig. 6c depict the “Head” region (HR), the “Shoulder” region (SR) and the “Near-side” region (NR).

Table. II summarizes the ξ values from the three methods. The results for the ZYAM and ABS methods are close, but the values from the fitting method are systematically lower. This could be due to the correlations between the fitting parameters or a limitation in the Gaussian assumptions for the jet shape. To avoid a possible overestimation of the jet yield in the $\Delta\phi$ region where the near- and away-side Gaussians overlap, we constrain the ξ to be ≥ 1 . This is a reasonable assumption in the absence of anti-correlation in trigger and partner hadron

multiplicity. We assign the differences with the ZYAM method as a one-sided systematic error on ξ . This error is important in central collisions and for $p_T^{a,b} < 3$ GeV/c.

TABLE II: Comparison of the ξ values obtained for three different normalization methods for several centrality selections. They are calculated for $2.5 < p_T^a < 4.0$ GeV/c and $1.0 < p_T^b < 2.0$ GeV/c bin.

Cent.	ZYAM	ABS	Constrained fit
0-5%	1.0018 ± 0.0004	1.0023 ± 0.0002	0.998 ± 0.002
20-30%	1.015 ± 0.0015	1.012 ± 0.003	1.004 ± 0.006
50-60%	1.076 ± 0.009	1.07 ± 0.02	1.054 ± 0.009

F. Systematic Uncertainties

We classify the systematic errors associated with the jet yield into three main categories: (1) Uncertainties in the single particle efficiency correction, ϵ^a and ϵ^b , for Au+Au and $p+p$; (2) Statistical and systematic uncertainties associated with the determination of the elliptic flow values, v_2^a and v_2^b , in Au+Au collisions; (3) Uncertainties associated with the determination of the combinatoric background level ξ in both Au+Au and $p+p$ collisions.

The uncertainties associated with the efficiency corrections include contributions from the detector acceptance (5%), matching cuts (4%), momentum scale and momentum resolution (5%). The background contamination is estimated to be 5% for $p_T < 5$ GeV/c, increasing to 10% for the 5-10 GeV/c bin. This leads to an overall systematic error of $\sim 10\%$ for $p_T < 5$ GeV/c and 13% for the 5-10 GeV/c bin. For central Au+Au collisions, there is an additional maximally 5%, centrality-dependent uncertainty due to occupancy effect.

The propagation of uncertainties arising from the single particle efficiency are different for different jet variables. For the per-trigger yield, it depends on the errors associated with the efficiency estimated for the partners (ϵ^b). For the hadron-pair yields, it depends on the errors related to efficiencies for both trigger (ϵ^a) and partner (ϵ^b) hadrons. Since the efficiency correction uncertainties are similar for trigger and partner hadrons in both Au+Au and $p+p$ collisions, we can use a single variable ϵ to represent them. If the uncertainties are independent between Au+Au and $p+p$, the total uncertainty would be $\sim \sqrt{2}\delta\epsilon/\epsilon$ for JPY and I_{AA} and $2\delta\epsilon/\epsilon$ for J_{AA} . However, some systematic errors partially cancel between Au+Au and $p+p$, especially those for the matching cut, momentum scale and momentum resolution. The total uncertainties are estimated to be 12% for I_{AA} and JPY, and 17% for J_{AA} .

The statistical uncertainties for v_2 are important in the most central and most peripheral centrality bins for $p_T > 4$ GeV/c. The systematic uncertainties are however driven by the uncertainty associated with the determination of the reaction plane resolution; they are estimated

to be $\sim 6\%$ for central and mid-central collisions, and $\sim 10\%$ for peripheral collisions [18]. This error is nearly independent of p_T , i.e. $\delta v_2^a/v_2^a \approx \delta v_2^b/v_2^b$, and the resulting error for the hadron-pair ratio is,

$$\begin{aligned} \delta \text{JPR}(\Delta\phi) &= 2\xi(\delta v_2^a v_2^b + \delta v_2^b v_2^a) \cos 2\Delta\phi \\ &\approx (\delta v_2/v_2) 4v_2^a v_2^b \cos 2\Delta\phi \end{aligned} \quad (21)$$

where the last approximation takes into account the fact that ξ is close to 1. Additional systematic errors related to v_4 and the factorization assumption that $\langle v_2^a v_2^b \rangle = \langle v_2^a \rangle \langle v_2^b \rangle$, were also estimated and found to be small [19].

The uncertainty due to ξ (ZYAM uncertainty) can be expressed as,

$$\delta \text{JPR}(\Delta\phi) = \delta\xi (1 + 2v_2^a v_2^b \cos 2\Delta\phi) \approx \delta\xi \quad (22)$$

where we ignored the $\cos 2\Delta\phi$ term since $2v_2^a v_2^b \ll 1$. The uncertainty of ξ includes both the statistical error of the data points around $\Delta\phi_{\min}$ and the systematic error from the fitting procedure.

Table. III summarizes the systematic errors for the jet yield in 0-20% Au+Au collisions due to v_2 and ZYAM subtraction. Errors for several combinations of trigger and partner p_T (in $p_T^a \otimes p_T^b$) are given. The uncertainties are $\Delta\phi$ dependent, so we present them separately for the three regions used in this analysis: a “head” region ($|\Delta\phi - \pi| < \pi/6$, HR), a “shoulder” region ($\pi/6 < |\Delta\phi - \pi| < \pi/2$, SR) and the “near-side” region ($|\Delta\phi| < \pi/3$, NR). These regions are indicated in Figure 6c.

The three types of systematic errors impacts the jet shape and jet yield differently. The single particle efficiency correction is a multiplicative factor, so its uncertainty influences the normalization of the jet yield, but does not influence its shape. The uncertainties associated with the elliptic flow varies with $\Delta\phi$. It is largest for regions around 0 and π , but reaches a minimum in the shoulder region. The influence of the ξ uncertainty on the jet yield also depends on $\Delta\phi$. It is the dominant uncertainty for the away-side yield at high p_T .

IV. RESULTS

A. Jet-induced Dihadron Azimuthal ($\Delta\phi$) Distributions

Figure 6 shows a representative subset of the per-trigger yield distributions, $Y_{\text{jet_ind}}(\Delta\phi)$ for various combinations of trigger and partner p_T ($p_T^a \otimes p_T^b$) for $p+p$ and 0-20% Au+Au collisions, arranged by increasing pair proxy energy, i.e. by $p_T^{\text{sum}} = p_T^a + p_T^b$. The comprehensive array of results, covering the momentum range of 0.4 to 10 GeV/c from which this subset is derived, are summarized in Appendix D (Figs.36-38). From Eq. 6, one can see that the distributions for $p_T^a \otimes p_T^b$ and $p_T^b \otimes p_T^a$ are related to each other by a normalization factor n_0^a/n_0^b , i.e. the ratio of the number of hadrons in the two p_T ranges. We have checked that these distributions, when re-scaled by n_0^a or

TABLE III: Systematic errors for the per-trigger yield in 0-20% Au+Au collisions for several combinations of trigger and partner p_T (in trigger $p_T \otimes$ partner p_T). The errors are in percentage and are shown separately for near-side ($|\Delta\phi| < \pi/3$), away-side ($|\Delta\phi - \pi| < \pi/2$), away-side head region ($|\Delta\phi - \pi| < \pi/6$), and away-side shoulder region ($\pi/6 < |\Delta\phi - \pi| < \pi/2$).

Errors in %	$2-3 \otimes 0.4-1$ GeV/c	$2-3 \otimes 2-3$ GeV/c	$3-4 \otimes 3-4$ GeV/c	$4-5 \otimes 4-5$ GeV/c	$5-10 \otimes 5-10$ GeV/c
near-side					
v_2 err.	± 18	± 9.5	± 3.8	± 1	< 1
ZYAM err. stat.	± 0.9	± 1.1	± 4.1	± 9	± 8
ZYAM over-sub.	$+30$	$+9.5$	< 1	< 1	< 1
away-side					
v_2 err.	± 10	± 10	± 9.3	± 3	± 1
ZYAM err. stat.	± 0.8	± 2	± 17	± 39	± 28
ZYAM over-sub.	$+28$	$+17$	< 1	< 1	< 1
away-side head region					
v_2 err.	± 26	$+42-39$	$+36-34$	± 5	± 1
ZYAM err. stat.	± 1	± 3	± 27	± 32	± 16
ZYAM over-sub.	$+28$	$+29$	< 1	< 1	< 1
away-side shoulder region					
v_2 err.	± 2.6	± 2.3	± 2	± 1	± 1
ZYAM err. stat.	± 0.8	± 1.6	± 15	± 43	± 45
ZYAM over-sub.	$+27$	$+15$	< 1	< 1	< 1

n_0^b , are consistent with each other. These $\Delta\phi$ distributions not only carry detailed jet shape and yield information, they serve as a basis for our systematic study of the p_T dependence of the contributions from various physical processes.

The results in Fig. 6 constitutes one of many possible ways of illustrating the evolution from low p_T to high p_T in the two dimensional space of p_T^a and p_T^b . It is designed to highlight the main features of an evolution from the soft-process dominated low- p_T region to the hard-process dominated high- p_T region. As shown in the figure, the $p+p$ data show essentially Gaussian away-side peaks centered at $\Delta\phi \sim \pi$ for all p_T^a and p_T^b . By contrast, the Au+Au data show substantial modifications relative to those for $p+p$ collisions, and these modifications vary non-trivially with p_T^a and p_T^b . For a fixed value of p_T^a , Figs. 6a - 6d reveal a striking evolution from a broad, roughly flat away-side peak to a local minimum at $\Delta\phi \sim \pi$ with side-peaks at $\Delta\phi \sim \pi \pm 1.1$. Interestingly, the location of the side-peaks in $\Delta\phi$ is found to be roughly constant with increasing p_T^b (see Fig. 11). Such p_T independence is compatible with an away-side jet modification expected from a medium-induced Mach shock [35] but provides a challenge for models which incorporate large angle gluon radiation [31, 32], Cherenkov gluon radiation [34] or deflected jets [23, 29].

For relatively large values of $p_T^a \otimes p_T^b$, Figs. 6e - 6h (also Fig. 36) show that the away-side jet shape for Au+Au gradually becomes peaked as for $p+p$, albeit suppressed. This “re-appearance” of the away-side peak seems to be due to a reduction of the yield centered at $\Delta\phi \sim \pi \pm 1.1$ relative to that at $\Delta\phi \sim \pi$, rather than a merging of the peaks centered at $\Delta\phi \sim \pi \pm 1.1$. This is consistent with the dominance of dijet fragmentation at large $p_T^a \otimes p_T^b$, possibly due to jets that “punch-through” the medium [14] or those emitted tangentially to the

medium’s surface [69].

The evolution pattern of the away-side jet shape with p_T suggests separate contributions from a medium-induced component at $\Delta\phi \sim \pi \pm 1.1$ and a fragmentation component centered at $\Delta\phi \sim \pi$. A model independent study of these contributions can be made by dividing the away-side jet function into equal-sized “head” ($|\Delta\phi - \pi| < \pi/6$, HR) and “shoulder” ($\pi/6 < |\Delta\phi - \pi| < \pi/2$, SR) regions, as indicated in Fig. 6c.

Figure 6 also shows significant modifications of the near-side $\Delta\phi$ distributions. For the $p_T^a \otimes p_T^b$ bins where the away-side has a concave shape, the near-side jet also shows a clear enhancement in the yield and a modification of the width relative to $p+p$. To facilitate a more detailed investigation, we define a “near-side” region ($|\Delta\phi| < \pi/3$, NR) as indicated in Fig. 6c. In the following, we focus on the jet-induced pairs in these three $\Delta\phi$ regions, and discuss in detail the p_T and centrality dependence of their shapes and yields.

B. Medium Modification of Away-side Jets

1. Away-side jet shape

We characterize the relative importance of the jet yields in the HR and the SR by the ratio, R_{HS} ,

$$R_{HS} = \frac{\int_{\Delta\phi \in \text{HR}} d\Delta\phi Y_{\text{jet-ind}}(\Delta\phi)}{\int_{\Delta\phi \in \text{HR}} d\Delta\phi} \bigg/ \frac{\int_{\Delta\phi \in \text{SR}} d\Delta\phi Y_{\text{jet-ind}}(\Delta\phi)}{\int_{\Delta\phi \in \text{SR}} d\Delta\phi} \quad (23)$$

i.e. it is a ratio of area-normalized jet yields in the HR and the SR. This ratio reflects the away-side jet shape and is symmetric with respect to p_T^a and p_T^b , i.e. $R_{HS}(p_T^a, p_T^b) = R_{HS}(p_T^b, p_T^a)$. For concave and convex

shapes, one expects $R_{\text{HS}} < 1$ and $R_{\text{HS}} > 1$ respectively; for a flat distribution, $R_{\text{HS}} = 1$.

Figure 7 shows the p_{T}^{b} dependence of R_{HS} for both $p+p$ and central Au+Au collisions for four p_{T}^{a} bins. The uncertainty for efficiency corrections drops out in the ratio; the v_2 errors (shaded bars) and ZYAM errors (brackets) are correlated in the two regions, thus they partially cancel.

The R_{HS} values for $p+p$ are always above one and increase with p_{T}^{b} . This reflects the narrowing of a peaked away-side jet shape with increasing p_{T}^{b} . In contrast, the ratios for Au+Au show a non-monotonic dependence on $p_{\text{T}}^{\text{a,b}}$. They evolve from $R_{\text{HS}} \sim 1$ for p_{T}^{a} or $p_{\text{T}}^{\text{b}} \lesssim 1$ GeV/c, through $R_{\text{HS}} < 1$ for $1 \lesssim p_{\text{T}}^{\text{a,b}} \lesssim 4$ GeV/c, followed by $R_{\text{HS}} > 1$ for $p_{\text{T}}^{\text{a,b}} \gtrsim 5$ GeV/c. These trends reflect the competition between medium-induced modification and jet fragmentation in determining the away-side jet shape, and suggest that the latter dominates for $p_{\text{T}}^{\text{a,b}} \gtrsim 5$ GeV/c.

R_{HS} values for Au+Au are smaller than those for $p+p$ even at the highest p_{T} . This difference could be due to some medium modification of the punch-through jets. However, the HR yield dominates the SR yield ($R_{\text{HS}} \gg 1$) in this p_{T} region, and the values for R_{HS} becomes very sensitivity to the SR yield. For instance, a small enhancement of the SR yield can significantly reduce the value of R_{HS} , without significantly affecting the overall away-side feature.

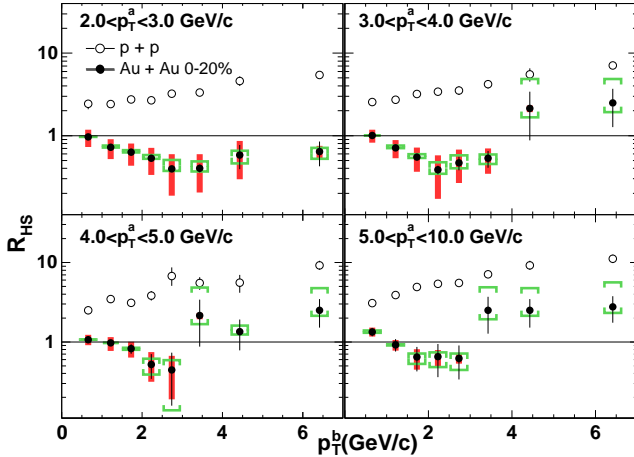


FIG. 7: (Color online) R_{HS} versus p_{T}^{b} for $p+p$ (open) and Au+Au (filled) collisions for four trigger selections. Shaded bars (brackets) represent p_{T} -correlated uncertainties due to elliptic flow (ZYAM procedure).

R_{HS} values reach their minimum around 2-3 GeV/c. Additional information can be obtained from their centrality dependence, as shown in Fig. 8 for $2 - 3 \otimes 2 - 3$ GeV/c bin. R_{HS} starts at around 3 for $p+p$ collisions but quickly drops and crosses 1 at $N_{\text{part}} \sim 80$. It then slowly decreases with N_{part} to a level of about 0.5 in central collisions. This trend implies a quick change of the HR and/or SR yield in relatively peripheral collisions. The saturation of the R_{HS} for $N_{\text{part}} > 200$ may suggest that

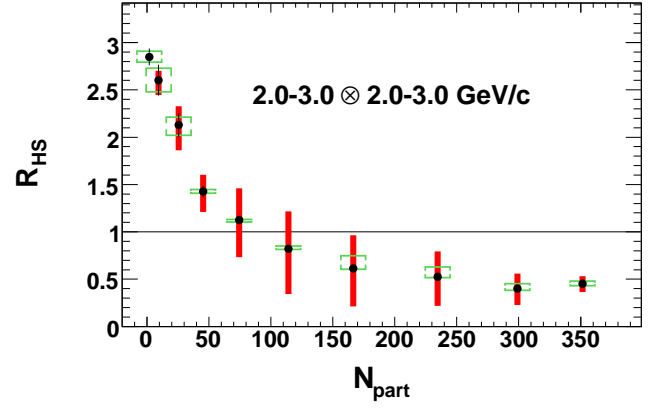


FIG. 8: (Color online) R_{HS} versus N_{part} for $2-3 \otimes 2-3$ GeV/c. Shaded bars (brackets) represent p_{T} -correlated uncertainties due to elliptic flow (ZYAM procedure). The most left point is from $p+p$.

TABLE IV: Centrality dependence of R_{HS} for $2 < p_{\text{T}}^{\text{a}}, p_{\text{T}}^{\text{b}} < 3$ GeV/c (Fig. 8).

$\langle N_{\text{part}} \rangle$	R_{HS}	Stat.	v_2 Err.	Norm Err.
351.4	0.451	0.030	+0.080-0.087	+0.028-0.021
299.0	0.402	0.024	+0.158-0.175	+0.051-0.019
234.6	0.526	0.018	+0.268-0.308	+0.102-0.011
166.6	0.614	0.021	+0.351-0.402	+0.133-0.009
114.2	0.821	0.030	+0.395-0.477	+0.031-0.006
74.4	1.126	0.045	+0.333-0.394	+0.005-0.022
45.5	1.427	0.060	+0.175-0.215	+0.020-0.018
25.7	2.130	0.125	+0.196-0.267	+0.081-0.110
9.5	2.603	0.164	+0.099-0.158	+0.125-0.124
2.0	2.848	0.090	—	+0.060-0.056

the HR yield is dominated by the feed-in of the SR yield (see further discussion in Section.IV B 2).

Although the p_{T} and centrality dependence of R_{HS} suggests that the away-side yield contains separate contributions from a fragmentation component (in the HR) and a medium-induced component (in the SR), R_{HS} does not constrain the shape of the two components directly. An alternative approach for quantifying the away-side shape, is to assume a specific functional form for these two components and carry out a model-dependent fit. Such a fit was performed with the following two functional forms,

$$Y_{\text{jet_ind}}^{\text{FIT1}}(\Delta\phi) = G_1(\Delta\phi) + G_2(\Delta\phi - \pi + D) + G_2(\Delta\phi - \pi - D) + \kappa \quad (24)$$

$$Y_{\text{jet_ind}}^{\text{FIT2}}(\Delta\phi) = G_1(\Delta\phi) + G_2(\Delta\phi - \pi + D) + G_2(\Delta\phi - \pi - D) + G_3(\Delta\phi - \pi) + \kappa \quad (25)$$

The first (FIT1) assumes two Gaussian shoulder components located symmetrically about π , each separated by the distance D from π . The second (FIT2) assumes the same shoulder components but also includes an additional Gaussian component centered at π ; the latter represents the jet fragmentation contribution, and is parameterized to have the same width as that for the $p+p$

away-side jet. FIT1 has six free parameters: background level (κ), near-side peak integral and width, shoulder peak location (D), integral and width. In addition to the parameters of FIT1, FIT2 has a parameter which controls the integral of the fragmentation component.

The separate contributions of FIT1 and FIT2 are illustrated for a typical $p_T^a \otimes p_T^b$ in Fig. 9.

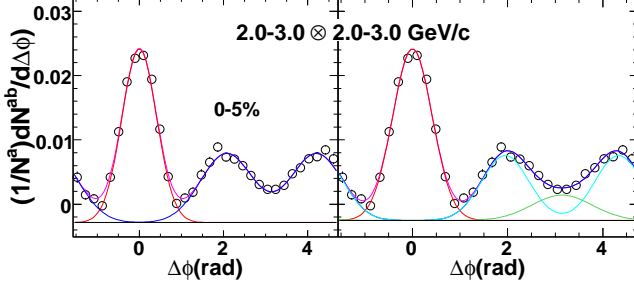


FIG. 9: (Color online) Per-trigger yield $\Delta\phi$ distribution and corresponding fits for $2-3 \otimes 2-3$ GeV/c in 0-5% Au+Au collisions. FIT1 (FIT2) is shown in the left panel (right panel). The total fit function and individual components are shown relative to the κ level indicated by the horizontal line.

The two fits treat the region around $\Delta\phi = \pi$ differently. FIT2 tends to assign the yield around π to the center Gaussian, while FIT1 tends to split that yield into the two shoulder Gaussians. Note, however, that a single Gaussian centered at π can be treated as two shoulder Gaussians with $D = 0$. Thus FIT1 does a good job at low p_T and high p_T , where the away-side is dominated by shoulder and head component, respectively. It does not work as well for intermediate p_T , where both components are important. The center Gaussian and shoulder Gaussians used in FIT2 are strongly anti-correlated. That is, a small shoulder yield implies a large head yield and vice versa. In addition, the center Gaussian tends to “push” the shoulder Gaussians away from π , and this results in larger D values than obtained with FIT1.

Figure 10a shows the D values obtained from the two fitting methods as a function of centrality for the p_T selection $2-3 \otimes 2-3$ GeV/c. The systematic errors from v_2 are shown as brackets (shaded bars) for FIT1 (FIT2). The values of D for FIT1 are consistent with zero in peripheral collisions, but grow rapidly to ~ 1 for $N_{\text{part}} \sim 100$, approaching ~ 1.05 in the most central collisions. The D values obtained from FIT2 are slightly larger (~ 1.2 radians) in the most central collisions. They are also relatively stable to variations of v_2 because most of the yield variation is “absorbed” by the center Gaussian (cf. Fig. 10b). Thus, the associated systematic errors are also smaller than those for FIT1.

For $N_{\text{part}} < 100$, the centrality dependence of D is also quite different for FIT1 and FIT2. As seen in Fig. 10, the D values for FIT2 are above 1. However the away-side yield in the SR, associated with these D values, are rather small and the away-side distribution is essentially a single peak centered around π . For such cases, the

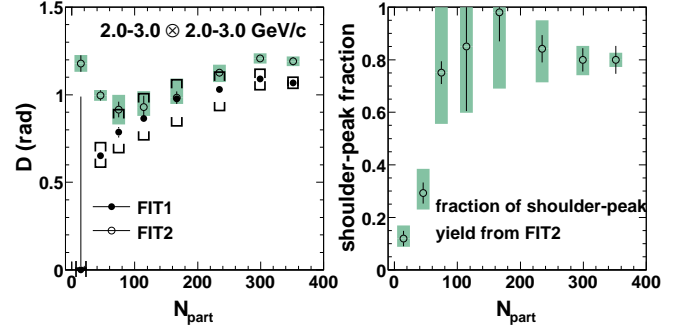


FIG. 10: (Color online) a) D versus N_{part} from FIT1 (solid circles) and FIT2 (open circles) for $2-3 \otimes 2-3$ GeV/c bin. The error bars are the statistical errors; The shaded bars and brackets are the systematic errors due to v_2 . b) The fraction of the shoulder Gaussian yield relative to the total away-side yield as function of N_{part} determined from FIT2.

values of D are prone to fluctuations and non-Gaussian tails. The deviation between the D values obtained with FIT1 and FIT2 for $N_{\text{part}} < 100$ simply reflects the weak constraint of the data on D in peripheral collisions.

Figure 11 shows the p_T dependence of D in 0-20% central Au+Au collisions. The values from FIT2 are basically flat with p_T^b . Those from FIT1 show a small increase with p_T^b , but with a larger systematic error. At low p_T , the values from FIT1 are systematically lower than those from FIT2. However, they approach each other at large $p_T^{a,b}$. From FIT1 and FIT2, it appears that the values of D covers the range 1-1.2 radians for $p_T^a, p_T^b \lesssim 4$ GeV/c. This trend ruled out a Cherenkov gluon radiation model [34] (with only transition from scalar bound states), which predicts decreasing D with increasing momentum.

2. Away-side jet per-trigger yield

Relative to $p + p$, the Au+Au yield is suppressed in the HR but is enhanced in the SR (cf. Fig. 6). A more detailed mapping of this modification pattern is obtained by comparing the jet yields in the HR and SR as a function of partner p_T . Such a comparison is given in Fig. 12 for central Au+Au and for $p + p$ collisions. The figure shows that, relative to $p + p$, the Au+Au data are enhanced in the SR for low p_T , and suppressed in the HR for high p_T . The shape of the Au+Au spectra in the HR is also quite different from that for $p + p$. For $p_T^{a,b} \lesssim 4$ GeV/c, the spectra for Au+Au are steeper than those for $p + p$. For higher p_T , both spectra have the same shape (parallel to each other) but the yield for Au+Au is clearly suppressed.

To quantify this suppression/enhancement, we use the per-trigger yield ratio I_{AA} , the ratio of per-trigger yield for Au+Au collisions to that for $p+p$ collisions (cf. Eq. 5). Such ratios for the HR and the HR+SR are shown as a

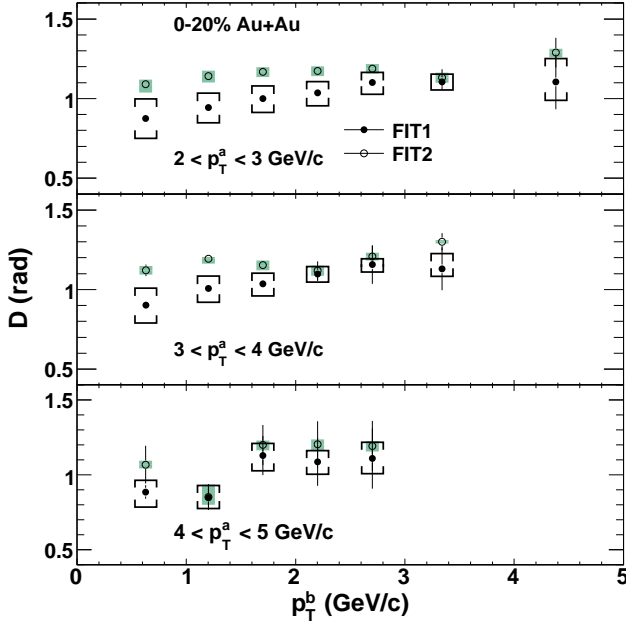


FIG. 11: (Color online) Values of D determined from FIT1 (solid circles) and FIT2 (open circles) as function of partner p_T for three trigger p_T ranges in 0-20% Au+Au collisions. The error bars are the statistical errors. The shaded bars and brackets are the systematic errors due to elliptic flow.

function of p_T^b for four different p_T^a selections in Fig. 13. For triggers of $2 < p_T^a < 3$ GeV/c, I_{AA} for HR+SR exceeds one at low p_T^b , but falls with p_T^b and crosses one around 3.5 GeV/c. A similar trend is observed for the higher p_T triggers, but the enhancement for low p_T^b is smaller and the suppression for high p_T^b is stronger. The I_{AA} values in the HR are also lower relative to HR+SR, for all $p_T^{a,b}$. For the low- p_T triggers, the HR suppression sets in for $1 \lesssim p_T^b \lesssim 3$ GeV/c, followed by a fall-off for $p_T^b \gtrsim 4$ GeV/c. For the higher- p_T triggers, a constant level $\sim 0.2 - 0.3$ is observed above ~ 2 GeV/c, similar to the suppression level of inclusive hadrons [7].

For comparison, Fig. 14 shows the I_{AA} for peripheral collisions. They indicate that, in contrast to the values for central collisions, there is only a small suppression in both the HR and the HR+SR for low- p_T triggers at large p_T^b . Moreover, the overall modifications are much smaller than observed for the more central Au+Au collisions.

A more detailed view of the enhancement/suppression patterns in the SR/HR can be provided by investigating their centrality dependence. Figure 15 shows the per-trigger yield in the SR and HR as function of N_{part} for trigger p_T of 3-4 GeV/c and five partner p_T bins ranging from 0.4 to 5 GeV/c. With increasing partner p_T , both the SR and HR yields show a characteristic evolution with N_{part} . That is, they first show an increase, followed by an essentially flat dependence, followed by a decrease (in the HR only). However, the values of p_T^b at which the centrality dependence becomes flat is quite different for the SR and the HR ($p_T^b \sim 4$ GeV/c for the SR and

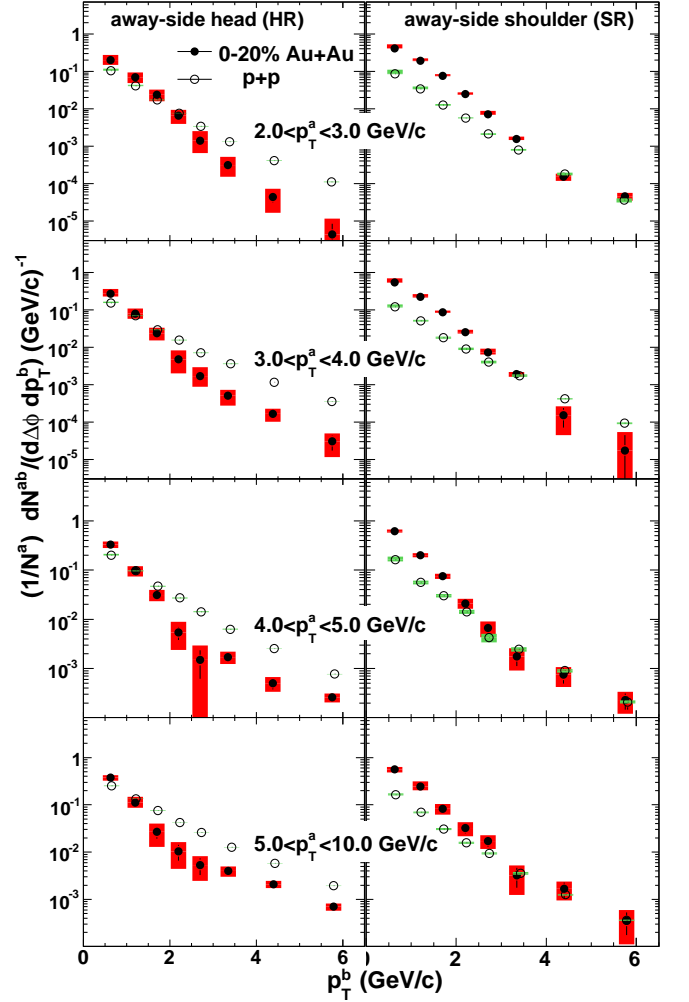


FIG. 12: (Color online) Per-trigger yield as function of partner p_T for the HR (left panels) and the SR region (right panels). Filled (open) circles represent the 0-20% Au+Au ($p+p$) collisions. Results for four trigger p_T in 2-3, 3-4, 4-5, 5-10 GeV/c are shown. The shaded bars represent the total systematic uncertainties.

$p_T^b \sim 1 - 2$ GeV/c for the HR, respectively).

Figures 13 and 15 provide clear evidence that in central Au+Au collisions, there is significant yield suppression in the HR and an enhancement in the SR. The suppression for the HR is consistent with a jet quenching scenario in which the HR yield at high p_T is dominated by radiated gluons and jets which survive passage through the medium. The enhancement for the SR could reflect the dissipative processes that redistribute the energy lost in the medium.

Several previous jet correlation measurements were carried out for an intermediate range of $p_T^a \otimes p_T^b$ [8, 17, 18, 19, 68, 70] and/or in a limited away-side integration window roughly equal to the HR [8, 12, 68, 70]. However, Fig. 15 shows that away-side yield modifications are sensitive to both p_T and the $\Delta\phi$ integration range. By choosing a certain p_T and $\Delta\phi$ range, the combined

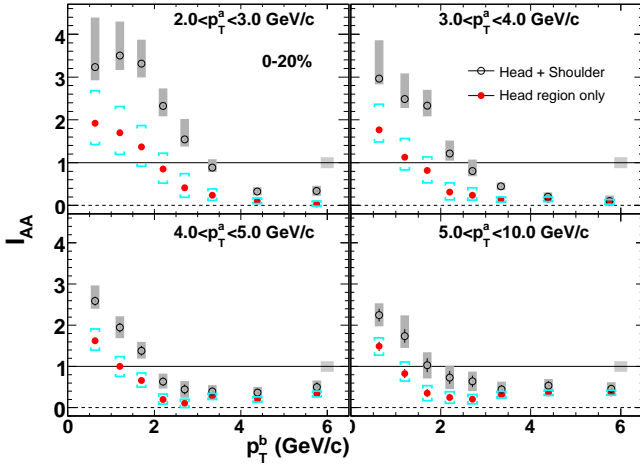


FIG. 13: (Color online) I_{AA} versus p_T^b for four trigger p_T bins in HR+SR ($|\Delta\phi - \pi| < \pi/2$) and HR ($|\Delta\phi - \pi| < \pi/6$) in 0-20% Au+Au collisions. The shaded bars and brackets represent the total systematic errors in the two regions. They are strongly correlated. Grey bands around $I_{AA} = 1$ represent 12% combined uncertainty on the single particle efficiency in Au+Au and $p + p$.

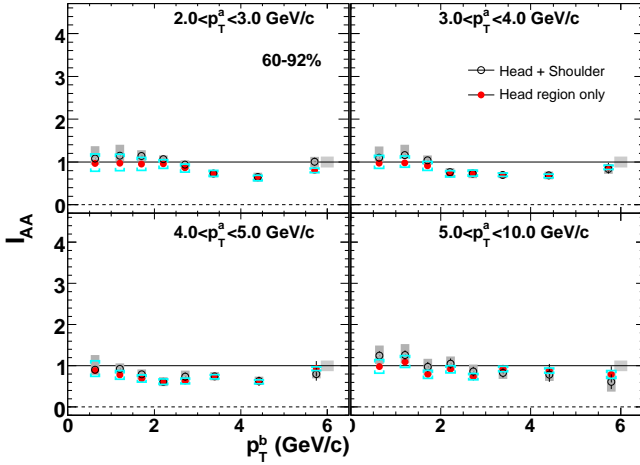


FIG. 14: (Color online) I_{AA} versus p_T^b for four trigger p_T bins in HR+SR ($|\Delta\phi - \pi| < \pi/2$) and HR ($|\Delta\phi - \pi| < \pi/6$) in 60-92% Au+Au collisions. The shaded bars and brackets represent the total systematic errors in the two regions. They are strongly correlated. Grey bands around $I_{AA} = 1$ represent 12% combined uncertainty on the single particle efficiency in Au+Au and $p + p$.

effect of SR enhancement and HR suppression can result in away-side yields that are almost independent of centrality, while their shapes still vary with centrality. Thus a detailed survey of the jet yield in a broad p_T and more differential study in $\Delta\phi$ for the away-side is important to obtain the full picture.

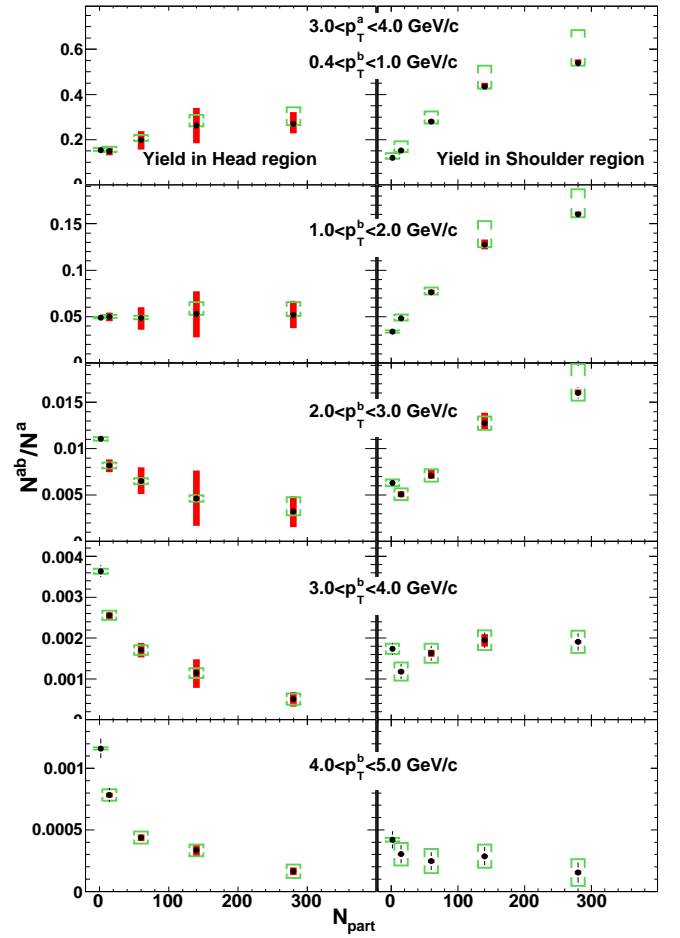


FIG. 15: (Color online) The per-trigger yield versus N_{part} in the HR (left panels) and the SR (right panels) for partner p_T in 0.4-1, 1-2, 2-3, 3-4, 4-5 GeV/c and fixed trigger in 3-4 GeV/c. The left most points are from $p + p$ collisions. The shaded bars (brackets) represent uncertainties due to elliptic flow (ZYAM procedure).

C. Medium Modification of Near-side Jets

In this section, we map out the p_T and centrality dependence of the shape and yields of the near-side jets.

1. Near-side jet shape

We characterize the near-side shape in $\Delta\phi$ by the Gaussian fit functions FIT1 and FIT2 described in Section IV B 1. The systematic uncertainties include the differences between FIT1 and FIT2 and the uncertainties associated with the elliptic flow subtraction. To account for a possible influence from feed-in of the shoulder component, we also performed fits to the near-side distribution with a single Gaussian function in $\pm 1\sigma$, $\pm 2\sigma$ and $\pm 3\sigma$ windows, where σ is the width of the near-side peak obtained with FIT2. Deviations from σ were added in quadrature to the total systematic errors. For $p + p$, a

simple fit with a near- and an away-side Gaussian plus a constant background was used.

Figure 16 compares the near-side Gaussian widths obtained for $p + p$ and 0-20% central Au+Au collisions. The results are shown as a function of partner p_T for four trigger p_T bins as indicated. The $p + p$ widths show the expected decrease with partner p_T for all trigger bins, as expected from a narrowing of the jet cone as p_T^b increases. The Au+Au widths also decrease with partner p_T except at low $p_T^{a,b}$. For low- p_T triggers of $2 < p_T^a < 3$ and $3 < p_T^a < 4$ GeV/c, the values for the widths are slightly below those for $p + p$ for $p_T^b < 1$ GeV/c; they are, however, significantly broader for $1 \lesssim p_T^b \lesssim 4$ GeV/c. For higher trigger p_T , the extracted widths are similar for Au+Au and $p + p$.

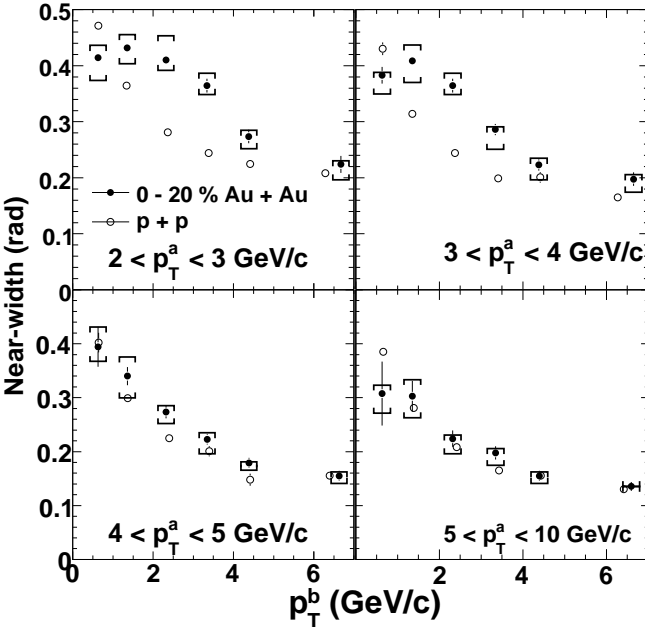


FIG. 16: Near-side Gaussian widths versus partner p_T for four trigger p_T ranges compared between 0-20 % Au+Au (solid circles) and $p + p$ (open circles).

Figure 17 shows the centrality dependence of the near-side widths for successively higher $p_T^a \otimes p_T^b$. For the lowest p_T bin of $2 - 3 \otimes 0.4 - 1$ GeV/c, the width decreases slightly with N_{part} and approaches a value of 0.4 radian in central collisions. A similar trend has been reported for measurements at low p_T [16]. For the $2 - 3 \otimes 2 - 3$ GeV/c selection, the near-side width grows with N_{part} , and approaches a value about 40% larger than the $p + p$ value for $N_{\text{part}} > 200$. For higher $p_T^a \otimes p_T^b$ bins, the near-side widths are narrower and their centrality dependence is flatter. For the $5 - 10 \otimes 5 - 10$ GeV/c bin, the near-side widths (~ 0.14 radian) are essentially independent of N_{part} , as might be expected if the near-side correlations are dominated by jet fragmentation.

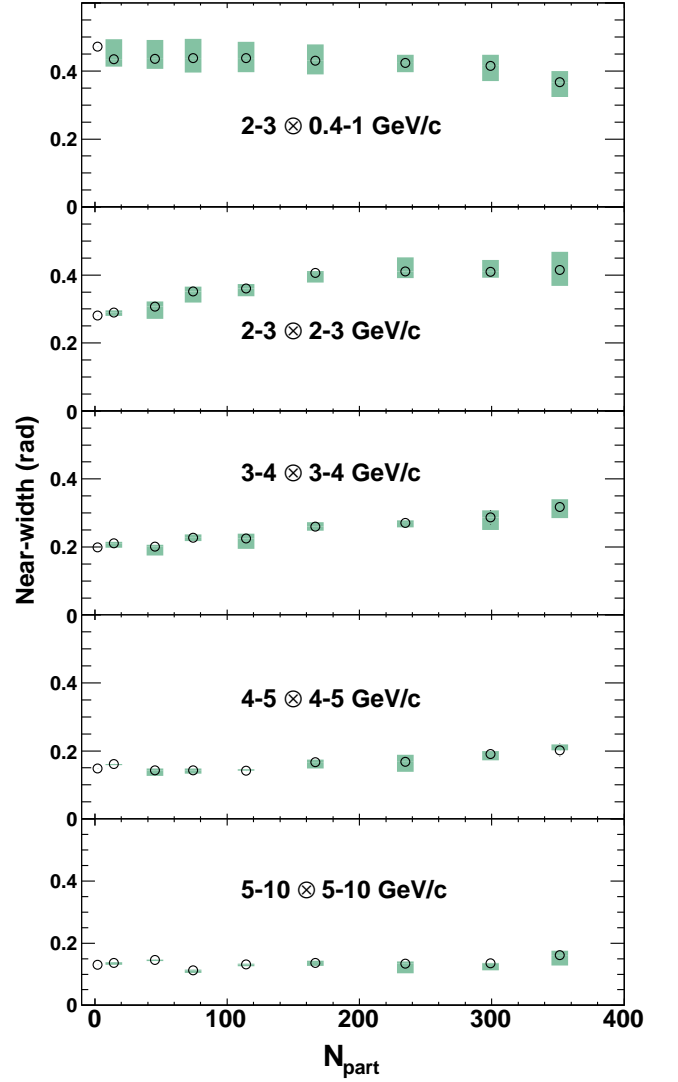


FIG. 17: (Color online) Near-side Gaussian widths versus N_{part} for five successively increasing $p_T^a \otimes p_T^b$. The most left point in each panel represents the value from $p + p$.

2. Near-side jet per-trigger yield

The near-side yield in $|\Delta\phi| < \pi/3$ (NR) as a function of partner p_T , is shown in Fig. 18 for $p + p$ and Au+Au collisions, for four trigger p_T bins. The corresponding results for the modification factor, I_{AA} , are shown in Fig. 19. For triggers of 2-3 GeV/c, I_{AA} is enhanced by more than a factor of two for $p_T^B < 2$ GeV/c, followed by a fall-off below unity for $p_T^B \gtrsim 4$ GeV/c. The overall deviation from $I_{AA} = 1$ decreases with increasing trigger p_T . For the highest p_T trigger, the near-side yield is close to that for $p + p$ over the full range of p_T^b . As a comparison, the I_{AA} values for the 60-92% centrality bin, shown in Fig. 20, are close to 1 for all $p_T^{a,b}$, suggesting a rather weak medium modification of the near-side yield in peripheral collisions.

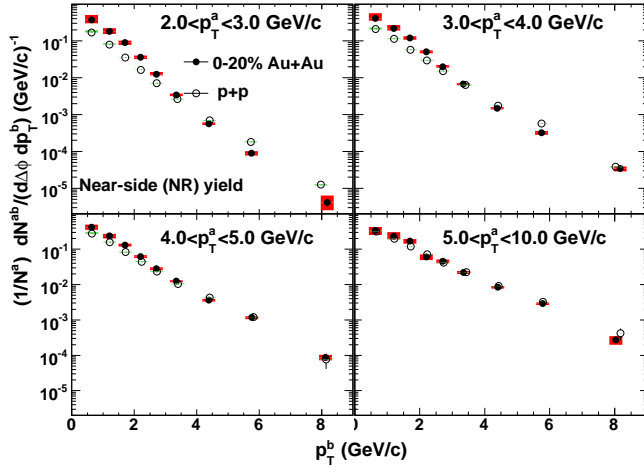


FIG. 18: (Color online) Near-side yield in $|\Delta\phi| < \pi/3$ versus partner p_T for four trigger p_T selections. The filled and open circles are for 0-20% Au+Au and $p + p$, respectively.

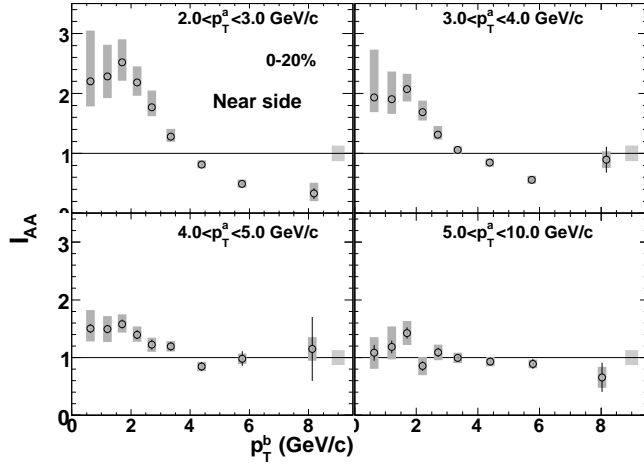


FIG. 19: Near-side I_{AA} in 0-20% Au+Au versus partner p_T for four trigger p_T bins. The shaded bars around the data points are the total systematic errors. Grey bands around $I_{AA} = 1$ represent 12% combined uncertainty on the single particle efficiency in Au+Au and $p + p$.

The patterns of the near-side jet shape and yields in Figs.16-20 suggest an influence from both medium modification and jet fragmentation at intermediate p_T . The influence of the medium has also been linked to a long range correlation component in $\Delta\eta$ [16, 17, 20]. This so called η “ridge” has been shown to be flat up to $|\Delta\eta| \sim 2$. The PHENIX $\Delta\eta$ acceptance is limited to $|\Delta\eta| < 0.7$. However, if contributions from the ridge are significant, they should show up in $\Delta\eta$ distributions.

Figure 21a shows a two-dimensional $\Delta\eta$ - $\Delta\phi$ correlation function for $2-3 \otimes 2-3$ GeV/c in 0-20% central Au+Au collisions. The $\Delta\eta$ range is displayed for $|\Delta\eta| < 0.5$ to suppress the relatively large statistical fluctuations at the edge of $\Delta\eta$ acceptance. The correlation function in Fig. 21a peaks along $\Delta\phi \sim 0$ and π , largely because of

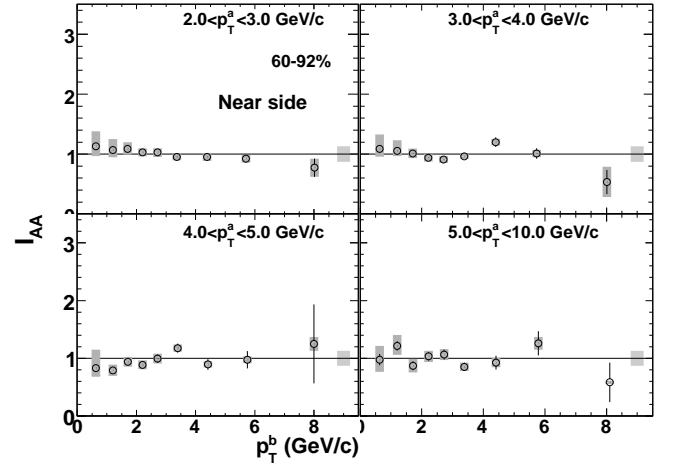


FIG. 20: Near-side I_{AA} in 60-92% Au+Au versus partner p_T for four trigger p_T bins. The shaded bars around the data points are the total systematic errors. Grey bands around $I_{AA} = 1$ represent 12% combined uncertainty on the single particle efficiency in Au+Au and $p + p$.

the elliptic flow modulation of the combinatoric pairs. To subtract the flow term, we assume that ξ and v_2 are identical to those used in our 1-D $\Delta\phi$ correlation analysis, and are constant for $|\eta| < 0.35$. The distribution after v_2 subtraction is shown in Fig. 21b. One can clearly see one near-side and two shoulder peaks (in $\Delta\phi$), which extend over the full range of $\Delta\eta$. However both $p+p$ and peripheral Au+Au collisions for the same p_T selections (Fig.22) show one near-side peak centered around $\Delta\eta \sim 0$ and one away-side peak elongated over $\Delta\eta$. These features are expected for fragmentation of back-to-back dijets in vacuum.

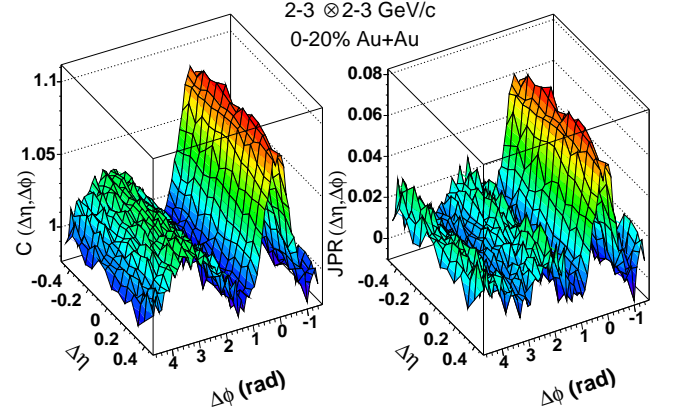


FIG. 21: (Color online) Correlation function (left panel, Eq. 8) and background subtracted hadron-pair ratio (right panel, Eq. 13) in $\Delta\eta$ and $\Delta\phi$ space for $2-3 \otimes 2-3$ GeV/c in 0-20 % Au+Au collisions.

To facilitate further detailed investigation, we focus on a near-side region defined by $|\Delta\phi| < 0.7$ and $|\Delta\eta| < 0.7$

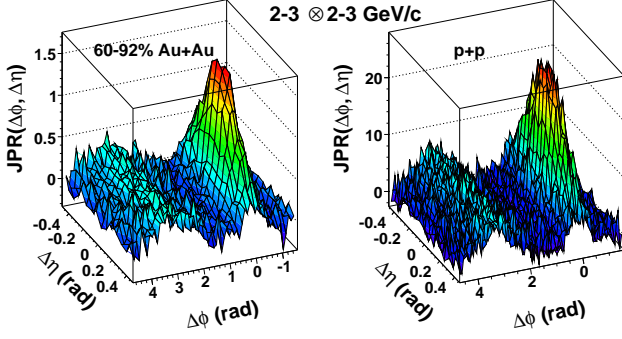


FIG. 22: (Color online) Background subtracted hadron-pair ratio (via Eq. 13) for $2-3 \otimes 2-3$ GeV/c in 60-92 % Au+Au (left panel) and p+p (right panel) collisions.

and study the projected distributions in $\Delta\phi$ and $\Delta\eta$. Figure 23 compares the $\Delta\eta$ distributions for $p+p$ and 0-20% central Au+Au collisions. The $p+p$ data indicate a relatively narrow jet-like peak for all four p_T selections. For the $2-3 \otimes 2-3$ GeV/c bin, the Au+Au data are enhanced and broadened relative to $p+p$. However, these differences gradually decrease toward higher p_T and essentially disappear for the $5-10 \otimes 5-10$ GeV/c bin. This possibly suggests that the ridge component at high p_T either disappears or becomes overwhelmed by the jet fragmentation component [71].

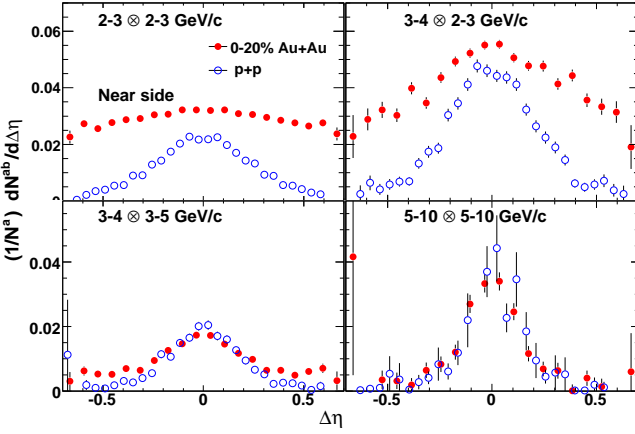


FIG. 23: (Color online) Per-trigger yield versus $\Delta\eta$ for $p+p$ (open symbols) and 0-20% central Au+Au (filled symbols) collisions. Results are shown for four $p_T^a \otimes p_T^b$ selections as indicated.

Figure 24 shows the comparison of the projected distributions in $\Delta\eta$ and $\Delta\phi$ for 0-20% central Au+Au collisions. By construction, the integrals of the two distributions are the same. For the $2-3 \otimes 2-3$ and $2-3 \otimes 3-4$ GeV/c bins, the distributions in $\Delta\eta$ are broader than in $\Delta\phi$. For the $3-4 \otimes 3-5$ and $5-10 \otimes 5-10$ GeV/c bins, the distributions become similar between $\Delta\phi$ and $\Delta\eta$. These observations suggest that the medium modifi-

cations are limited to $p_T^{a,b} \lesssim 4$ GeV/c, a similar p_T range in which the away-side is also strongly modified.

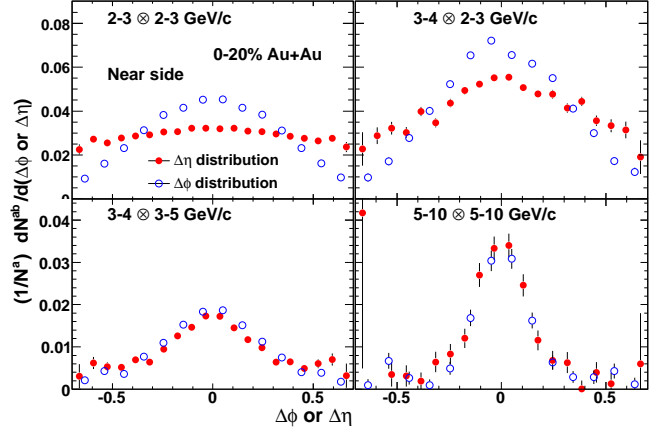


FIG. 24: (Color online) The projection of 2-D per-trigger yield in $|\Delta\eta| < 0.7$ $|\Delta\phi| < 0.7$ and 0-20% central Au+Au collisions onto $\Delta\phi$ (open symbols) and $\Delta\eta$ (filled symbols) for four $p_T^a \otimes p_T^b$ selections.

The evolution of the enhancement and broadening with the $p_T^{a,b}$ reflects the competition between contributions from the medium response and jet fragmentation. The former is important at $p_T^{a,b} \lesssim 4$ GeV/c and manifests itself as an enhanced and broadened distribution in $\Delta\eta$ and $\Delta\phi$. The latter dominates at higher p_T , reflected by $I_{AA} \approx 1$ and a near-side width similar to $p+p$. The strong modifications at intermediate p_T may reflect the remnants of those jets that interact with the medium, appearing as low p_T hadron pairs with modified width and multiplicity. Possible physics mechanisms for this parton-medium interaction include jet interaction with a longitudinal flowing medium [22, 23, 27], position-momentum correlations induced by radial flow [21], correlation between radial flow boosted beam jet and medium suppressed transverse jet [26], plasma instability [24, 25], or back-splash caused by the quenched jets [28]. However, the modification mechanisms for the near- and away-side may be related: both near- and away-side distributions show enhancement and broadening in the lower range $p_T < 4$ GeV/c, above which the jet characteristics qualitatively approach the jet fragmentation.

D. Away- and Near-side Spectral Slopes

To further explore the differences between the NR, HR and SR, we compare the shapes of the partner p_T spectra in these three $\Delta\phi$ regions. To do this, we characterize the local inverse slope of the spectra via a truncated mean p_T in a given p_T range,

$$\langle p'_T \rangle \equiv \langle p_T^b \rangle_{p_T^{\min} < p_T^b < p_T^{\max}} - p_T^{\min}. \quad (26)$$

where $\langle p'_T \rangle$ is calculated from the jet yields shown in Fig. 12 and Fig. 18. For an exponential spectrum with

an inverse slope of T and $T \ll p_T^{\max} - p_T^{\min}$, $\langle p'_T \rangle \approx T$.

First, we focus on an intermediate p_T region, $1 < p_T^b < 5$ GeV/c, where the medium-induced contributions are important for the near- and away-side yields. Figure 25 shows values of $\langle p'_T \rangle$ for the HR, SR and NR as a function of N_{part} . For all trigger p_T bins, the values for the NR drop slightly with centrality to a lower level relative to $p + p$. This can be understood from the shape difference in Fig. 19, where the Au+Au spectra drop faster with increasing p_T^b . For $3 < p_T^a < 4$ GeV/c, a factor of two decrease in 1 - 5 GeV/c amounts to a reduction of ~ 0.1 GeV/c in $\langle p'_T \rangle$.

Despite the small decrease with N_{part} , the overall average level of $\langle p'_T \rangle$ for the NR for $N_{\text{part}} > 100$ increases with trigger p_T . They are $0.533 + 0.024 - 0.016$, $0.605 + 0.033 - 0.023$, $0.698 + 0.03 - 0.04$ GeV/c and $0.797 + 0.052 - 0.042$ GeV/c for triggers in 2-3, 3-4, 4-5 and 5-10 GeV/c, respectively. This trend is consistent with the dominance of jet fragmentation on the near-side, i.e. a harder spectrum for partner hadrons is expected for higher p_T trigger hadrons.

Values for the SR also show an almost flat centrality dependence for $N_{\text{part}} \gtrsim 100$. In this case, the values for $\langle p'_T \rangle$ are lower (≈ 0.45 GeV/c, see Table. V) and they do not depend on the trigger p_T . They are, however, larger than the values obtained for inclusive charged hadrons (0.36 GeV/c as indicated by the solid lines) [7]. The relatively sharp change in $\langle p'_T \rangle$ for $N_{\text{part}} \lesssim 100$ may reflect the dominance of jet fragmentation contribution in peripheral collisions.

The values of $\langle p'_T \rangle$ for the HR show a gradual decrease with N_{part} . They start at a level close to the values for the near-side, and gradually decrease with increasing N_{part} , consistent with a softening of the partner spectrum in central collisions. For 2-3 and 3-4 GeV/c trigger bins, the values of $\langle p'_T \rangle$ for $N_{\text{part}} \gtrsim 150$ approach those for inclusive spectra. For higher trigger p_T bins, the drop with N_{part} is less dramatic, possibly due to punch-through jet fragmentation contribution at high p_T .

To further investigate the onset of the jet fragmentation in the HR, we study the dependence of $\langle p'_T \rangle$ on partner momentum. Figure 26 shows the centrality dependence of $\langle p'_T \rangle$ calculated in various ranges of p_T^b for triggers in 3-4 GeV/c (left panels) and 4-5 GeV/c (right panels). These results are compared with values for inclusive hadron spectra calculated in the same p_T^b ranges. For $1 < p_T^b < 7$ GeV/c bin, $\langle p'_T \rangle$ decreases with N_{part} . As the p_T^b range shifts upward, the centrality dependence becomes flatter. $\langle p'_T \rangle$ for $3 < p_T^b < 7$ GeV/c is essentially constant with N_{part} . The flattening of the spectral slope with N_{part} starts at a lower p_T^b for $4 < p_T^a < 5$ GeV/c than that for $3 < p_T^a < 4$ GeV/c. This implies (1) a similar spectra shape for Au+Au and $p + p$ at high $p_T^{a,b}$, and (2) the jet fragmentation contribution dominates the HR yield at large $p_T^{a,b}$.

The different patterns observed for the yields in the HR and SR suggest a different origin for these yields.

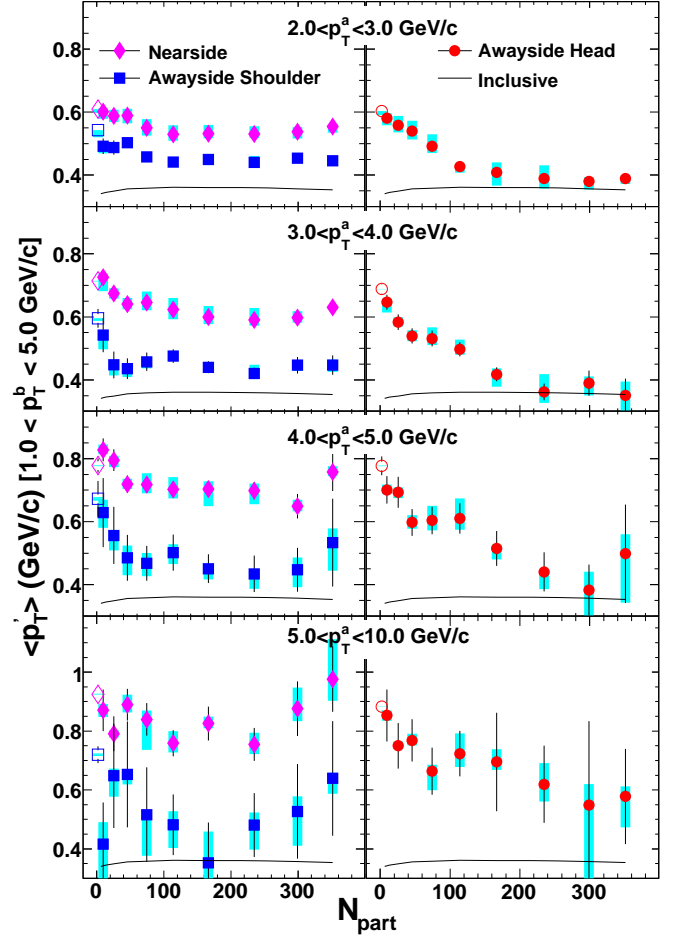


FIG. 25: (Color online) Truncated mean p_T , $\langle p'_T \rangle$, in $1 < p_T^b < 5$ GeV/c versus N_{part} for the near-side (diamonds), away-side shoulder (squares) and head (circles) regions for Au+Au (filled) and $p + p$ (open) for four trigger p_T bins. Solid lines represent values for inclusive charged hadrons (~ 0.36 GeV/c) [7]. Error bars represent the statistical errors. Shaded bars represent the sum of N_{part} -correlated elliptic flow and ZYAM error.

TABLE V: Truncated mean p_T , $\langle p'_T \rangle$, calculated for $1 < p_T^b < 5$ GeV/c and averaged for $N_{\text{part}} > 100$ in the NR and SR for various bins of trigger p_T .

p_T^a range (GeV/c)	NR $\langle p'_T \rangle$ (GeV/c)	SR $\langle p'_T \rangle$ (GeV/c)
2-3	$0.533 + 0.024 - 0.016$	$0.445 + 0.013 - 0.007$
3-4	$0.605 + 0.033 - 0.023$	$0.443 + 0.018 - 0.018$
4-5	$0.698 + 0.030 - 0.040$	$0.461 + 0.031 - 0.051$
5-10	$0.797 + 0.052 - 0.042$	$0.478 + 0.079 - 0.139$

The suppression of the HR yield and the softening of its spectrum are consistent with jet quenching. The observed HR yield could be comprised of contributions from “punch-through” jets, radiated gluons and feed-in from the SR. By contrast, the enhancement of the SR yield for $p_T^{a,b} \lesssim 4$ GeV/c suggests a remnant of the lost energy from quenched jets. The very weak dependence on

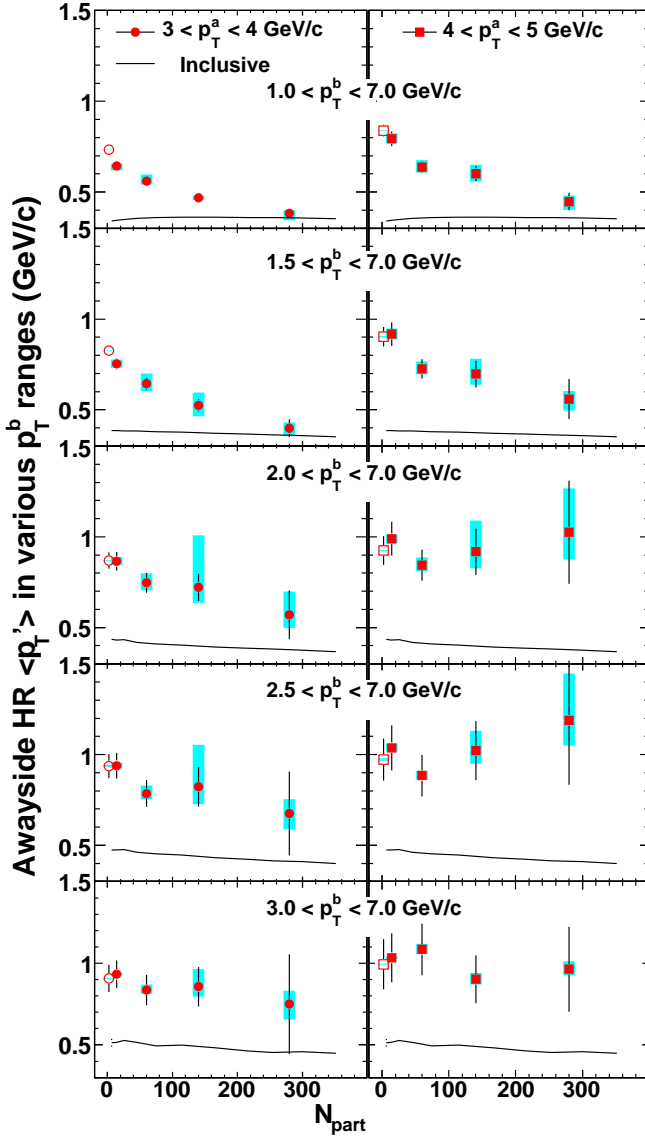


FIG. 26: (Color online) Truncated mean p_T , $\langle p'_T \rangle$, calculated for five partner p_T ranges (from top to bottom) in the HR. The left panels (right panels) shows the results for triggers in 3–4 (4–5) GeV/c. Solid lines represent values for inclusive charged hadrons. Error bars represent the statistical errors. Shaded bars represent the sum of N_{part} -correlated elliptic flow and ZYAM error.

p_T and centrality (for $N_{\text{part}} \gtrsim 100$) for its peak location and mean p_T may reflect an intrinsic response of the medium to the lost energy. These observations are challenging for simple deflected jet scenarios [23, 29], since both the deflection angle and jet spectral slope would depend on p_T^a or p_T^b . On the other hand, they are consistent with expectations for Mach-shock in a near-ideal hydrodynamical medium [35, 72], and thus they can be used to constrain the medium transport properties such as speed of sound and viscosity to entropy ratio within these models.

E. Medium Modification of Hadron Pair Yield

In $p + p$ collisions at 200 GeV, it is generally believed that hadrons for $p_T > 2$ GeV/c are dominated by jet fragmentation [73]. By contrast, particle production in heavy-ion collisions is complicated by final-state medium effects. Due to strong jet quenching, jet fragmentation contribution only dominates for $p_T \gtrsim 5-7$ GeV/c [7, 11]. The bulk of hadrons, i.e. those at $p_T \lesssim 4$ GeV/c, are dominated by soft processes such as the hydrodynamic flow of locally thermalized partonic medium [37, 74, 75] which subsequently hadronize via coalescence of constituent quarks [38, 39, 40, 41]. The p_T of $4 \lesssim p_T \lesssim 7$ GeV/c is a transition region where both soft and hard processes contribute.

Dihadron correlations provide new tools for separating the hard and soft contributions at low and intermediate p_T , albeit for hadron pair production instead of single hadron production. If jets are quenched by the medium and their energy is transported to lower p_T , a significant fraction of the low and intermediate p_T hadron pairs may retain some correlation with the original jet [42]. Consequently, they can contribute to a dihadron correlation analysis. However such pairs can also be influenced by soft processes which dominate the inclusive hadron production in the same p_T region. For instance, they may couple with hydrodynamical flow at the partonic stage [23] or reflect the effects of the coalescence between shower parton and thermal partons during hadronization [39].

Thus far, we have quantified the jet modifications via per-trigger yields. While sensitive to modifications of jet-induced pairs, these yields are also sensitive to modifications in the number of triggers. For high- p_T triggers, however, the per-trigger yield is roughly equal to per-jet yield, because most jets fragment into at most one trigger hadron due to the steeply falling jet spectra [44]. For intermediate and low- p_T triggers, a large fraction of triggers may come from soft processes, and hence “dilute” the per-trigger yield.

To illustrate this dilution effect, we focus on the near-side jet-induced pairs in which the first hadron is fixed in the 5-10 GeV/c p_T range, and the second hadron is varied in p_T from 0.4 to 7 GeV/c. We note here that the requirement of a high- p_T hadron ensures that most of the near-side pairs come from fragmentation of partons. Figure 27a shows the per-trigger yield modification factor I_{AA} when hadrons in the 5-10 GeV/c p_T range are designated triggers; Fig. 27b shows the corresponding I_{AA} when the lower- p_T hadrons are designated as triggers, which is calculated according to Eq. 7.

Figure 27a shows that I_{AA} is near unity for all p_T^b for the 5-10 GeV/c hadron triggers. This is consistent with each high- p_T trigger coming from one jet. On the other hand, when low- p_T hadrons are used as triggers, Fig. 27b shows that I_{AA} has a non-trivial dependence on p_T^a . That is, there is a strong suppression of I_{AA} in the 2-4 GeV/c p_T range, which reflects an excess of trigger hadrons at

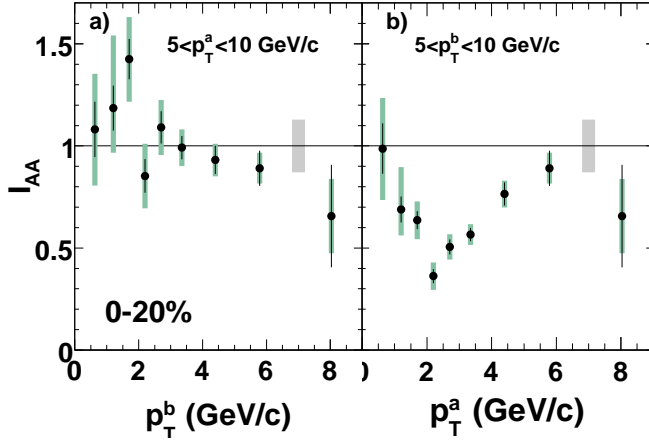


FIG. 27: (Color online) a) I_{AA} versus partner p_T when 5-10 GeV/c hadrons are designated triggers. b) I_{AA} versus trigger p_T when 5-10 GeV/c hadrons are used as partners.

low p_T with weaker jet correlation strength. This dilution effect is also reflected in the near-side I_{AA} values in Fig. 19 and for the away-side I_{AA} values in Fig. 13 (also reflected in Fig. 36 for low p_T^a and high p_T^b). The former shows a suppression at large p_T^b for soft triggers ($2 < p_T^a < 3$ and $3 < p_T^a < 4$ GeV/c). The latter shows a stronger suppression for low- p_T triggers ($2 < p_T^a < 3$ and $3 < p_T^a < 4$ GeV/c) than for high- p_T triggers ($4 < p_T^a < 5$ and $5 < p_T^a < 10$ GeV/c). This dilution effect might be the result of the following two scenarios: 1) a large fraction of low- p_T hadrons are from soft processes such as coalescence of flow-boosted thermal quarks related to the anomalous proton/pion ratio [7, 11], or 2) jets are quenched and these hadrons are the remnants of the quenched jets, and thus lack associated hadrons at high p_T .

To gain more insights on intermediate- p_T correlations, we focus on the pair suppression factor J_{AA} defined in Eq. 4. We recall here that J_{AA} quantifies the modification of jet-induced pairs in Au+Au relative to that in $p + p$ normalized by N_{coll} . It is symmetric with respect to the interchange of p_T^a and p_T^b and equals one in the absence of medium effects. Figure 28 shows the near-side J_{AA} as function of p_T^b for 0-20% central Au+Au collisions and for four different p_T^a bins. Values of J_{AA} are above one for $p_T^{a,b} < 2$ GeV/c. However, they decrease with increasing $p_T^{a,b}$ and drop below one. For high $p_T^{a,b}$, J_{AA} reaches a constant value $\sim 0.2 - 0.3$, which is similar to the high- p_T single particle suppression factor R_{AA} .

To interpret these observations, we note that each high p_T pair at the near-side comes from the same jet. Thus J_{AA} reflects the modification of single jets, which at high p_T should be the same as leading hadron R_{AA} . Since the values of R_{AA} is constant at high p_T , we expect high- p_T J_{AA} to be constant and equal to R_{AA} .

Furthermore, if each high- p_T near-side pair comes from the same jet, then the sum of their transverse momentum, $p_T^{sum} = p_T^a + p_T^b$, should serve as a better proxy for

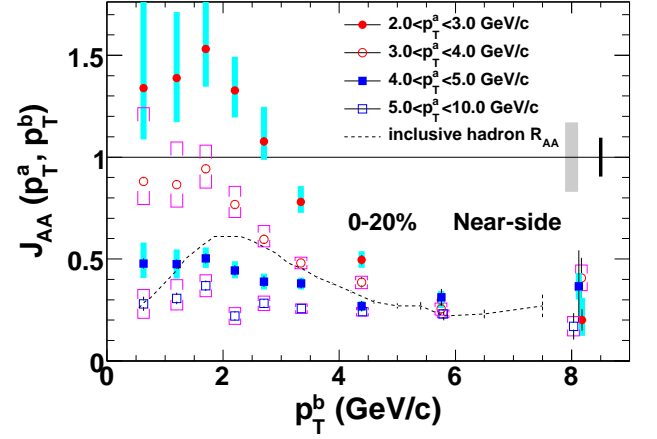


FIG. 28: (Color online) The near-side pair suppression factor J_{AA} in 0-20% Au+Au collisions as function of p_T^b for various ranges of p_T^a . The dashed line indicate the charged hadron R_{AA} . The grey band around one is the systematic error due to the 20% combined single particle efficiency of the triggers and partners in Au+Au and $p + p$. The dark line around one indicate the uncertainty on the N_{coll} .

the original jet energy. With this in mind, we re-plot in Fig. 29 the near-side J_{AA} values as a function of this “pair proxy energy” p_T^{sum} . Interestingly, the pair modification factors roughly follow a single curve in p_T^{sum} . It is above 1 below 5 GeV/c, followed by a decrease with p_T^{sum} , and reaches a constant for $p_T^{sum} > 8$ GeV/c. The approximate scaling behavior breaks when the p_T of one hadron is $\lesssim 2$ GeV/c, where J_{AA} is systematically below the overall trend.

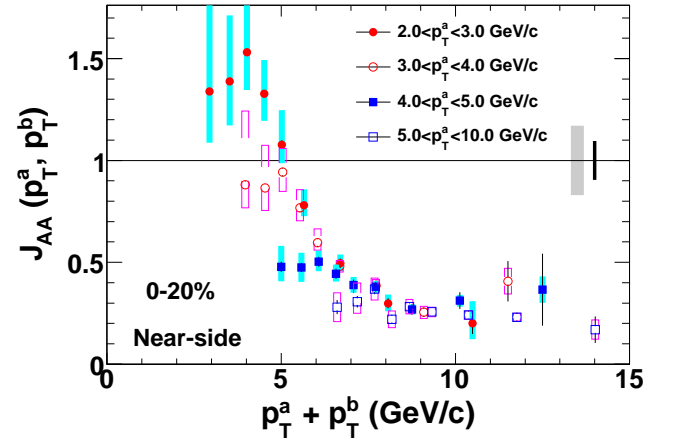


FIG. 29: (Color online) Near-side pair suppression factor J_{AA} as function of pair transverse momentum, $p_T^{sum} = p_T^a + p_T^b$ in 0-20% Au+Au collisions. The grey band around one is the systematic error due to the 20% combined single particle efficiency of the triggers and partners in Au+Au and $p + p$. The dark line around one indicate the uncertainty on the N_{coll} .

The fact that $J_{AA} > 1$ for $p_T^{\text{sum}} < 5 \text{ GeV}/c$ implies that the total jet-induced pair yield is enhanced relative to the N_{coll} scaled $p+p$ collisions. This enhancement may reflect the energy of the quenched jets being transported to low p_T . J_{AA} is almost a factor of 6-7 larger than its high p_T^{sum} limit. By contrast, the enhancement shown for I_{AA} in Fig. 19 is only a factor of 2.5 at low $p_T^{a,b}$. This difference can be attributed to the dilution effect on the triggers. For completeness, Fig. 30 shows the values of J_{AA} versus p_T^b (left panels) and p_T^{sum} (right panels) for 20-40%, 40-60% and 60-92% centrality bins. J_{AA} versus p_T^{sum} shows an approximate scaling behavior for all centralities i.e., J_{AA} for large p_T^{sum} approaches a constant level roughly equal to that for the high- p_T R_{AA} values.

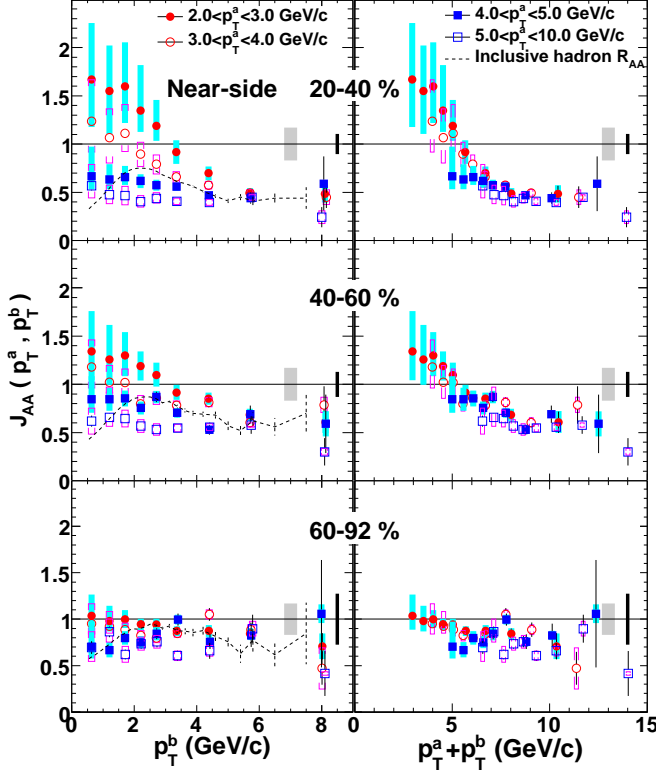


FIG. 30: (Color online) The near-side J_{AA} as function of p_T^b (left panels) and p_T^{sum} (right panels) for four p_T^a bins and three centrality bins. From top to bottom are 20-40%, 40-60% and 60-92 %. The dashed lines in the left panels indicate the charged hadron R_{AA} . The grey bands around one is the systematic error due to the 17% combined single particle efficiency of the triggers and partners in Au+Au and $p+p$. The dark line around one indicate the uncertainty on the N_{coll} .

In Fig. 31 we show the J_{AA} for the away-side HR as a function of p_T^b in various centrality bins. In central collisions, a possible enhancement at low p_T^b and a strong suppression at large p_T^b can be seen. This is consistent with the feedback of lost energy to lower p_T on the away-side. The modifications decrease for peripheral collisions, as expected for a weaker medium effect. However, the suppression level seems to approach a constant value

TABLE VI: The average ratio J_{AA}/R_{AA}^2 for the away-side HR for $4 < p_T^b < 7 \text{ GeV}/c$ (see Fig. 31).

Centrality	J_{AA}/R_{AA}^2 for HR ($\pm \text{Stat} + \text{Sys-Sys}$)
0-20%	$0.81 \pm 0.07 + 0.44 - 0.41$
20-40%	$0.89 \pm 0.05 + 0.37 - 0.35$
40-60%	$0.80 \pm 0.03 + 0.26 - 0.23$
60-92%	$0.90 \pm 0.03 + 0.25 - 0.23$

for high p_T^b for all centralities. This is expected since $I_{AA} \approx R_{AA}$ at high p_T for the away-side HR. This implies that $J_{AA} = I_{AA} R_{AA} \approx R_{AA}^2$ when one of the hadrons is at high p_T , as indicated by the dashed line.

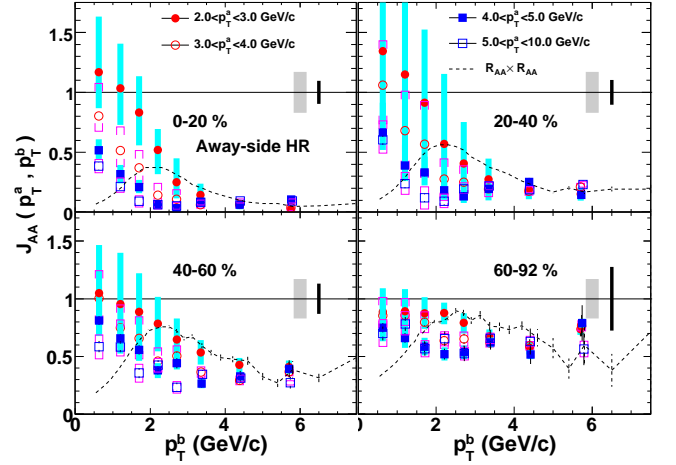


FIG. 31: (Color online) The pair suppression factor J_{AA} for the away-side HR in Au+Au collisions as function of p_T^b for various ranges of p_T^a . The dashed line indicate square of the charged hadron R_{AA} . The grey bands around one is the systematic error due to the combined single particle efficiency of the two particles in Au+Au and $p+p$. The dark line around one indicate the uncertainty on the N_{coll} .

To quantify this high- p_T scaling behavior, we calculate the ratio $\frac{J_{AA}}{R_{AA}^2}$ for away-side head region for $4 < p_T^b < 7 \text{ GeV}/c$ and various p_T^a selections. The values for the four centrality ranges used in Fig.31 are summarized in Table.VI. Although the uncertainties are quite substantial, the HR J_{AA} approximately equals R_{AA}^2 , suggesting a similar suppression factor for inclusive hadrons and away-side jet at high p_T . This, as pointed out in Ref. [76, 77], could be a canceling effect between a stronger energy loss which increase the suppression, and a harder away-side hadron spectra associated with high- p_T triggers which decrease the suppression.

V. DISCUSSION

A. Insights from Identified Particle and Energy Dependent Correlations

To elucidate the underlying physics of the medium-induced component, we focus on intermediate p_T where the SR dominates, and study the particle composition of the yield in the SR. PHENIX has published results on correlations of a trigger hadron, at intermediate transverse momentum ($2.5 < p_T^a < 4$ GeV/c), with identified partner mesons or baryons at lower p_T [43]. The away-side shape was found to be similar for partner baryons and mesons; namely, the pairs peak at $\Delta\phi \sim \pi \pm 1.1$ with a local minimum at $\Delta\phi \sim \pi$. The particle composition in the away-side jet, as reflected by the baryon to meson ratio, was also found to grow with increasing partner p_T . The trend is similar to that observed for inclusive hadron production. These observations for intermediate p_T correlations are consistent with strong parton-medium interactions which induce correlations between soft partons, followed by coalescence at hadronization.

Further insight into the physics underlying the SR yield can be obtained by studying its energy dependence. In particular, it is interesting to see whether the two-component picture applies at much lower collision energy. Figure 32 compares the per-trigger yield at $\sqrt{s_{NN}} = 200$ and 62.4 GeV for $1 < p_T^b < 2.5 < p_T^a < 4$ GeV/c. They are the yields associated with the jet functions previously published in [19]. The away-side shapes are strongly non-Gaussian in both cases. The 62.4 GeV data seems to be somewhat flatter, however, its relatively large statistical uncertainties do not allow a definite statement.

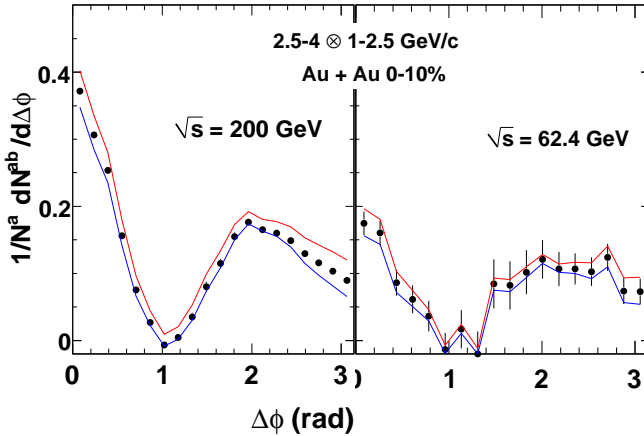


FIG. 32: (Color online) Per-trigger yield in 0-10% central Au+Au collisions from PHENIX at (a) $\sqrt{s_{NN}} = 200$ GeV and (b) $\sqrt{s_{NN}} = 62.4$ GeV. The histograms show the combined uncertainty of the elliptic flow and ZYAM errors.

The CERES collaboration has recently released their high-statistics preliminary results of per-trigger yields in 0-5% and 5-10% Pb+Au collisions for $1 < p_T^b < 2.5 < p_T^a < 4$ GeV/c [78]. This measurement was carried out

at $\sqrt{s_{NN}} = 17.2$ GeV at the SPS, for $0.1 < \eta < 0.7$ in the center of mass (CM) frame. The equivalent pseudo-rapidity window of 0.6 is close to the value of 0.7 for PHENIX. Thus, the jet yields from both experiments can be compared after applying the correction of $0.7/0.6 = 1.17$. In contrast to the PHENIX results, the CERES data show an essentially flat away-side jet shape. The maximum of SR is about half that of the PHENIX value, whereas the yield at the HR is close to the PHENIX value. The former might suggest a weaker medium effect at lower energy; the latter could be a combination of a lower jet multiplicity and a weaker jet quenching at SPS energy. However, it is conceivable that other nuclear effects, especially Cronin effect [79], may also broaden the away-side jet shape. Further detailed study of the collision energy dependence of the HR and the SR components might elucidate the onset of jet quenching and medium response.

B. Comparison with models

If jets are generated close to the surface, they exit and subsequently fragment outside the medium. Otherwise, they lose energy by radiating gluons. These shower gluons may be emitted at large angles relative to the original partons [31, 32] and fragment into hadrons, or they can be deflected to large angles by interactions with medium. Examples of the latter include medium deflection in the azimuthal [23, 29] and the beam directions [25] or excitation of collective Mach shock [35, 36];

Several calculations for radiative energy loss have been carried out [14, 31, 77] to describe dihadron production at high p_T . They all describe the data fairly well. As an example, Fig. 33 shows a comparison of data for the 4-5 and 5-10 GeV/c triggers with recent calculations from Ref. [77]. For $p_T^a > 2$ GeV/c, the calculated I_{AA} is approximately constant and agrees well with the data. According to this calculation, both tangential and punch-through jet emission are important, accounting for 3/4 and 1/4 of the away-side high- p_T pairs, respectively.

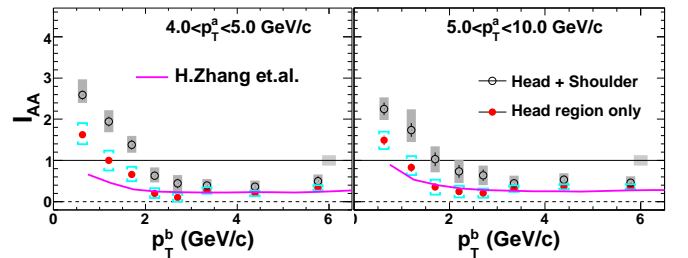


FIG. 33: (Color online) Comparison of I_{AA} with energy loss calculation from Ref. [77].

To extend the calculation to the low and intermediate p_T , contributions from radiated gluons have to be taken into account. Early energy loss model calculations suggested that these radiated gluons are almost collinear

with the jet axis [80]. However, recent calculations [31] favor large angle gluon emission due to destructive interference that suppresses collinear emission. By including gluon feedback, the calculation can reproduce away-side per-trigger yields at low partner p_T , but the gluon emission angle is too small to reproduce the away-side jet shape.

In an improved calculation that includes the Sudakov form factors [32], the authors can qualitatively describe the away-side jet shape and its centrality dependence at intermediate p_T , when the leading parton is assumed to split into two semi-hard gluons which then fragment into hadrons. This model assumes a transport coefficient of $\hat{q} \sim 5 - 10 \text{ GeV}^2/\text{fm}$. A smaller \hat{q} , for instance, would substantially reduce the predicted split angle.

The away-side broadening may also arise from Cherenkov gluon radiation [34]. It could occur when the gluon is scattered by colored bound states in such a way that the permittivity for in-medium gluons becomes space-like. A first calculation that includes only scalar bound states suggests that the peak angle D should gradually decrease to zero with increasing momentum; this trend seems to be ruled out by the present data. More sophisticated calculations including other bound states are needed in future studies.

It was suggested that shower partons could couple with the longitudinal and transverse flow, and are broadened or deflected in $\Delta\eta$ [21, 22, 23, 27] and/or $\Delta\phi$ [23, 29] directions. The longitudinal deflection was argued to be responsible for the $\Delta\eta$ ridge structure at the near-side. The transverse deflection can lead to broadening in $\Delta\phi$. It was argued in [29] that a random multiple scattering of the leading parton, combined with energy loss, can result in the double peaked structure of the away-side. However, in general, the deflection angle decreases with the hadron momentum. This is not compatible with the observation of p_T -independent D values and universal spectral slopes of the SR.

Finally, it has been proposed that the lost energy can be absorbed by the medium and converted into collective Mach shock [35, 36]. In this picture, the fluid elements are boosted along the Mach angle [72] and then hadronize via coalescence. The Mach angle depends only on the sound speed of the medium thus is independent of p_T and consistent with the data. The boost effect also produces a harder slope for the partners, qualitatively consistent with experimental observations. Our results on the PID dependence of the correlation pattern [43] are consistent with the above picture. The propagation of the shock wave requires hydrodynamical behavior of the medium with small viscosity. If the Mach-shock is the underlying physics, the observation can be used to constrain the value of η/s .

Many of the models discussed in this section are quite qualitative in nature. These models typically focus on either jet shape or jet yield, near-side or away-side, high p_T or low p_T . The fact that both near- and away-side distributions are enhanced and broadened at low p_T and

that the modifications limited to $p_T \lesssim 4 \text{ GeV}/c$, above which the jet characteristics qualitatively approach jet fragmentation, may suggest that the modification mechanisms for the near- and away-side are related. A model framework including both jet quenching and medium response, which can describe the full p_T evolution of the jet shape and yield at both near- and away-side is required to understand the parton-medium interactions. Our data provide valuable guidance for such future model developments.

VI. SUMMARY AND CONCLUSIONS

We have analysed dihadron azimuthal correlations for $0.4 < p_T < 10 \text{ GeV}/c$ unidentified charged hadrons in Au+Au collisions at $\sqrt{s_{NN}} = 200 \text{ GeV}$. The results are presented as functions of trigger p_T , partner p_T and centrality, and are compared with correlations of identified hadrons as well as results from lower energies. The evolution of the jet shape and yield with p_T seems to suggest four distinct contributions to jet-induced pairs: 1) a jet fragmentation component around $\Delta\phi \sim 0$, 2) a punch-through jet fragmentation component around $\Delta\phi \sim \pi$, 3) a medium-induced component around $\Delta\phi \sim 0$, and 4) a medium-induced components around $\Delta\phi \sim \pi \pm 1.1$.

The jet fragmentation components arise from jets that suffer small energy loss due to the surface or punch-through jet emissions. They dominate the near- and away-side pairs at large p_T . The near-side pair suppression factor J_{AA} follows an approximate scaling with the pair proxy energy p_T^{sum} . It reaches a constant for $p_T^{\text{sum}} > 8 \text{ GeV}/c$, at a level similar to the suppression for single jets at high p_T . In this p_T region, the yield of both the single jets (near-side pairs) and back-to-back jets (away-side pairs) are consistent with energy loss calculations.

By contrast, the enhancement of medium-induced components may reflect a remnant of the lost energy from quenched jets. This enhancement is limited to $p_T^{A,B} \lesssim 4 \text{ GeV}/c$. The near-side medium-induced component is responsible for broadening in $\Delta\phi$ and significant elongation in $\Delta\eta$, and is related to the ridge structure in [16, 17, 20]. The away-side medium-induced component exhibits p_T - and centrality-independent shape and mean p_T , and a bulk-medium like particle composition [43], possibly reflecting an intrinsic property of the medium response to energetic jets.

We have also investigated the contribution of medium-induced components to single particle production at intermediate p_T , where soft processes such as hydrodynamical flow and coalescence are important. The yields of jet-induced hadron pairs (via J_{AA}) are not suppressed at low pair proxy energy $p_T^{\text{sum}} = p_T^a + p_T^b$. However, pair yields divided by the yield of soft triggers show an apparent dilution effect at large partner p_T . This suggests that these soft hadrons either come from soft processes such as from coalescence of thermal partons, or they are the remnant of quenched jets, and thus lack high- p_T jet

partners.

VII. ACKNOWLEDGEMENTS

We thank the staff of the Collider-Accelerator and Physics Departments at Brookhaven National Laboratory and the staff of the other PHENIX participating institutions for their vital contributions. We thank Hanzhong Zhang and XinNian Wang for providing theoretical calculation input. We acknowledge support from the Department of Energy, Office of Science, Office of Nuclear Physics, the National Science Foundation, Abilene Christian University Research Council, Research Foundation of SUNY, and Dean of the College of Arts and Sciences, Vanderbilt University (U.S.A), Ministry of Education, Culture, Sports, Science, and Technology and the Japan Society for the Promotion of Science (Japan), Conselho Nacional de Desenvolvimento Científico e Tecnológico and Fundação de Amparo à Pesquisa do Estado de São Paulo (Brazil), Natural Science Foundation of China (People's Republic of China), Ministry of Education, Youth and Sports (Czech Republic), Centre National de la Recherche Scientifique, Commissariat à l'Énergie Atomique, and Institut National de Physique Nucléaire et de Physique des Particules (France), Ministry of Industry, Science and Technologies, Bundesministerium für Bildung und Forschung, Deutscher Akademischer Austausch Dienst, and Alexander von Humboldt Stiftung (Germany), Hungarian National Science Fund, OTKA (Hungary), Department of Atomic Energy (India), Israel Science Foundation (Israel), Korea Research Foundation and Korea Science and Engineering Foundation (Korea), Ministry of Education and Science, Russia Academy of Sciences, Federal Agency of Atomic Energy (Russia), VR and the Wallenberg Foundation (Sweden), the U.S. Civilian Research and Development Foundation for the Independent States of the Former Soviet Union, the US-Hungarian NSF-OTKA-MTA, and the US-Israel Binational Science Foundation.

APPENDIX A: DIHADRON CORRELATION METHOD

This section demonstrates that the shape of the $\Delta\phi$ correlation function, constructed as the ratio of same- to mixed-event, reproduces the shape of the true-pair distribution in $\Delta\phi$. We demonstrate this is generally true for a non-uniform experimental acceptance such as in PHENIX. Our argument is not original with our analysis, but has been used numerous times before in correlation analyses in heavy-ion experiments.

We start by giving notation for the true distributions

of type a and type b particles. They are

$$\frac{d^2 N_0^{ab}}{d\phi^a d\phi^b}, \quad \frac{dN_0^a}{d\phi^a}, \quad \frac{dN_0^b}{d\phi^b} \quad (A1)$$

for the true azimuthal distributions for ab pairs and a , b singles produced for PHENIX pseudo-rapidity acceptance and for events in one centrality bin. We use superscript “0” to indicate the true distributions. The *true* distributions are for particles in PHENIX η range, but with full azimuthal coverage.

The PHENIX Beam-Beam Counter (BBC) and Zero-Degree Calorimeter (ZDC), which trigger on events and determine their centrality, are uniform in azimuth. Therefore the *true* singles distributions are uniform, and the *true* pair distribution depends only on the difference between the two angles:

$$\frac{d^2 N_0^{ab}}{d\phi^a d\phi^b} = f(\phi^a - \phi^b), \quad \frac{dN_0^a}{d\phi^a} = \text{const}, \quad \frac{dN_0^b}{d\phi^b} = \text{const} \quad (A2)$$

To study the pair distribution as a function of $\Delta\phi$, we define the difference and average of ϕ^a and ϕ^b as new orthogonal variables:

$$\Delta\phi \equiv \phi^a - \phi^b, \quad \bar{\Phi} \equiv (\phi^a + \phi^b)/2 \quad (A3)$$

We integrate the true pairs over $\bar{\Phi}$ to obtain the projection onto $\Delta\phi$. This is equivalent to binning the data in $\Delta\phi$.

$$\begin{aligned} \frac{dN_0^{ab}}{d(\Delta\phi)} &= \int \frac{d^2 N_0^{ab}}{d\phi^a d\phi^b} d\bar{\Phi} = \int f(\Delta\phi) d\bar{\Phi} \\ &= f(\Delta\phi) \int d\bar{\Phi} \propto f(\Delta\phi) \end{aligned} \quad (A4)$$

The measured distributions (without superscript) are related to the true distributions through the experimental acceptance/efficiency (here just “acceptance” for short):

$$\begin{aligned} \frac{d^2 N^{ab}}{d\phi^a d\phi^b} &= \varepsilon^{ab}(\phi^a, \phi^b) \frac{d^2 N_0^{ab}}{d\phi^a d\phi^b}, \\ \frac{dN^a}{d\phi^a} &= \varepsilon^a(\phi^a) \frac{dN_0^a}{d\phi^a}, \quad \frac{dN^b}{d\phi^b} = \varepsilon^b(\phi^b) \frac{dN_0^b}{d\phi^b} \end{aligned} \quad (A5)$$

where ε^{ab} , ε^a and ε^b describe the experimental acceptances for pairs and singles. The pair acceptance is, to a very good approximation, equal to the product of the singles acceptances:

$$\varepsilon^{ab}(\phi^a, \phi^b) = \varepsilon^a(\phi^a) \varepsilon^b(\phi^b) \quad (A6)$$

i.e. the experimental acceptance for A particles is not influenced by the presence or absence of B particles in any particular event, and vice versa [81].

The numerator of the correlation function is the measured pair distribution projected onto $\Delta\phi$

$$\begin{aligned} N^{\text{same}}(\Delta\phi) &= \int \frac{d^2 N_0^{ab}}{d\phi^a d\phi^b} d\bar{\Phi} \\ &= f(\Delta\phi) \int \varepsilon^{ab}(\phi^a, \phi^b) d\bar{\Phi} \end{aligned} \quad (\text{A7})$$

Mixed-event pairs are constructed by combining a particle at ϕ^a from one event with particles at ϕ^b from other, unrelated events. The mixed-event pairs over (ϕ^a, ϕ^b) factorize and have the form

$$\frac{d^2 N_{\text{mixed}}^{ab}}{d\phi^a d\phi^b} \propto \frac{dN^a}{d\phi^a} \frac{dN^b}{d\phi^b} \quad (\text{A8})$$

The denominator of the correlation function is the projection of the measured mixed-event pairs:

$$\begin{aligned} N^{\text{mixed}}(\Delta\phi) &= \int \frac{d^2 N_{\text{mixed}}^{ab}}{d\phi^a d\phi^b} d\bar{\Phi} \\ &\propto \int \frac{dN^a}{d\phi^a} \frac{dN^b}{d\phi^b} d\bar{\Phi} \\ &\propto \int \varepsilon^a(\phi^a) \varepsilon^b(\phi^b) d\bar{\Phi} \end{aligned} \quad (\text{A9})$$

Writing the correlation function with Equations A7 and A9, and applying Eq. A6 and Eq. A4 yields

$$\begin{aligned} C(\Delta\phi) &\equiv \frac{N^{\text{same}}(\Delta\phi)}{N^{\text{mixed}}(\Delta\phi)} \\ &\propto \frac{f(\Delta\phi) \int \varepsilon^{ab}(\phi^a, \phi^b) d\bar{\Phi}}{\int \varepsilon^a(\phi^a) \varepsilon^b(\phi^b) d\bar{\Phi}} \end{aligned} \quad (\text{A10})$$

$$\propto f(\Delta\phi) \propto \frac{dN_0^{ab}}{d(\Delta\phi)} \quad (\text{A11})$$

This shows that the shape of the true-pair distribution is recovered in the correlation function.

APPENDIX B: THE ROLE OF REACTION PLANE

No mention, explicit or implicit, was made of the reaction plane in the preceding proof; this is not surprising, since its validity holds for *any* source of correlation, whether from flow, jets, or other. We show that Eq. A11 holds for limited detector acceptance with the reaction plane included explicitly.

For events with reaction plane direction Ψ we define the conditional probabilities of finding an a or a b particle, including the effects of acceptance:

$$\begin{aligned} P^a(\phi^a|\Psi) &= \varepsilon^a(\phi^a) \frac{dN^a}{d(\phi^a - \Psi)}, \\ P^b(\phi^b|\Psi) &= \varepsilon^b(\phi^b) \frac{dN^b}{d(\phi^b - \Psi)} \end{aligned} \quad (\text{B1})$$

We can write the acceptances, and the *true* singles distributions with respect to Ψ , into their Fourier expansions:

$$\varepsilon^a(\phi) = \sum_{p=-\infty}^{p=+\infty} a_p e^{ip\phi} \quad \varepsilon^b(\phi) = \sum_{q=-\infty}^{q=+\infty} b_q e^{iq\phi} \quad (\text{B2})$$

where $a_{-p} = a_p^*$, $b_{-q} = b_q^*$ and

$$\begin{aligned} \frac{dN^a}{d(\phi^a - \Psi)} &= \frac{1}{2\pi} \sum_{n=-\infty}^{n=+\infty} \nu_n^a e^{in(\phi^a - \Psi)} \\ &= \frac{1}{2\pi} \left(1 + \sum_{n=1}^{+\infty} 2\nu_n^a \cos n(\phi^a - \Psi) \right) \\ \frac{dN^b}{d(\phi^b - \Psi)} &= \frac{1}{2\pi} \sum_{m=-\infty}^{m=+\infty} \nu_m^b e^{im(\phi^b - \Psi)} \\ &= \frac{1}{2\pi} \left(1 + \sum_{m=1}^{+\infty} 2\nu_m^b \cos m(\phi^b - \Psi) \right) \end{aligned} \quad (\text{B3})$$

In the case that ab correlations are due to particle correlation with respect to the same reaction plane, as would be true of background pairs, then the *measured* same-event pair distribution can be written as

$$\begin{aligned} N^{\text{same}}(\Delta\phi) &= \int \frac{d\phi^a}{2\pi} \frac{d\Psi}{2\pi} P^a(\phi^a|\Psi) P^b((\phi^a - \Delta\phi)|\Psi) \\ &= \sum_{p=-\infty}^{p=+\infty} \sum_{n=-\infty}^{n=+\infty} a_p b_p^* \nu_n^a \nu_n^b e^{i(p+n)\Delta\phi} \end{aligned} \quad (\text{B4})$$

Similarly, the *measured* mixed-event pair distribution is

$$\begin{aligned} N^{\text{mixed}}(\Delta\phi) &= \int \frac{d\phi^a d\Psi^a d\Psi^b}{8\pi^3} P^a(\phi^a|\Psi^a) P^b((\phi^a - \Delta\phi)|\Psi^b) \\ &= \sum_{p=-\infty}^{p=+\infty} a_p b_p^* e^{ip\Delta\phi} \end{aligned} \quad (\text{B5})$$

Using these to construct the correlation function, we find

$$C(\Delta\phi) \equiv \frac{N^{\text{same}}(\Delta\phi)}{N^{\text{mixed}}(\Delta\phi)} = \sum_{n=-\infty}^{n=+\infty} \nu_n^a \nu_n^b e^{in\Delta\phi} \quad (\text{B6})$$

It is clear that the dependence upon the reaction plane angle is integrated out when forming the correlation function. It is also clear that the quadruple modulation strength of the correlation function $\nu_2^a \nu_2^b$ for background pairs is exactly the product of the *true* modulation strengths of the *true* singles distributions ν_2^a and ν_2^b .

APPENDIX C: SIMULATION STUDY OF THE NON-FLOW EFFECT FROM JETS

The elliptic flow of the triggers and partners, which are used to estimate the background contribution in the correlation function Eq. 15, are provided by the BBC reaction plane method. In this section, we show that the large rapidity separation of $|\Delta\eta| > 2.75$ between PHENIX BBC and central arm greatly suppresses the bias due to jet and dijets to the reaction plane determination. More details can be also be found in [82].

The intra-jet correlation is typically limited by the size of the jet cone, which is much smaller than the $\Delta\eta$ separation between BBC and central arm. However, due to their broad distribution of parton x values, the away-side jet has a very broad distribution in $\Delta\eta$. Hence the inter-jet correlations can potentially bias the BBC reaction plane determination. We study the biases by embedding back-to-back jet pairs into HIJING events. The HIJING events serve as the underlying Au+Au events, and were checked to reproduce the charged hadron multiplicity in η from PHOBOS [83]. Elliptic flow is implemented by applying a track by track weight in each HIJING event:

$$w(\mathbf{b}, p_T, \eta) = 1 + 2v_2(\mathbf{b}, p_T, \eta) \cos 2(\phi - \Psi)$$

where the Ψ is the direction of the impact parameter \mathbf{b} . The centrality and p_T dependence of the v_2 is tuned according to the PHENIX measurement [84]. The η dependence of v_2 is obtained from PHOBOS [59] minimum bias events. The v_2 shape versus η is assumed to be independent of centrality selections. This gives an overall \mathbf{b} , p_T and η dependence by a single function,

$$v_2(p_T, \mathbf{b}, \eta) = 0.02834 \mathbf{b} e^{-0.5(\eta/3.92)^2} \left(1 - \frac{2.1}{1 + e^{1.357p_T}} \right)$$

We then generate back-to-back jet pairs from the PYTHIA event generator, requiring a leading particle above 6 GeV/c at mid-rapidity ($|\eta| < 0.35$). Assuming the fractional momentum of the leading hadron is $\langle z \rangle \approx 0.7$ [44], this corresponds to typical jet energy of $6/\langle z \rangle \approx 9$ GeV/c.

We evaluate the dijet bias by comparing the event plane before and after the embedding. Dijets tend to bias the event plane towards the dijet direction, resulting in a false v_2 for the jet particles. Figure 34 shows the relative azimuth distribution between the jet leading hadrons and the event plane (EP) from the HIJING event (left panels) or the combined event (right panels). The dijets clearly become correlated with the EP determined from the combined event, leading to a false v_2 for the leading hadrons. However, since we embed one such dijet pair for every event, the bias shown in Fig. 34 should be interpreted as the bias for those events containing a high- p_T dijet. Thus it sets an upper limit for the bias effect.

In order to understand the impact of the false v_2 , we have to determine their magnitudes in the same way as

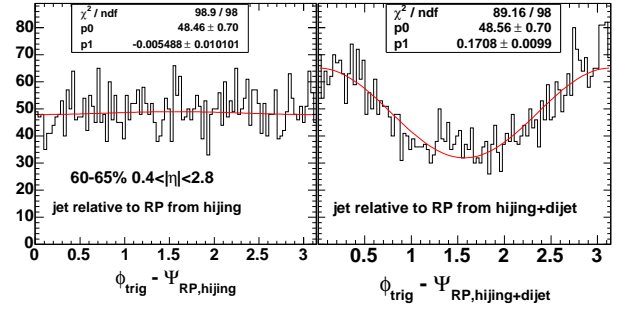


FIG. 34: The distribution of the leading particle from the dijets relative to the event plane calculated from HIJING only (left) and event plane from the embedded event (right).

the real data analysis, i.e. according to:

$$v_2 = \frac{v_{2,\text{raw}}}{c_{v_2}} = \frac{\langle \cos 2(\phi - \Phi_{\text{EP}}) \rangle}{\langle \cos 2(\Phi_{\text{EP}} - \Phi_{\text{RP}}) \rangle}$$

We obtain the raw v_2 for by fitting the embedded trigger distribution (such as Fig. 34) for each individual centrality bin. The raw v_2 is then divided by the corresponding reaction plane resolution, which can be calculated as $c_{v_2} = \langle \cos 2(\Phi_{\text{EP}} - \Phi_{\text{RP}}) \rangle$.

The magnitude of the false v_2 depends on the rapidity separation between the trigger and the sub-event used to determine the EP. Due to away-side jet swing, this bias could persist to large rapidity regions. Figure 35 shows the centrality dependence of false trigger v_2 for events containing high- p_T dijets for various rapidity windows used for EP determination. The false v_2 decreases as the sub-event used to determine the EP moves towards large η . When the sub-event is in the BBC acceptance ($3 < |\eta| < 4$), the false v_2 becomes negligible.

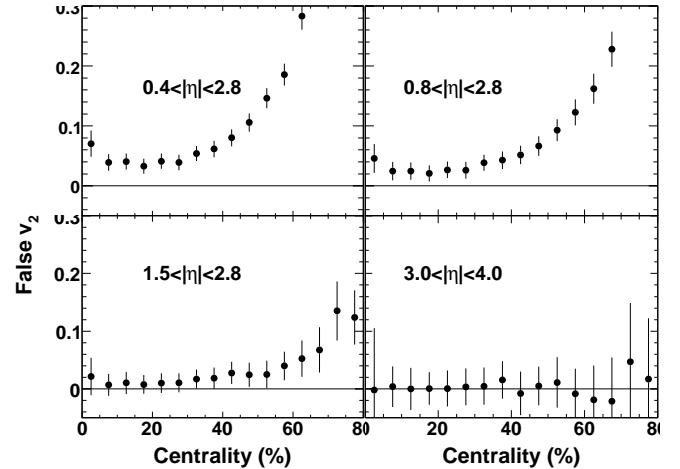


FIG. 35: The false reaction plane v_2 of the leading hadron from the embedded dijet as function of centrality. The η range used to determine the event plane is indicated in each panel. The embedded dijet is required to have a trigger hadron above 6 GeV/c with in mid-rapidity window of $|\eta| < 0.35$.

APPENDIX D: COMPREHENSIVE DATA PLOTS AND DATA TABLES

Figures 36-38 show the comprehensive array of results, covering the momentum range of 0.4 to 10 GeV/ c from which the representative subset shown in Fig. 6 were derived. These results are described in Sections III and IV.

Tables VII to XIX show numerical values of the plotted data. The corresponding figures are indicated in the table captions.

TABLE VII: D from FIT1 and FIT2 versus p_T^b for three p_T^a bins (Fig. 11).

$\langle p_T^b \rangle$ GeV/ c	D \pm Stat+Sys-Sys FIT1	D \pm Stat+Sys-Sys FIT2
$2 < p_T^a < 3$ GeV/ c		
0.6	0.88 \pm 0.01+0.12-0.12	1.09 \pm 0.01+0.03-0.05
1.2	0.94 \pm 0.01+0.09-0.10	1.14 \pm 0.01+0.04-0.04
1.7	1.00 \pm 0.01+0.08-0.09	1.17 \pm 0.01+0.03-0.03
2.2	1.04 \pm 0.01+0.07-0.08	1.17 \pm 0.01+0.03-0.03
2.7	1.10 \pm 0.02+0.06-0.07	1.19 \pm 0.02+0.03-0.03
3.3	1.11 \pm 0.05+0.05-0.05	1.13 \pm 0.05+0.03-0.03
4.4	1.11 \pm 0.17+0.15-0.12	1.29 \pm 0.09+0.02-0.03
$3 < p_T^a < 4$ GeV/ c		
0.6	0.90 \pm 0.01+0.11-0.11	1.12 \pm 0.04+0.03-0.03
1.2	1.01 \pm 0.01+0.08-0.09	1.19 \pm 0.02+0.01-0.03
1.7	1.04 \pm 0.02+0.07-0.08	1.15 \pm 0.03+0.03-0.03
2.2	1.10 \pm 0.04+0.05-0.05	1.12 \pm 0.06+0.03-0.03
2.7	1.16 \pm 0.12+0.04-0.05	1.21 \pm 0.07+0.02-0.03
3.3	1.13 \pm 0.13+0.10-0.05	1.30 \pm 0.06+0.01-0.01
$4 < p_T^a < 5$ GeV/ c		
0.6	0.89 \pm 0.05+0.08-0.10	1.07 \pm 0.13+0.03-0.03
1.2	0.85 \pm 0.06+0.08-0.07	0.85 \pm 0.09+0.08-0.05
1.7	1.13 \pm 0.13+0.08-0.10	1.20 \pm 0.13+0.03-0.04
2.2	1.09 \pm 0.16+0.08-0.08	1.21 \pm 0.16+0.03-0.04
2.7	1.11 \pm 0.20+0.11-0.10	1.19 \pm 0.17+0.03-0.04

TABLE VIII: Near-side jet width for $p+p$ and 0-20% Au+Au for various p_T^a and p_T^b bins (Fig. 16). The width is unchanged by interchanging p_T^a and p_T^b .

Au+Au 0-20%				p+p	
$2 < p_T^a < 3 \text{ GeV}/c$					
$\langle p_T^b \rangle \text{ GeV}/c$	Width	Stat	Sys	Width	Sys
0.6	0.415	0.002	+0.022-0.041	0.472	0.006
1.4	0.432	0.001	+0.024-0.028	0.364	0.003
2.3	0.410	0.002	+0.043-0.019	0.281	0.003
$3 < p_T^a < 4 \text{ GeV}/c$					
0.6	0.383	0.015	+0.006-0.033	0.430	0.012
1.4	0.409	0.004	+0.028-0.039	0.314	0.005
2.3	0.365	0.012	+0.022-0.016	0.244	0.005
3.3	0.286	0.010	+0.005-0.035	0.199	0.007
$4 < p_T^b < 5 \text{ GeV}/c$					
0.6	0.394	0.037	+0.036-0.027	0.402	0.018
1.4	0.340	0.017	+0.036-0.040	0.299	0.008
2.3	0.274	0.012	+0.011-0.022	0.225	0.007
3.3	0.223	0.010	+0.012-0.027	0.201	0.010
4.4	0.179	0.009	+0.002-0.013	0.148	0.011
$5 < p_T^a < 10 \text{ GeV}/c$					
0.6	0.308	0.059	+0.016-0.036	0.385	0.008
1.4	0.303	0.029	+0.031-0.040	0.281	0.003
2.3	0.224	0.015	+0.007-0.028	0.208	0.003
3.3	0.198	0.012	+0.008-0.023	0.165	0.003
4.4	0.155	0.009	+0.007-0.014	0.155	0.005
6.6	0.135	0.008	+0.001-0.001	0.130	0.004

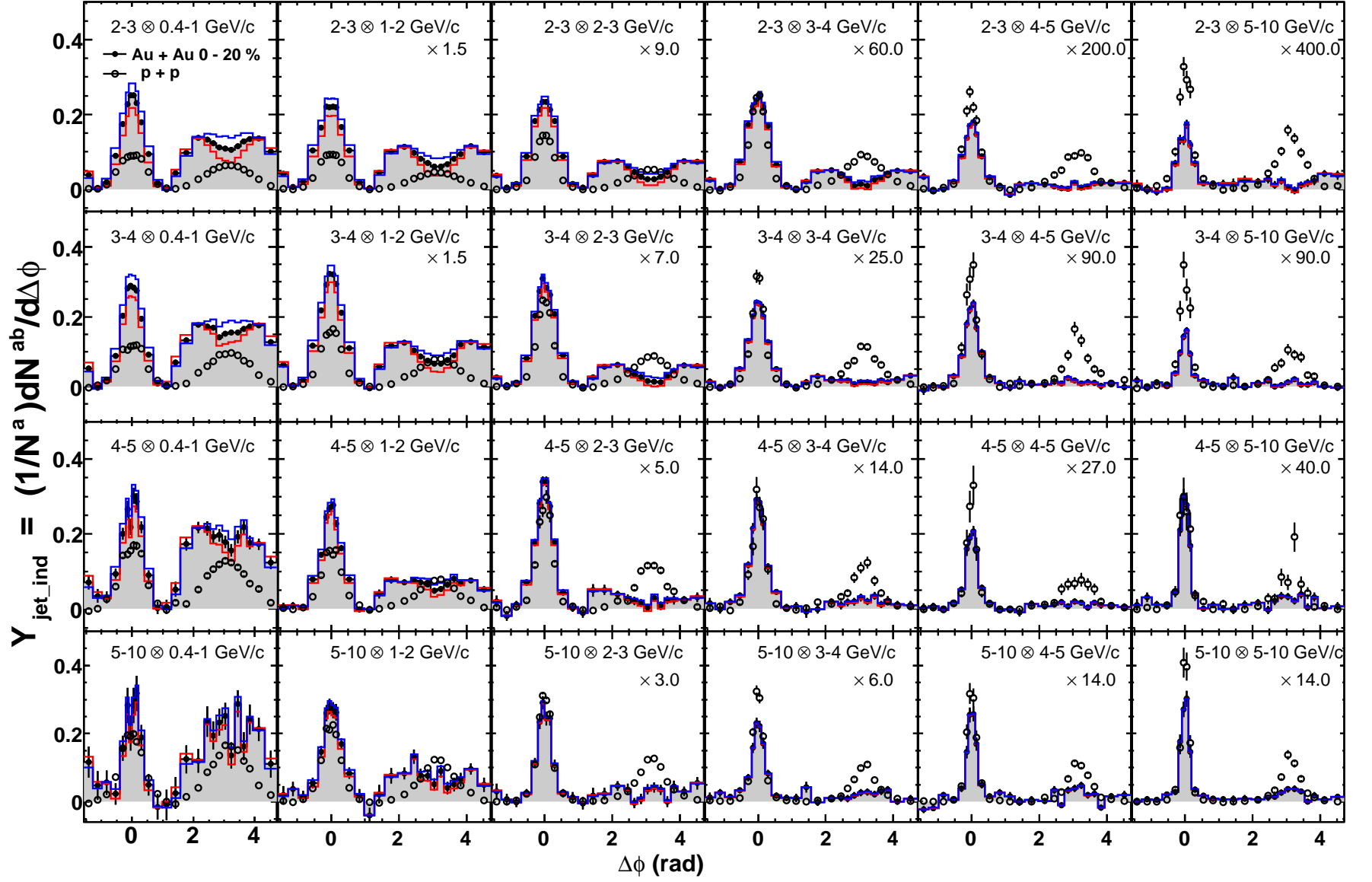


FIG. 36: (Color online) Per-trigger yield versus $\Delta\phi$ for successively increasing trigger and partner p_T ($p_T^a \otimes p_T^b$) in $p+p$ (open circles) and 0-20 % Au+Au (filled circles) collisions. Data are scaled to the vertical axes of the four left panels. Histograms indicate elliptic flow uncertainties for Au+Au collisions.

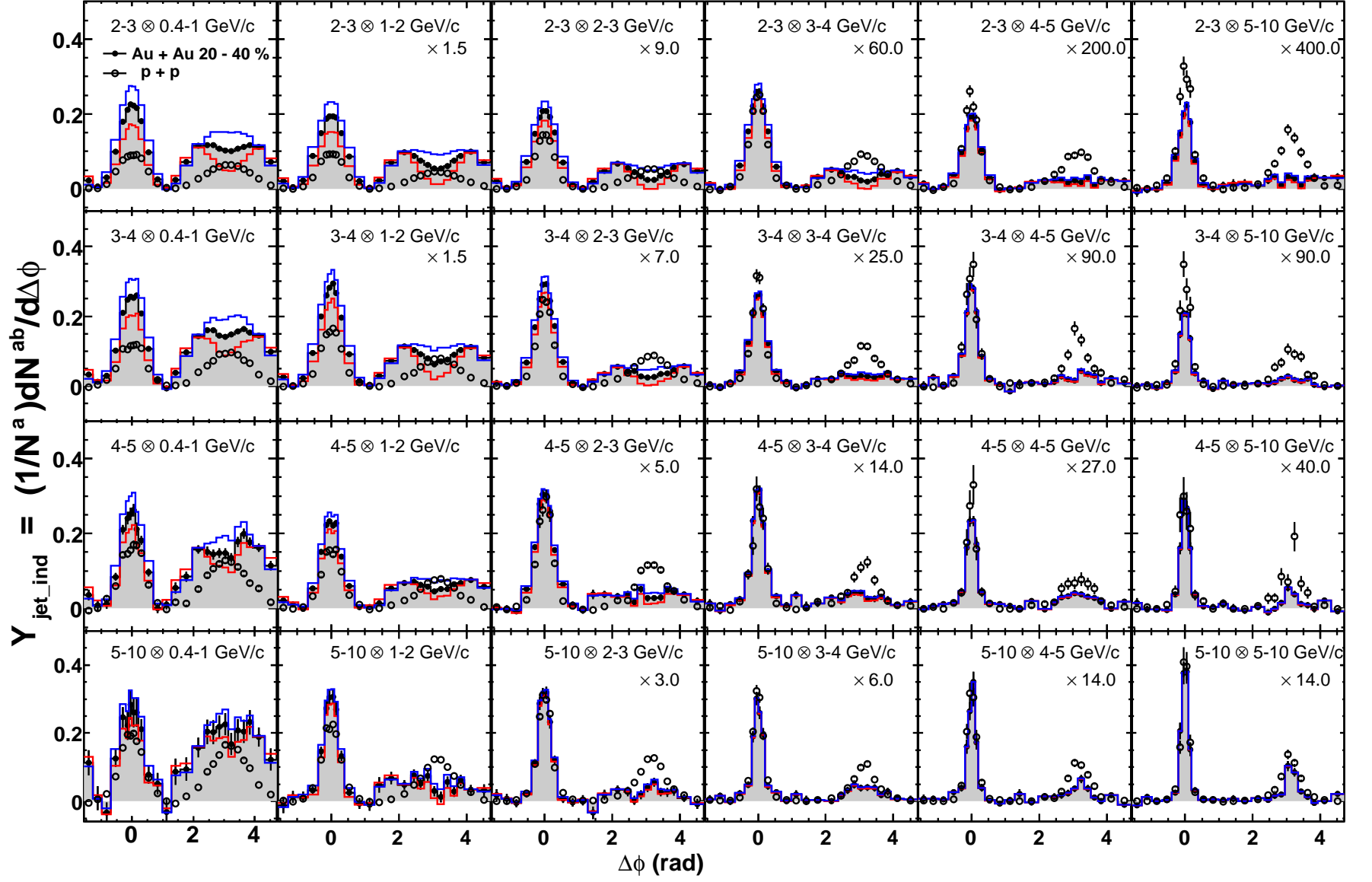


FIG. 37: (Color online) Per-trigger yield versus $\Delta\phi$ for successively increasing trigger and partner p_T ($p_T^a \otimes p_T^b$) in p + p (open circles) and 20-40 % Au+Au (filled circles) collisions. Data are scaled to the vertical axes of the three left panels. Histograms indicate elliptic flow uncertainties for Au+Au collisions.

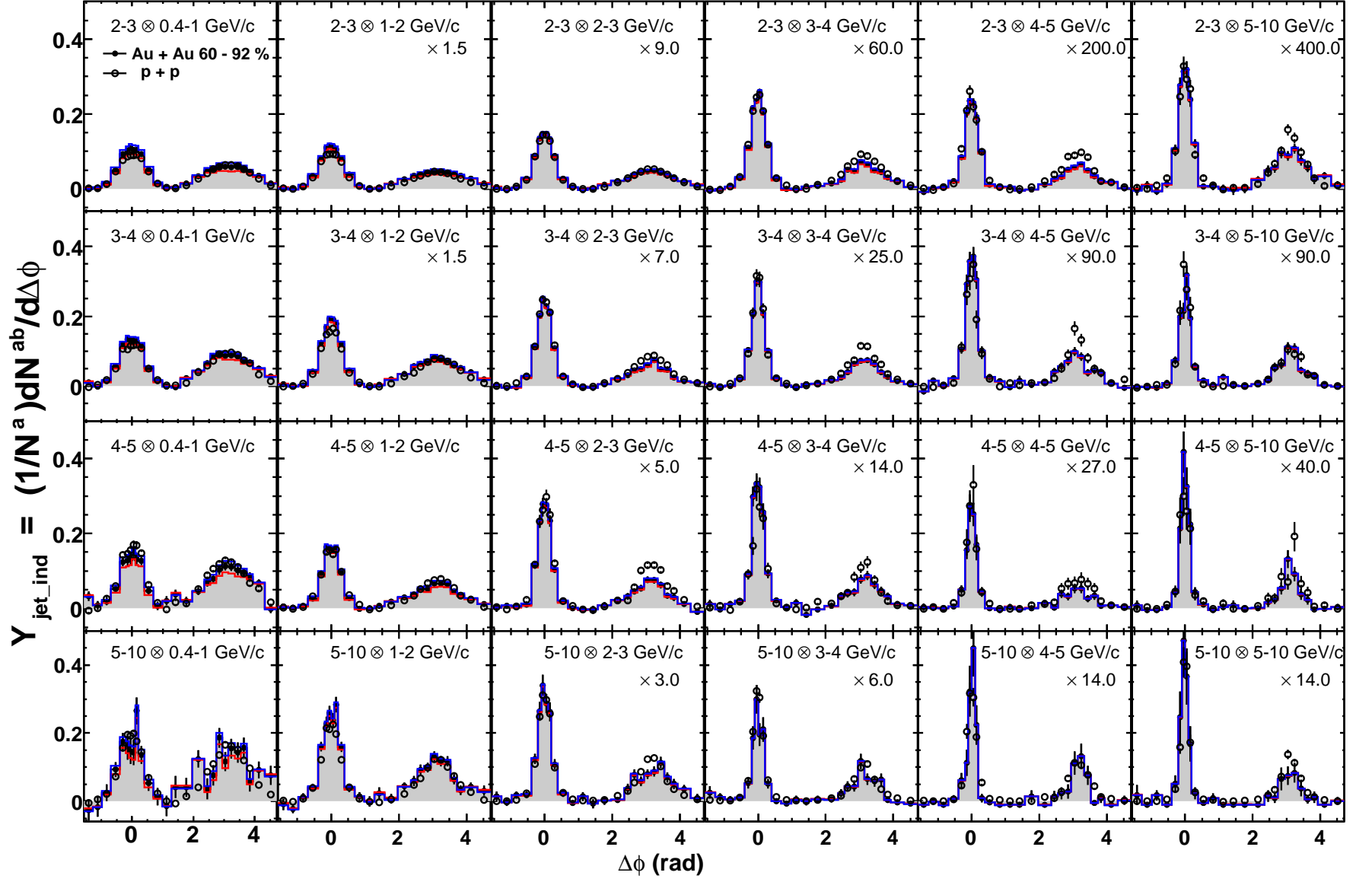


FIG. 38: (Color online) Per-trigger yield versus $\Delta\phi$ for successively increasing trigger and partner p_T ($p_T^a \otimes p_T^b$) in $p + p$ (open circles) and 60-92 % Au+Au (filled circles) collisions. Data are scaled to the vertical axes of the three left panels. Histograms indicate elliptic flow uncertainties for Au+Au collisions.

TABLE IX: Centrality dependence of near-side jet widths for various $p_T^a \otimes p_T^b$ bins (Fig. 17).

$\langle N_{\text{part}} \rangle$	Width	Stat.Err.	Sys. Err.
$2 - 3 \otimes 0.4 - 1 \text{ GeV}/c$			
351.4	0.367	0.012	+0.032-0.043
299.0	0.415	0.007	+0.033-0.044
234.6	0.424	0.002	+0.024-0.027
166.6	0.431	0.002	+0.048-0.041
114.2	0.438	0.002	+0.048-0.041
74.4	0.438	0.003	+0.057-0.043
45.5	0.436	0.004	+0.055-0.030
14.5	0.435	0.003	+0.059-0.022
2.0	0.472	0.006	+0.001-0.001
$2 - 3 \otimes 2 - 3 \text{ GeV}/c$			
351.4	0.415	0.005	+0.054-0.047
299.0	0.409	0.005	+0.035-0.017
234.6	0.410	0.003	+0.042-0.019
166.6	0.406	0.008	+0.006-0.028
114.2	0.360	0.008	+0.013-0.023
74.4	0.352	0.008	+0.014-0.033
45.5	0.307	0.005	+0.015-0.037
14.5	0.289	0.004	+0.006-0.009
2.0	0.281	0.003	+0.001-0.001
$3 - 4 \otimes 3 - 4 \text{ GeV}/c$			
351.4	0.318	0.019	+0.023-0.032
299.0	0.287	0.021	+0.021-0.037
234.6	0.271	0.010	+0.008-0.013
166.6	0.260	0.010	+0.012-0.012
114.2	0.225	0.008	+0.015-0.030
74.4	0.228	0.008	+0.009-0.011
45.5	0.201	0.008	+0.005-0.026
14.5	0.211	0.006	+0.004-0.014
2.0	0.199	0.007	+0.001-0.001
$4 - 5 \otimes 4 - 5 \text{ GeV}/c$			
351.4	0.202	0.020	+0.017-0.000
299.0	0.191	0.018	+0.009-0.019
234.6	0.168	0.013	+0.021-0.029
166.6	0.167	0.010	+0.008-0.019
114.2	0.142	0.008	+0.004-0.001
74.4	0.143	0.009	+0.005-0.010
45.5	0.143	0.011	+0.005-0.016
14.5	0.161	0.010	+0.001-0.003
2.0	0.148	0.011	+0.002-0.002
$5 - 10 \otimes 5 - 10 \text{ GeV}/c$			
351.4	0.162	0.017	+0.014-0.034
299.0	0.135	0.017	+0.001-0.023
234.6	0.133	0.011	+0.008-0.031
166.6	0.136	0.009	+0.007-0.009
114.2	0.131	0.008	+0.002-0.005
74.4	0.113	0.015	+0.002-0.008
45.5	0.146	0.016	+0.001-0.004
14.5	0.137	0.015	+0.002-0.007
2.0	0.130	0.004	+0.002-0.002

TABLE X: R_{HS} in $p + p$ and 0-20% Au+Au for various p_{T}^{a} and p_{T}^{b} bins (Fig. 7).

$\langle p_{\text{T}}^{\text{b}} \rangle$ GeV/ c	Au + Au 0-20%				$p + p$	
	R_{HS}	Stat.	v_2 Err.	ZYAM Err.	R_{HS}	Total Err.
$2.0 < p_{\text{T}}^{\text{a}} < 3.0$ GeV/ c						
0.66	0.965	0.008	+0.211-0.236	+0.007-0.000	2.428	+0.007-0.000
1.22	0.722	0.008	+0.180-0.201	+0.038-0.002	2.419	+0.038-0.002
1.72	0.628	0.010	+0.176-0.196	+0.040-0.005	2.752	+0.040-0.005
2.23	0.531	0.016	+0.178-0.198	+0.051-0.009	2.673	+0.051-0.009
2.73	0.395	0.027	+0.198-0.208	+0.113-0.021	3.234	+0.113-0.021
3.43	0.402	0.044	+0.192-0.198	+0.083-0.035	3.325	+0.083-0.035
4.43	0.581	0.190	+0.278-0.285	+0.076-0.119	4.590	+0.076-0.119
6.42	0.638	0.213	+0.114-0.111	+0.070-0.114	5.438	+0.070-0.114
$3.0 < p_{\text{T}}^{\text{a}} < 4.0$ GeV/ c						
0.66	1.003	0.021	+0.174-0.183	+0.000-0.001	2.553	+0.000-0.001
1.22	0.711	0.023	+0.169-0.180	+0.048-0.007	2.730	+0.048-0.007
1.72	0.550	0.028	+0.166-0.185	+0.044-0.016	3.199	+0.044-0.016
2.23	0.384	0.046	+0.190-0.213	+0.093-0.039	3.418	+0.093-0.039
2.73	0.467	0.088	+0.208-0.200	+0.109-0.065	3.525	+0.109-0.065
3.43	0.531	0.122	+0.166-0.185	+0.059-0.079	4.184	+0.059-0.079
4.43	2.145	1.271	+0.165-0.216	+2.705-0.472	5.528	+2.705-0.472
6.42	2.488	1.216	+0.042-0.048	+2.378-0.567	7.077	+2.378-0.567
$4.0 < p_{\text{T}}^{\text{a}} < 5.0$ GeV/ c						
0.66	1.069	0.057	+0.157-0.164	+0.004-0.006	2.495	+0.004-0.006
1.22	0.971	0.087	+0.181-0.202	+0.003-0.003	3.464	+0.003-0.003
1.72	0.822	0.112	+0.184-0.185	+0.019-0.024	3.109	+0.019-0.024
2.23	0.520	0.179	+0.223-0.207	+0.093-0.132	3.835	+0.093-0.132
2.73	0.443	0.286	+0.225-0.254	+0.146-0.306	6.726	+0.146-0.306
3.43	2.145	1.271	+0.165-0.216	+2.705-0.472	5.528	+2.705-0.472
4.43	1.344	0.565	+0.056-0.060	+0.265-0.104	5.579	+0.265-0.104
6.42	2.489	0.972	+0.008-0.009	+2.250-0.358	9.191	+2.250-0.358
$5.0 < p_{\text{T}}^{\text{a}} < 10.0$ GeV/ c						
0.66	1.339	0.165	+0.169-0.173	+0.050-0.039	3.073	+0.050-0.039
1.22	0.917	0.162	+0.140-0.144	+0.018-0.016	3.884	+0.018-0.016
1.72	0.645	0.219	+0.167-0.198	+0.071-0.117	4.915	+0.071-0.117
2.23	0.649	0.289	+0.141-0.165	+0.086-0.169	5.372	+0.086-0.169
2.73	0.620	0.283	+0.079-0.087	+0.092-0.178	5.525	+0.092-0.178
3.43	2.488	1.216	+0.042-0.048	+2.378-0.567	7.077	+2.378-0.567
4.43	2.489	0.972	+0.008-0.009	+2.250-0.358	9.191	+2.250-0.358
6.42	2.761	1.015	+0.004-0.004	+2.879-0.437	11.159	+2.879-0.437

TABLE XI: Centrality dependence of D from FIT1 and FIT2 (Fig. 10).

$\langle N_{\text{part}} \rangle$	D from FIT1			D from FIT2			Fraction of shoulder yield(FIT2)		
	D	Stat. Err	Sys.Err	D	Stat. Err	Sys.Err	Frac	Stat.Err	Sys.Err
351.4	1.068	0.016	+0.032-0.032	1.192	0.024	+0.028-0.028	0.800	0.053	+0.027-0.028
299.0	1.090	0.013	+0.055-0.062	1.208	0.017	+0.028-0.030	0.800	0.044	+0.053-0.059
234.6	1.030	0.010	+0.100-0.120	1.126	0.022	+0.045-0.054	0.842	0.052	+0.108-0.128
166.6	0.976	0.016	+0.110-0.153	0.983	0.035	+0.103-0.036	0.981	0.111	+0.019-0.291
114.2	0.865	0.018	+0.141-0.123	0.930	0.064	+0.091-0.050	0.851	0.246	+0.149-0.253
74.4	0.786	0.030	+0.129-0.116	0.916	0.045	+0.085-0.085	0.750	0.043	+0.250-0.195
45.5	0.652	0.021	+0.074-0.066	0.996	0.029	+0.030-0.030	0.293	0.040	+0.091-0.064
14.5	0.000	0.989	+0.010-0.000	1.178	0.047	+0.050-0.047	0.120	0.029	+0.049-0.032

TABLE XII: Truncated mean p_T , $\langle p'_T \rangle$, for various $\Delta\phi$ ranges and centrality (Fig. 25).

$2.0 < p_T^a < 3.0 \text{ GeV}/c$									
Near-side(GeV/c)				Away-side Shoulder(GeV/c)			Away-side Head(GeV/c)		
$\langle N_{\text{part}} \rangle$	$\langle p'_T \rangle$	Stat	Sys	$\langle p'_T \rangle$	Stat	Sys	$\langle p'_T \rangle$	Stat	Sys
351.4	0.554	0.008	+0.009-0.019	0.445	0.011	+0.001-0.010	0.388	0.017	+0.006-0.017
299.0	0.538	0.007	+0.015-0.022	0.453	0.009	+0.001-0.011	0.379	0.014	+0.014-0.026
234.6	0.530	0.004	+0.025-0.012	0.439	0.006	+0.020-0.004	0.388	0.008	+0.042-0.032
166.6	0.531	0.004	+0.028-0.015	0.449	0.007	+0.018-0.005	0.407	0.008	+0.033-0.042
114.2	0.529	0.005	+0.028-0.020	0.441	0.008	+0.002-0.007	0.426	0.009	+0.005-0.020
74.4	0.549	0.006	+0.028-0.024	0.457	0.012	+0.005-0.011	0.491	0.012	+0.039-0.021
45.5	0.589	0.007	+0.021-0.025	0.503	0.017	+0.000-0.013	0.540	0.013	+0.032-0.027
25.7	0.587	0.009	+0.020-0.019	0.487	0.022	+0.000-0.014	0.557	0.013	+0.030-0.023
9.5	0.600	0.009	+0.011-0.022	0.491	0.025	+0.003-0.023	0.580	0.013	+0.016-0.023
2.0	0.609	0.005	+0.000-0.012	0.543	0.014	+0.000-0.023	0.603	0.008	+0.000-0.012
$3.0 < p_T^a < 4.0 \text{ GeV}/c$									
Near-side(GeV/c)				Away-side Shoulder(GeV/c)			Away-side Head(GeV/c)		
$\langle N_{\text{part}} \rangle$	$\langle p'_T \rangle$	Stat	Sys	$\langle p'_T \rangle$	Stat	Sys	$\langle p'_T \rangle$	Stat	Sys
351.4	0.630	0.020	+0.007-0.007	0.446	0.031	+0.018-0.022	0.349	0.054	+0.044-0.060
299.0	0.598	0.017	+0.021-0.017	0.446	0.026	+0.007-0.018	0.388	0.040	+0.021-0.039
234.6	0.590	0.011	+0.038-0.019	0.420	0.018	+0.028-0.013	0.361	0.027	+0.057-0.035
166.6	0.599	0.011	+0.034-0.022	0.439	0.019	+0.009-0.014	0.416	0.022	+0.019-0.040
114.2	0.623	0.011	+0.036-0.031	0.475	0.022	+0.006-0.014	0.495	0.023	+0.030-0.017
74.4	0.646	0.014	+0.034-0.025	0.457	0.029	+0.014-0.021	0.530	0.025	+0.036-0.021
45.5	0.640	0.015	+0.019-0.016	0.435	0.033	+0.011-0.027	0.539	0.024	+0.018-0.017
25.7	0.674	0.018	+0.016-0.016	0.446	0.042	+0.013-0.033	0.582	0.024	+0.015-0.014
9.5	0.725	0.019	+0.010-0.044	0.542	0.054	+0.002-0.045	0.646	0.024	+0.011-0.033
2.0	0.715	0.012	+0.000-0.002	0.595	0.030	+0.002-0.007	0.689	0.016	+0.000-0.001
$4.0 < p_T^a < 5.0 \text{ GeV}/c$									
Near-side(GeV/c)				Away-side Shoulder(GeV/c)			Away-side Head(GeV/c)		
$\langle N_{\text{part}} \rangle$	$\langle p'_T \rangle$	Stat	Sys	$\langle p'_T \rangle$	Stat	Sys	$\langle p'_T \rangle$	Stat	Sys
351.4	0.758	0.060	+0.018-0.013	0.533	0.140	+0.045-0.088	0.495	0.156	+0.064-0.146
299.0	0.649	0.039	+0.020-0.017	0.447	0.070	+0.039-0.055	0.381	0.081	+0.058-0.088
234.6	0.698	0.028	+0.022-0.043	0.433	0.058	+0.008-0.047	0.438	0.062	+0.006-0.054
166.6	0.703	0.026	+0.024-0.055	0.449	0.046	+0.002-0.034	0.513	0.055	+0.011-0.034
114.2	0.702	0.026	+0.039-0.029	0.501	0.058	+0.027-0.036	0.609	0.048	+0.064-0.036
74.4	0.717	0.026	+0.036-0.028	0.468	0.055	+0.033-0.040	0.603	0.043	+0.047-0.032
45.5	0.718	0.028	+0.018-0.015	0.485	0.073	+0.039-0.055	0.597	0.042	+0.022-0.021
25.7	0.795	0.034	+0.014-0.022	0.556	0.091	+0.017-0.047	0.693	0.049	+0.016-0.018
9.5	0.827	0.036	+0.017-0.014	0.627	0.109	+0.042-0.049	0.700	0.043	+0.017-0.013
2.0	0.778	0.022	+0.001-0.001	0.672	0.057	+0.005-0.006	0.777	0.030	+0.001-0.001
$5.0 < p_T^a < 10.0 \text{ GeV}/c$									
Near-side(GeV/c)				Away-side Shoulder(GeV/c)			Away-side Head(GeV/c)		
$\langle N_{\text{part}} \rangle$	$\langle p'_T \rangle$	Stat	Sys.	$\langle p'_T \rangle$	Stat	Sys	$\langle p'_T \rangle$	Stat	Sys
351.4	0.976	0.110	+0.136-0.074	0.640	0.195	+0.018-0.051	0.577	0.162	+0.035-0.085
299.0	0.876	0.092	+0.071-0.042	0.528	0.161	+0.052-0.116	0.536	0.285	+0.081-0.410
234.6	0.754	0.056	+0.040-0.033	0.481	0.109	+0.043-0.083	0.619	0.131	+0.073-0.058
166.6	0.826	0.057	+0.023-0.016	0.356	0.136	+0.102-0.194	0.695	0.167	+0.045-0.028
114.2	0.758	0.045	+0.041-0.031	0.481	0.103	+0.047-0.076	0.722	0.077	+0.069-0.045
74.4	0.839	0.056	+0.031-0.103	0.516	0.161	+0.006-0.131	0.663	0.080	+0.021-0.064
45.5	0.889	0.054	+0.034-0.026	0.654	0.179	+0.014-0.033	0.768	0.072	+0.022-0.017
25.7	0.791	0.059	+0.012-0.013	0.649	0.177	+0.025-0.071	0.749	0.077	+0.015-0.012
9.5	0.871	0.071	+0.021-0.023	0.419	0.142	+0.073-0.135	0.853	0.088	+0.017-0.018
2.0	0.925	0.013	+0.001-0.001	0.720	0.028	+0.004-0.005	0.883	0.015	+0.001-0.001

TABLE XIII: Truncated mean p_T , $\langle p'_T \rangle$, in HR for various $p_T^a \otimes p_T^b$ bins (Fig. 26).

$1.0 < p_T^b < 7.0 \text{ GeV}/c$						
$3.0 < p_T^a < 4.0 \text{ GeV}/c$				$4.0 < p_T^a < 5.0 \text{ GeV}/c$		
$\langle N_{\text{part}} \rangle$	$\langle p'_T \rangle$	Stat	Sys	$\langle p'_T \rangle$	Stat	Sys
279.9	0.383	0.020	+0.017-0.039	0.448	0.049	+0.034-0.046
140.4	0.469	0.017	+0.010-0.014	0.602	0.042	+0.047-0.044
60.0	0.560	0.018	+0.037-0.020	0.637	0.032	+0.039-0.030
14.5	0.643	0.018	+0.014-0.024	0.794	0.041	+0.030-0.024
2.0	0.732	0.017	+0.000-0.002	0.838	0.032	+0.002-0.002
$1.5 < p_T^b < 7.0 \text{ GeV}/c$						
$3.0 < p_T^a < 4.0 \text{ GeV}/c$				$4.0 < p_T^a < 5.0 \text{ GeV}/c$		
$\langle N_{\text{part}} \rangle$	$\langle p'_T \rangle$	Stat	Sys	$\langle p'_T \rangle$	Stat	Sys
279.9	0.398	0.049	+0.032-0.042	0.559	0.111	+0.044-0.062
140.4	0.525	0.035	+0.071-0.059	0.697	0.073	+0.084-0.059
60.0	0.643	0.033	+0.057-0.040	0.725	0.054	+0.040-0.029
14.5	0.753	0.032	+0.024-0.021	0.917	0.065	+0.031-0.029
2.0	0.827	0.029	+0.002-0.002	0.903	0.053	+0.003-0.003
$2.0 < p_T^b < 7.0 \text{ GeV}/c$						
$3.0 < p_T^a < 4.0 \text{ GeV}/c$				$4.0 < p_T^a < 5.0 \text{ GeV}/c$		
$\langle N_{\text{part}} \rangle$	$\langle p'_T \rangle$	Stat	Sys	$\langle p'_T \rangle$	Stat	Sys
279.9	0.570	0.135	+0.128-0.072	1.026	0.284	+0.240-0.150
140.4	0.722	0.075	+0.285-0.085	0.918	0.127	+0.171-0.093
60.0	0.747	0.054	+0.052-0.043	0.843	0.086	+0.042-0.033
14.5	0.865	0.051	+0.025-0.020	0.989	0.093	+0.024-0.026
2.0	0.869	0.045	+0.004-0.003	0.924	0.079	+0.004-0.004
$2.5.0 < p_T^b < 7.0 \text{ GeV}/c$						
$3.0 < p_T^a < 4.0 \text{ GeV}/c$				$4.0 < p_T^a < 5.0 \text{ GeV}/c$		
$\langle N_{\text{part}} \rangle$	$\langle p'_T \rangle$	Stat	Sys	$\langle p'_T \rangle$	Stat	Sys
279.9	0.675	0.231	+0.078-0.085	1.188	0.354	+0.259-0.140
140.4	0.822	0.107	+0.231-0.095	1.021	0.162	+0.109-0.073
60.0	0.785	0.074	+0.044-0.030	0.884	0.114	+0.027-0.023
14.5	0.939	0.071	+0.018-0.014	1.037	0.124	+0.023-0.019
2.0	0.936	0.066	+0.006-0.005	0.972	0.116	+0.006-0.006
$3.0 < p_T^b < 7.0 \text{ GeV}/c$						
$3.0 < p_T^a < 4.0 \text{ GeV}/c$				$4.0 < p_T^a < 5.0 \text{ GeV}/c$		
$\langle N_{\text{part}} \rangle$	$\langle p'_T \rangle$	Stat	Sys	$\langle p'_T \rangle$	Stat	Sys
279.9	0.750	0.305	+0.082-0.095	0.963	0.260	+0.047-0.037
140.4	0.857	0.121	+0.107-0.062	0.902	0.147	+0.039-0.032
60.0	0.836	0.092	+0.032-0.023	1.085	0.158	+0.035-0.029
14.5	0.932	0.085	+0.008-0.008	1.033	0.150	+0.009-0.008
2.0	0.906	0.083	+0.004-0.003	0.993	0.153	+0.004-0.004

TABLE XIV: Per-trigger yield in NR, HR and SR and various p_T^b ranges for $2.0 < p_T^a < 3.0$ GeV/c. They are bases for Fig. 12-14 and Fig. 18-20. The systematic uncertainties due to the single particle efficiency are not included ($\sim 10\%$).

$2.0 < p_T^a < 3.0$ GeV/c				
p_T^b (GeV/c)	$\int_{ \Delta\phi < \pi/3, \text{NR}} d\Delta\phi \left(\frac{1}{N^a} \frac{dN^{ab}}{d\Delta\phi} \right)$ Yield \pm Stat. + Sys. - Sys.	$\int_{ \Delta\phi - \pi < \pi/6, \text{HR}} d\Delta\phi \left(\frac{1}{N^a} \frac{dN^{ab}}{d\Delta\phi} \right)$ Yield \pm Stat. + Sys. - Sys.	$\int_{\pi/6 < \Delta\phi - \pi < \pi/3, \text{SR}} d\Delta\phi \left(\frac{1}{N^a} \frac{dN^{ab}}{d\Delta\phi} \right)$ Yield \pm Stat. + Sys. - Sys.	
0-20%	0.4-1.0	$(2.24 \pm 0.01 + 0.80 - 0.42) \times 10^{-1}$	$(1.20 \pm 0.01 + 0.45 - 0.31) \times 10^{-1}$	$(2.48 \pm 0.01 + 0.68 - 0.05) \times 10^{-1}$
	1.0-1.5	$(9.14 \pm 0.05 + 2.03 - 1.43) \times 10^{-2}$	$(3.47 \pm 0.03 + 1.23 - 1.02) \times 10^{-2}$	$(9.60 \pm 0.06 + 1.54 - 0.24) \times 10^{-2}$
	1.5-2.0	$(4.48 \pm 0.02 + 0.68 - 0.54) \times 10^{-2}$	$(1.18 \pm 0.02 + 0.43 - 0.39) \times 10^{-2}$	$(3.76 \pm 0.03 + 0.46 - 0.10) \times 10^{-2}$
	2.0-2.5	$(1.79 \pm 0.01 + 0.22 - 0.18) \times 10^{-2}$	$(3.25 \pm 0.08 + 1.40 - 1.27) \times 10^{-3}$	$(1.23 \pm 0.02 + 0.15 - 0.04) \times 10^{-2}$
	2.5-3.0	$(6.26 \pm 0.07 + 0.98 - 0.52) \times 10^{-3}$	$(7.07 \pm 0.44 + 5.60 - 3.80) \times 10^{-4}$	$(3.57 \pm 0.09 + 0.83 - 0.13) \times 10^{-3}$
	3.0-4.0	$(3.38 \pm 0.05 + 0.34 - 0.22) \times 10^{-3}$	$(3.14 \pm 0.31 + 2.04 - 1.61) \times 10^{-4}$	$(1.56 \pm 0.07 + 0.25 - 0.09) \times 10^{-3}$
	4.0-5.0	$(5.65 \pm 0.19 + 0.47 - 0.44) \times 10^{-4}$	$(4.41 \pm 1.24 + 2.86 - 2.72) \times 10^{-5}$	$(1.52 \pm 0.26 + 0.34 - 0.34) \times 10^{-4}$
	5.0-7.0	$(1.78 \pm 0.12 + 0.26 - 0.23) \times 10^{-4}$	$(8.83 \pm 8.19 + 14.41 - 12.59) \times 10^{-6}$	$(9.16 \pm 1.67 + 2.28 - 2.22) \times 10^{-5}$
	7.0-10.0	$(1.24 \pm 0.28 + 0.67 - 0.49) \times 10^{-5}$	—	—
20-40%	0.4-1.0	$(2.27 \pm 0.01 + 0.72 - 0.67) \times 10^{-1}$	$(1.12 \pm 0.01 + 0.49 - 0.48) \times 10^{-1}$	$(1.96 \pm 0.01 + 0.34 - 0.11) \times 10^{-1}$
	1.0-1.5	$(8.28 \pm 0.04 + 2.46 - 2.37) \times 10^{-2}$	$(3.14 \pm 0.03 + 1.70 - 1.73) \times 10^{-2}$	$(7.69 \pm 0.06 + 1.12 - 0.39) \times 10^{-2}$
	1.5-2.0	$(3.79 \pm 0.02 + 1.08 - 0.90) \times 10^{-2}$	$(1.05 \pm 0.01 + 0.70 - 0.66) \times 10^{-2}$	$(2.95 \pm 0.03 + 0.70 - 0.15) \times 10^{-2}$
	2.0-2.5	$(1.47 \pm 0.01 + 0.52 - 0.24) \times 10^{-2}$	$(2.90 \pm 0.08 + 2.97 - 1.90) \times 10^{-3}$	$(9.38 \pm 0.16 + 4.41 - 0.20) \times 10^{-3}$
	2.5-3.0	$(5.60 \pm 0.06 + 1.27 - 0.72) \times 10^{-3}$	$(9.27 \pm 0.42 + 7.91 - 5.83) \times 10^{-4}$	$(3.00 \pm 0.09 + 0.93 - 0.12) \times 10^{-3}$
	3.0-4.0	$(3.23 \pm 0.05 + 0.43 - 0.42) \times 10^{-3}$	$(4.87 \pm 0.30 + 3.04 - 3.11) \times 10^{-4}$	$(1.33 \pm 0.06 + 0.12 - 0.11) \times 10^{-3}$
	4.0-5.0	$(6.46 \pm 0.18 + 0.63 - 0.66) \times 10^{-4}$	$(1.06 \pm 0.12 + 0.43 - 0.46) \times 10^{-4}$	$(2.20 \pm 0.24 + 0.32 - 0.32) \times 10^{-4}$
	5.0-7.0	$(2.37 \pm 0.11 + 0.27 - 0.26) \times 10^{-4}$	$(4.54 \pm 0.76 + 1.68 - 1.67) \times 10^{-5}$	$(7.67 \pm 1.50 + 1.98 - 1.96) \times 10^{-5}$
	7.0-10.0	$(2.43 \pm 0.26 + 0.43 - 0.43) \times 10^{-5}$	—	—
40-60%	0.4-1.0	$(1.57 \pm 0.01 + 0.43 - 0.35) \times 10^{-1}$	$(7.52 \pm 0.07 + 2.84 - 2.55) \times 10^{-2}$	$(1.09 \pm 0.01 + 0.19 - 0.06) \times 10^{-1}$
	1.0-1.5	$(5.78 \pm 0.04 + 1.59 - 1.21) \times 10^{-2}$	$(2.24 \pm 0.03 + 1.03 - 0.89) \times 10^{-2}$	$(4.03 \pm 0.06 + 0.92 - 0.21) \times 10^{-2}$
	1.5-2.0	$(2.66 \pm 0.02 + 0.49 - 0.44) \times 10^{-2}$	$(8.80 \pm 0.15 + 3.32 - 3.26) \times 10^{-3}$	$(1.54 \pm 0.03 + 0.29 - 0.08) \times 10^{-2}$
	2.0-2.5	$(1.12 \pm 0.01 + 0.14 - 0.14) \times 10^{-2}$	$(3.43 \pm 0.08 + 1.02 - 1.04) \times 10^{-3}$	$(5.74 \pm 0.15 + 0.42 - 0.31) \times 10^{-3}$
	2.5-3.0	$(4.45 \pm 0.06 + 0.52 - 0.48) \times 10^{-3}$	$(1.27 \pm 0.04 + 0.36 - 0.35) \times 10^{-3}$	$(1.74 \pm 0.08 + 0.19 - 0.14) \times 10^{-3}$
	3.0-4.0	$(2.77 \pm 0.05 + 0.24 - 0.22) \times 10^{-3}$	$(8.14 \pm 0.31 + 1.64 - 1.60) \times 10^{-4}$	$(9.52 \pm 0.61 + 1.01 - 0.86) \times 10^{-4}$
	4.0-5.0	$(6.79 \pm 0.19 + 0.46 - 0.48) \times 10^{-4}$	$(2.04 \pm 0.13 + 0.29 - 0.30) \times 10^{-4}$	$(2.08 \pm 0.24 + 0.33 - 0.33) \times 10^{-4}$
	5.0-7.0	$(2.86 \pm 0.12 + 0.25 - 0.25) \times 10^{-4}$	$(1.05 \pm 0.08 + 0.14 - 0.15) \times 10^{-4}$	$(6.83 \pm 1.55 + 2.10 - 2.11) \times 10^{-5}$
	7.0-10.0	$(2.62 \pm 0.31 + 0.48 - 0.47) \times 10^{-5}$	—	—
60-92%	0.4-1.0	$(1.15 \pm 0.01 + 0.18 - 0.17) \times 10^{-1}$	$(6.03 \pm 0.07 + 1.17 - 1.15) \times 10^{-2}$	$(6.27 \pm 0.12 + 1.08 - 0.50) \times 10^{-2}$
	1.0-1.5	$(4.28 \pm 0.04 + 0.66 - 0.49) \times 10^{-2}$	$(1.99 \pm 0.03 + 0.40 - 0.36) \times 10^{-2}$	$(2.29 \pm 0.05 + 0.49 - 0.11) \times 10^{-2}$
	1.5-2.0	$(1.94 \pm 0.02 + 0.19 - 0.18) \times 10^{-2}$	$(8.25 \pm 0.15 + 1.31 - 1.28) \times 10^{-3}$	$(8.72 \pm 0.29 + 0.74 - 0.47) \times 10^{-3}$
	2.0-2.5	$(8.45 \pm 0.12 + 0.53 - 0.57) \times 10^{-3}$	$(3.65 \pm 0.08 + 0.37 - 0.41) \times 10^{-3}$	$(3.44 \pm 0.15 + 0.26 - 0.21) \times 10^{-3}$
	2.5-3.0	$(3.63 \pm 0.07 + 0.23 - 0.26) \times 10^{-3}$	$(1.48 \pm 0.04 + 0.15 - 0.17) \times 10^{-3}$	$(1.12 \pm 0.08 + 0.12 - 0.13) \times 10^{-3}$
	3.0-4.0	$(2.52 \pm 0.05 + 0.14 - 0.15) \times 10^{-3}$	$(9.76 \pm 0.35 + 0.87 - 0.97) \times 10^{-4}$	$(5.75 \pm 0.64 + 0.91 - 0.93) \times 10^{-4}$
	4.0-5.0	$(6.63 \pm 0.23 + 0.44 - 0.46) \times 10^{-4}$	$(2.63 \pm 0.16 + 0.25 - 0.28) \times 10^{-4}$	$(1.25 \pm 0.27 + 0.36 - 0.36) \times 10^{-4}$
	5.0-7.0	$(3.35 \pm 0.16 + 0.21 - 0.21) \times 10^{-4}$	$(1.79 \pm 0.11 + 0.11 - 0.11) \times 10^{-4}$	$(1.17 \pm 0.18 + 0.22 - 0.21) \times 10^{-4}$
	7.0-10.0	$(2.90 \pm 0.41 + 0.55 - 0.55) \times 10^{-5}$	—	—
p+p	0.4-1.0	$(1.02 \pm 0.01 + 0.15 - 0.01) \times 10^{-1}$	$(6.24 \pm 0.05 + 0.77 - 0.05) \times 10^{-2}$	$(5.14 \pm 0.08 + 1.55 - 0.10) \times 10^{-2}$
	1.0-1.5	$(4.00 \pm 0.03 + 0.28 - 0.04) \times 10^{-2}$	$(2.04 \pm 0.02 + 0.14 - 0.02) \times 10^{-2}$	$(1.69 \pm 0.03 + 0.28 - 0.04) \times 10^{-2}$
	1.5-2.0	$(1.78 \pm 0.02 + 0.04 - 0.02) \times 10^{-2}$	$(8.64 \pm 0.11 + 0.18 - 0.10) \times 10^{-3}$	$(6.28 \pm 0.17 + 0.36 - 0.20) \times 10^{-3}$
	2.0-2.5	$(8.20 \pm 0.09 + 0.10 - 0.10) \times 10^{-3}$	$(3.81 \pm 0.06 + 0.05 - 0.05) \times 10^{-3}$	$(2.85 \pm 0.09 + 0.10 - 0.10) \times 10^{-3}$
	2.5-3.0	$(3.54 \pm 0.06 + 0.06 - 0.06) \times 10^{-3}$	$(1.71 \pm 0.04 + 0.03 - 0.03) \times 10^{-3}$	$(1.06 \pm 0.06 + 0.06 - 0.06) \times 10^{-3}$
	3.0-4.0	$(2.64 \pm 0.05 + 0.04 - 0.04) \times 10^{-3}$	$(1.33 \pm 0.03 + 0.02 - 0.02) \times 10^{-3}$	$(7.99 \pm 0.43 + 0.43 - 0.43) \times 10^{-4}$
	4.0-5.0	$(6.94 \pm 0.22 + 0.17 - 0.17) \times 10^{-4}$	$(4.17 \pm 0.17 + 0.08 - 0.08) \times 10^{-4}$	$(1.81 \pm 0.18 + 0.17 - 0.17) \times 10^{-4}$
	5.0-7.0	$(3.64 \pm 0.16 + 0.10 - 0.10) \times 10^{-4}$	$(2.23 \pm 0.13 + 0.05 - 0.05) \times 10^{-4}$	$(7.22 \pm 1.12 + 0.96 - 0.96) \times 10^{-5}$
	7.0-10.0	$(3.76 \pm 0.52 + 0.17 - 0.17) \times 10^{-5}$	—	—

TABLE XV: Per-trigger yield in various NR, HR and SR for $3.0 < p_T^a < 4.0$ GeV/c. They are bases for Fig. 12-14 and Fig. 18-20. The systematic uncertainties due to the single particle efficiency are not included ($\sim 10\%$).

$3.0 < p_T^a < 4.0 \text{ GeV}/c$				
$p_T^b \text{ (GeV}/c)$	$\int_{ \Delta\phi <\pi/3, \text{NR}} d\Delta\phi \left(\frac{1}{N^a} \frac{dN^{ab}}{d\Delta\phi} \right)$ Yield \pm Stat. +Sys. -Sys.	$\int_{ \Delta\phi-\pi <\pi/6, \text{HR}} d\Delta\phi \left(\frac{1}{N^a} \frac{dN^{ab}}{d\Delta\phi} \right)$ Yield \pm Stat. +Sys. -Sys.	$\int_{\pi/6< \Delta\phi-\pi <\pi/3, \text{SR}} d\Delta\phi \left(\frac{1}{N^a} \frac{dN^{ab}}{d\Delta\phi} \right)$ Yield \pm Stat. +Sys. -Sys.	
0-20%	0.4-1.0	$(2.45 \pm 0.04 + 0.98 - 0.31) \times 10^{-1}$	$(1.62 \pm 0.02 + 0.54 - 0.26) \times 10^{-1}$	$(3.23 \pm 0.05 + 0.89 - 0.08) \times 10^{-1}$
	1.0-1.5	$(1.09 \pm 0.02 + 0.26 - 0.14) \times 10^{-1}$	$(3.90 \pm 0.10 + 1.51 - 1.02) \times 10^{-2}$	$(1.10 \pm 0.02 + 0.22 - 0.03) \times 10^{-1}$
	1.5-2.0	$(5.98 \pm 0.08 + 0.72 - 0.60) \times 10^{-2}$	$(1.19 \pm 0.05 + 0.46 - 0.42) \times 10^{-2}$	$(4.32 \pm 0.11 + 0.48 - 0.17) \times 10^{-2}$
	2.0-2.5	$(2.52 \pm 0.04 + 0.28 - 0.20) \times 10^{-2}$	$(2.40 \pm 0.27 + 1.68 - 1.40) \times 10^{-3}$	$(1.25 \pm 0.06 + 0.22 - 0.08) \times 10^{-2}$
	2.5-3.0	$(9.96 \pm 0.22 + 1.09 - 0.59) \times 10^{-3}$	$(8.44 \pm 1.43 + 6.18 - 4.04) \times 10^{-4}$	$(3.62 \pm 0.30 + 0.94 - 0.40) \times 10^{-3}$
	3.0-4.0	$(6.71 \pm 0.16 + 0.36 - 0.37) \times 10^{-3}$	$(5.07 \pm 1.02 + 2.20 - 2.29) \times 10^{-4}$	$(1.91 \pm 0.21 + 0.28 - 0.28) \times 10^{-3}$
	4.0-5.0	$(1.49 \pm 0.06 + 0.12 - 0.12) \times 10^{-3}$	$(1.65 \pm 0.40 + 0.62 - 0.63) \times 10^{-4}$	$(1.54 \pm 0.83 + 1.09 - 1.09) \times 10^{-4}$
	5.0-7.0	$(6.45 \pm 0.42 + 0.75 - 0.75) \times 10^{-4}$	$(6.18 \pm 2.70 + 3.82 - 3.85) \times 10^{-5}$	$(3.51 \pm 5.43 + 7.28 - 7.28) \times 10^{-5}$
7.0-10.0	$(1.03 \pm 0.10 + 0.16 - 0.16) \times 10^{-4}$	—	—	
20-40%	0.4-1.0	$(2.53 \pm 0.03 + 0.85 - 0.65) \times 10^{-1}$	$(1.58 \pm 0.02 + 0.54 - 0.48) \times 10^{-1}$	$(2.61 \pm 0.04 + 0.56 - 0.09) \times 10^{-1}$
	1.0-1.5	$(9.94 \pm 0.13 + 2.78 - 2.44) \times 10^{-2}$	$(3.83 \pm 0.09 + 1.84 - 1.78) \times 10^{-2}$	$(8.70 \pm 0.18 + 1.63 - 0.45) \times 10^{-2}$
	1.5-2.0	$(5.19 \pm 0.07 + 1.40 - 0.87) \times 10^{-2}$	$(1.34 \pm 0.05 + 0.84 - 0.65) \times 10^{-2}$	$(3.59 \pm 0.09 + 1.11 - 0.16) \times 10^{-2}$
	2.0-2.5	$(2.17 \pm 0.04 + 0.29 - 0.31) \times 10^{-2}$	$(3.48 \pm 0.24 + 2.09 - 2.25) \times 10^{-3}$	$(1.01 \pm 0.05 + 0.08 - 0.08) \times 10^{-2}$
	2.5-3.0	$(9.74 \pm 0.20 + 1.15 - 1.22) \times 10^{-3}$	$(1.44 \pm 0.13 + 0.78 - 0.84) \times 10^{-3}$	$(3.24 \pm 0.26 + 0.48 - 0.49) \times 10^{-3}$
	3.0-4.0	$(6.81 \pm 0.15 + 0.54 - 0.57) \times 10^{-3}$	$(1.14 \pm 0.09 + 0.36 - 0.38) \times 10^{-3}$	$(1.95 \pm 0.19 + 0.28 - 0.29) \times 10^{-3}$
	4.0-5.0	$(1.64 \pm 0.06 + 0.11 - 0.11) \times 10^{-3}$	$(3.34 \pm 0.38 + 0.63 - 0.65) \times 10^{-4}$	$(2.87 \pm 0.74 + 0.95 - 0.95) \times 10^{-4}$
	5.0-7.0	$(9.23 \pm 0.38 + 0.64 - 0.64) \times 10^{-4}$	$(2.46 \pm 0.24 + 0.33 - 0.34) \times 10^{-4}$	$(1.95 \pm 0.46 + 0.60 - 0.60) \times 10^{-4}$
7.0-10.0	$(8.37 \pm 0.94 + 1.38 - 1.38) \times 10^{-5}$	—	—	
40-60%	0.4-1.0	$(1.92 \pm 0.03 + 0.42 - 0.35) \times 10^{-1}$	$(1.19 \pm 0.02 + 0.27 - 0.25) \times 10^{-1}$	$(1.68 \pm 0.04 + 0.27 - 0.07) \times 10^{-1}$
	1.0-1.5	$(7.55 \pm 0.12 + 1.28 - 1.22) \times 10^{-2}$	$(3.33 \pm 0.08 + 0.88 - 0.89) \times 10^{-2}$	$(5.51 \pm 0.16 + 0.65 - 0.29) \times 10^{-2}$
	1.5-2.0	$(3.77 \pm 0.07 + 0.51 - 0.45) \times 10^{-2}$	$(1.23 \pm 0.04 + 0.35 - 0.33) \times 10^{-2}$	$(1.85 \pm 0.09 + 0.23 - 0.13) \times 10^{-2}$
	2.0-2.5	$(1.53 \pm 0.03 + 0.17 - 0.14) \times 10^{-2}$	$(4.58 \pm 0.23 + 1.13 - 1.01) \times 10^{-3}$	$(5.31 \pm 0.45 + 0.75 - 0.59) \times 10^{-3}$
	2.5-3.0	$(8.39 \pm 0.19 + 0.60 - 0.63) \times 10^{-3}$	$(2.29 \pm 0.13 + 0.39 - 0.42) \times 10^{-3}$	$(2.47 \pm 0.25 + 0.35 - 0.36) \times 10^{-3}$
	3.0-4.0	$(6.41 \pm 0.15 + 0.34 - 0.35) \times 10^{-3}$	$(1.71 \pm 0.10 + 0.21 - 0.21) \times 10^{-3}$	$(1.63 \pm 0.18 + 0.25 - 0.25) \times 10^{-3}$
	4.0-5.0	$(1.85 \pm 0.06 + 0.10 - 0.11) \times 10^{-3}$	$(4.38 \pm 0.40 + 0.55 - 0.56) \times 10^{-4}$	$(2.47 \pm 0.73 + 0.98 - 0.98) \times 10^{-4}$
	5.0-7.0	$(8.94 \pm 0.44 + 0.76 - 0.62) \times 10^{-4}$	$(3.37 \pm 0.29 + 0.38 - 0.32) \times 10^{-4}$	$(9.01 \pm 4.82 + 7.43 - 6.20) \times 10^{-5}$
7.0-10.0	$(1.16 \pm 0.12 + 0.11 - 0.11) \times 10^{-4}$	—	—	
60-92%	0.4-1.0	$(1.37 \pm 0.03 + 0.28 - 0.16) \times 10^{-1}$	$(8.92 \pm 0.19 + 1.54 - 1.11) \times 10^{-2}$	$(9.12 \pm 0.36 + 2.42 - 0.53) \times 10^{-2}$
	1.0-1.5	$(6.04 \pm 0.12 + 1.01 - 0.47) \times 10^{-2}$	$(3.38 \pm 0.08 + 0.56 - 0.35) \times 10^{-2}$	$(3.58 \pm 0.16 + 0.91 - 0.20) \times 10^{-2}$
	1.5-2.0	$(2.91 \pm 0.06 + 0.22 - 0.21) \times 10^{-2}$	$(1.32 \pm 0.04 + 0.15 - 0.15) \times 10^{-2}$	$(1.13 \pm 0.08 + 0.13 - 0.11) \times 10^{-2}$
	2.0-2.5	$(1.40 \pm 0.04 + 0.09 - 0.09) \times 10^{-2}$	$(5.61 \pm 0.24 + 0.54 - 0.58) \times 10^{-3}$	$(3.77 \pm 0.44 + 0.60 - 0.59) \times 10^{-3}$
	2.5-3.0	$(6.90 \pm 0.21 + 0.40 - 0.42) \times 10^{-3}$	$(2.63 \pm 0.14 + 0.23 - 0.25) \times 10^{-3}$	$(1.42 \pm 0.25 + 0.32 - 0.33) \times 10^{-3}$
	3.0-4.0	$(6.11 \pm 0.17 + 0.25 - 0.26) \times 10^{-3}$	$(2.56 \pm 0.12 + 0.14 - 0.14) \times 10^{-3}$	$(1.18 \pm 0.18 + 0.23 - 0.23) \times 10^{-3}$
	4.0-5.0	$(2.11 \pm 0.09 + 0.09 - 0.10) \times 10^{-3}$	$(7.84 \pm 0.56 + 0.49 - 0.50) \times 10^{-4}$	$(3.02 \pm 0.74 + 0.92 - 0.92) \times 10^{-4}$
	5.0-7.0	$(1.16 \pm 0.07 + 0.07 - 0.07) \times 10^{-3}$	$(6.24 \pm 0.48 + 0.35 - 0.36) \times 10^{-4}$	$(1.31 \pm 0.50 + 0.69 - 0.69) \times 10^{-4}$
7.0-10.0	$(6.14 \pm 1.86 + 2.90 - 2.90) \times 10^{-5}$	—	—	
p+p	0.4-1.0	$(1.26 \pm 0.02 + 0.12 - 0.03) \times 10^{-1}$	$(9.18 \pm 0.14 + 0.61 - 0.14) \times 10^{-2}$	$(7.19 \pm 0.22 + 1.22 - 0.29) \times 10^{-2}$
	1.0-1.5	$(5.74 \pm 0.08 + 0.16 - 0.11) \times 10^{-2}$	$(3.46 \pm 0.06 + 0.08 - 0.05) \times 10^{-2}$	$(2.53 \pm 0.09 + 0.16 - 0.11) \times 10^{-2}$
	1.5-2.0	$(2.88 \pm 0.05 + 0.06 - 0.06) \times 10^{-2}$	$(1.45 \pm 0.04 + 0.03 - 0.03) \times 10^{-2}$	$(9.08 \pm 0.52 + 0.60 - 0.58) \times 10^{-3}$
	2.0-2.5	$(1.49 \pm 0.03 + 0.03 - 0.03) \times 10^{-2}$	$(7.73 \pm 0.24 + 0.16 - 0.16) \times 10^{-3}$	$(4.52 \pm 0.31 + 0.31 - 0.31) \times 10^{-3}$
	2.5-3.0	$(7.59 \pm 0.21 + 0.18 - 0.18) \times 10^{-3}$	$(3.53 \pm 0.15 + 0.09 - 0.09) \times 10^{-3}$	$(2.00 \pm 0.18 + 0.18 - 0.18) \times 10^{-3}$
	3.0-4.0	$(6.35 \pm 0.18 + 0.13 - 0.13) \times 10^{-3}$	$(3.64 \pm 0.14 + 0.06 - 0.06) \times 10^{-3}$	$(1.74 \pm 0.15 + 0.13 - 0.13) \times 10^{-3}$
	4.0-5.0	$(1.76 \pm 0.09 + 0.02 - 0.02) \times 10^{-3}$	$(1.16 \pm 0.08 + 0.01 - 0.01) \times 10^{-3}$	$(4.20 \pm 0.70 + 0.16 - 0.16) \times 10^{-4}$
	5.0-7.0	$(1.15 \pm 0.08 + 0.01 - 0.01) \times 10^{-3}$	$(7.15 \pm 0.65 + 0.05 - 0.05) \times 10^{-4}$	$(1.88 \pm 0.44 + 0.10 - 0.10) \times 10^{-4}$
7.0-10.0	$(1.15 \pm 0.26 + 0.03 - 0.03) \times 10^{-4}$	—	—	

TABLE XVI: Per-trigger yield in various NR, HR and SR for $4.0 < p_T^a < 5.0$ GeV/c. They are bases for Fig. 12-14 and Fig. 18-20. The systematic uncertainties due to the single particle efficiency are not included ($\sim 10\%$).

$4.0 < p_T^a < 5.0$ GeV/c

p_T^b (GeV/c)	$\int_{ \Delta\phi <\pi/3,\text{NR}} d\Delta\phi \left(\frac{1}{N^a} \frac{dN^{ab}}{d\Delta\phi} \right)$ Yield \pm Stat. +Sys. -Sys.	$\int_{ \Delta\phi-\pi <\pi/6,\text{HR}} d\Delta\phi \left(\frac{1}{N^a} \frac{dN^{ab}}{d\Delta\phi} \right)$ Yield \pm Stat. +Sys. -Sys.	$\int_{\pi/6< \Delta\phi-\pi <\pi/3,\text{SR}} d\Delta\phi \left(\frac{1}{N^a} \frac{dN^{ab}}{d\Delta\phi} \right)$ Yield \pm Stat. +Sys. -Sys.	
0-20%	0.4-1.0	$(2.50 \pm 0.11 + 0.48 - 0.36) \times 10^{-1}$	$(1.96 \pm 0.07 + 0.32 - 0.27) \times 10^{-1}$	$(3.66 \pm 0.14 + 0.33 - 0.19) \times 10^{-1}$
	1.0-1.5	$(1.19 \pm 0.05 + 0.17 - 0.17) \times 10^{-1}$	$(4.84 \pm 0.31 + 1.14 - 1.17) \times 10^{-2}$	$(9.97 \pm 0.63 + 1.03 - 0.87) \times 10^{-2}$
	1.5-2.0	$(6.58 \pm 0.24 + 0.66 - 0.58) \times 10^{-2}$	$(1.55 \pm 0.16 + 0.43 - 0.38) \times 10^{-2}$	$(3.76 \pm 0.34 + 0.46 - 0.44) \times 10^{-2}$
	2.0-2.5	$(3.09 \pm 0.12 + 0.30 - 0.25) \times 10^{-2}$	$(2.70 \pm 0.81 + 1.76 - 1.51) \times 10^{-3}$	$(1.04 \pm 0.17 + 0.25 - 0.22) \times 10^{-2}$
	2.5-3.0	$(1.42 \pm 0.07 + 0.13 - 0.13) \times 10^{-2}$	$(7.43 \pm 4.34 + 7.21 - 7.37) \times 10^{-4}$	$(3.35 \pm 0.92 + 1.19 - 1.19) \times 10^{-3}$
	3.0-4.0	$(1.25 \pm 0.05 + 0.09 - 0.09) \times 10^{-2}$	$(1.72 \pm 0.31 + 0.47 - 0.48) \times 10^{-3}$	$(1.76 \pm 0.63 + 0.84 - 0.84) \times 10^{-3}$
	4.0-5.0	$(3.63 \pm 0.20 + 0.33 - 0.33) \times 10^{-3}$	$(5.04 \pm 1.24 + 1.65 - 1.65) \times 10^{-4}$	$(7.50 \pm 2.55 + 3.26 - 3.26) \times 10^{-4}$
	5.0-7.0	$(2.35 \pm 0.13 + 0.22 - 0.22) \times 10^{-3}$	$(5.18 \pm 0.85 + 1.09 - 1.09) \times 10^{-4}$	$(4.59 \pm 1.64 + 2.16 - 2.16) \times 10^{-4}$
7.0-10.0	$(2.63 \pm 0.35 + 0.46 - 0.46) \times 10^{-4}$	—	—	
20-40%	0.4-1.0	$(2.27 \pm 0.08 + 1.03 - 0.45) \times 10^{-1}$	$(1.64 \pm 0.06 + 0.60 - 0.36) \times 10^{-1}$	$(2.80 \pm 0.11 + 0.84 - 0.17) \times 10^{-1}$
	1.0-1.5	$(1.03 \pm 0.04 + 0.26 - 0.16) \times 10^{-1}$	$(3.86 \pm 0.24 + 1.70 - 1.29) \times 10^{-2}$	$(9.10 \pm 0.48 + 1.58 - 0.71) \times 10^{-2}$
	1.5-2.0	$(5.59 \pm 0.19 + 0.97 - 0.66) \times 10^{-2}$	$(1.59 \pm 0.13 + 0.63 - 0.51) \times 10^{-2}$	$(3.33 \pm 0.26 + 0.66 - 0.34) \times 10^{-2}$
	2.0-2.5	$(2.80 \pm 0.10 + 0.31 - 0.33) \times 10^{-2}$	$(5.10 \pm 0.65 + 2.08 - 2.21) \times 10^{-3}$	$(1.01 \pm 0.13 + 0.18 - 0.18) \times 10^{-2}$
	2.5-3.0	$(1.36 \pm 0.05 + 0.12 - 0.13) \times 10^{-2}$	$(1.95 \pm 0.35 + 0.77 - 0.80) \times 10^{-3}$	$(3.69 \pm 0.72 + 0.94 - 0.94) \times 10^{-3}$
	3.0-4.0	$(1.20 \pm 0.04 + 0.08 - 0.08) \times 10^{-2}$	$(2.51 \pm 0.26 + 0.47 - 0.48) \times 10^{-3}$	$(2.78 \pm 0.51 + 0.69 - 0.69) \times 10^{-3}$
	4.0-5.0	$(4.12 \pm 0.17 + 0.26 - 0.26) \times 10^{-3}$	$(1.31 \pm 0.11 + 0.14 - 0.14) \times 10^{-3}$	$(9.06 \pm 2.02 + 2.57 - 2.57) \times 10^{-4}$
	5.0-7.0	$(2.16 \pm 0.12 + 0.18 - 0.18) \times 10^{-3}$	$(4.57 \pm 0.75 + 0.91 - 0.91) \times 10^{-4}$	$< 2.4 \times 10^{-4}$
7.0-10.0	$(2.75 \pm 0.34 + 0.18 - 0.18) \times 10^{-4}$	—	—	
40-60%	0.4-1.0	$(2.06 \pm 0.07 + 0.54 - 0.34) \times 10^{-1}$	$(1.43 \pm 0.05 + 0.31 - 0.23) \times 10^{-1}$	$(1.83 \pm 0.09 + 0.46 - 0.13) \times 10^{-1}$
	1.0-1.5	$(9.80 \pm 0.32 + 1.36 - 1.36) \times 10^{-2}$	$(4.63 \pm 0.21 + 0.90 - 0.92) \times 10^{-2}$	$(6.99 \pm 0.42 + 0.68 - 0.65) \times 10^{-2}$
	1.5-2.0	$(5.18 \pm 0.17 + 0.46 - 0.49) \times 10^{-2}$	$(1.90 \pm 0.11 + 0.30 - 0.32) \times 10^{-2}$	$(2.41 \pm 0.22 + 0.30 - 0.30) \times 10^{-2}$
	2.0-2.5	$(2.44 \pm 0.09 + 0.21 - 0.21) \times 10^{-2}$	$(7.52 \pm 0.59 + 1.23 - 1.30) \times 10^{-3}$	$(8.59 \pm 1.17 + 1.56 - 1.57) \times 10^{-3}$
	2.5-3.0	$(1.47 \pm 0.05 + 0.09 - 0.10) \times 10^{-2}$	$(4.59 \pm 0.34 + 0.52 - 0.54) \times 10^{-3}$	$(3.79 \pm 0.64 + 0.83 - 0.83) \times 10^{-3}$
	3.0-4.0	$(1.08 \pm 0.04 + 0.07 - 0.07) \times 10^{-2}$	$(2.43 \pm 0.26 + 0.36 - 0.36) \times 10^{-3}$	$(9.42 \pm 4.72 + 6.40 - 6.41) \times 10^{-4}$
	4.0-5.0	$(3.31 \pm 0.18 + 0.26 - 0.25) \times 10^{-3}$	$(1.21 \pm 0.12 + 0.13 - 0.13) \times 10^{-3}$	$(5.53 \pm 1.90 + 2.62 - 2.52) \times 10^{-4}$
	5.0-7.0	$(2.41 \pm 0.14 + 0.14 - 0.14) \times 10^{-3}$	$(8.88 \pm 0.95 + 0.69 - 0.69) \times 10^{-4}$	$(3.75 \pm 1.33 + 1.36 - 1.36) \times 10^{-4}$
7.0-10.0	$(1.97 \pm 0.43 + 0.43 - 0.43) \times 10^{-4}$	—	—	
60-92%	0.4-1.0	$(1.38 \pm 0.07 + 0.52 - 0.24) \times 10^{-1}$	$(1.06 \pm 0.05 + 0.28 - 0.16) \times 10^{-1}$	$(9.05 \pm 0.89 + 4.79 - 1.23) \times 10^{-2}$
	1.0-1.5	$(6.25 \pm 0.30 + 0.77 - 0.70) \times 10^{-2}$	$(3.76 \pm 0.21 + 0.49 - 0.48) \times 10^{-2}$	$(3.28 \pm 0.39 + 0.60 - 0.51) \times 10^{-2}$
	1.5-2.0	$(3.91 \pm 0.17 + 0.34 - 0.32) \times 10^{-2}$	$(1.61 \pm 0.11 + 0.21 - 0.20) \times 10^{-2}$	$(1.43 \pm 0.21 + 0.28 - 0.27) \times 10^{-2}$
	2.0-2.5	$(1.96 \pm 0.09 + 0.17 - 0.15) \times 10^{-2}$	$(8.35 \pm 0.63 + 0.94 - 0.86) \times 10^{-3}$	$(4.30 \pm 1.10 + 1.43 - 1.40) \times 10^{-3}$
	2.5-3.0	$(1.15 \pm 0.06 + 0.09 - 0.09) \times 10^{-2}$	$(4.51 \pm 0.39 + 0.46 - 0.49) \times 10^{-3}$	$(2.32 \pm 0.65 + 0.82 - 0.82) \times 10^{-3}$
	3.0-4.0	$(1.23 \pm 0.05 + 0.06 - 0.06) \times 10^{-2}$	$(4.62 \pm 0.34 + 0.29 - 0.30) \times 10^{-3}$	$(1.90 \pm 0.45 + 0.55 - 0.55) \times 10^{-3}$
	4.0-5.0	$(3.84 \pm 0.27 + 0.24 - 0.23) \times 10^{-3}$	$(1.54 \pm 0.18 + 0.12 - 0.11) \times 10^{-3}$	$(6.30 \pm 2.14 + 2.36 - 2.28) \times 10^{-4}$
	5.0-7.0	$(2.33 \pm 0.22 + 0.14 - 0.14) \times 10^{-3}$	$(1.44 \pm 0.18 + 0.07 - 0.07) \times 10^{-3}$	$(1.35 \pm 1.32 + 1.37 - 1.37) \times 10^{-4}$
7.0-10.0	$(2.85 \pm 0.83 + 0.27 - 0.27) \times 10^{-4}$	—	—	
p+p	0.4-1.0	$(1.67 \pm 0.05 + 0.16 - 0.07) \times 10^{-1}$	$(1.21 \pm 0.03 + 0.08 - 0.03) \times 10^{-1}$	$(9.66 \pm 0.52 + 1.62 - 0.65) \times 10^{-2}$
	1.0-1.5	$(7.94 \pm 0.21 + 0.25 - 0.25) \times 10^{-2}$	$(4.83 \pm 0.16 + 0.12 - 0.12) \times 10^{-2}$	$(2.79 \pm 0.22 + 0.25 - 0.25) \times 10^{-2}$
	1.5-2.0	$(4.16 \pm 0.13 + 0.13 - 0.13) \times 10^{-2}$	$(2.34 \pm 0.10 + 0.06 - 0.06) \times 10^{-2}$	$(1.50 \pm 0.12 + 0.13 - 0.13) \times 10^{-2}$
	2.0-2.5	$(2.21 \pm 0.09 + 0.06 - 0.06) \times 10^{-2}$	$(1.36 \pm 0.07 + 0.03 - 0.03) \times 10^{-2}$	$(7.09 \pm 0.76 + 0.65 - 0.65) \times 10^{-3}$
	2.5-3.0	$(1.16 \pm 0.06 + 0.04 - 0.04) \times 10^{-2}$	$(7.13 \pm 0.48 + 0.21 - 0.21) \times 10^{-3}$	$(2.12 \pm 0.41 + 0.41 - 0.41) \times 10^{-3}$
	3.0-4.0	$(1.05 \pm 0.05 + 0.03 - 0.03) \times 10^{-2}$	$(6.29 \pm 0.44 + 0.13 - 0.13) \times 10^{-3}$	$(2.46 \pm 0.41 + 0.27 - 0.27) \times 10^{-3}$
	4.0-5.0	$(4.30 \pm 0.33 + 0.07 - 0.07) \times 10^{-3}$	$(2.53 \pm 0.27 + 0.04 - 0.04) \times 10^{-3}$	$(9.06 \pm 1.99 + 0.73 - 0.73) \times 10^{-4}$
	5.0-7.0	$(2.39 \pm 0.28 + 0.03 - 0.03) \times 10^{-3}$	$(1.55 \pm 0.24 + 0.01 - 0.01) \times 10^{-3}$	$(4.20 \pm 1.29 + 0.29 - 0.29) \times 10^{-4}$
7.0-10.0	$(2.29 \pm 1.06 + 0.03 - 0.03) \times 10^{-4}$	—	—	

TABLE XVII: Per-trigger yield in various NR, HR and SR for $5.0 < p_T^a < 10.0$ GeV/c. They are bases for Fig. 12-14 and Fig. 18-20. The systematic uncertainties due to the single particle efficiency are not included ($\sim 10\%$).

5.0 < p _T ^a < 10.0 GeV/c				
p _T ^b (GeV/c)	∫ _{Δφ <π/3,NR} dΔφ ($\frac{1}{N^a} \frac{dN^{ab}}{d\Delta\phi}$)	∫ _{Δφ-π <π/6,HR} dΔφ ($\frac{1}{N^a} \frac{dN^{ab}}{d\Delta\phi}$)	∫ _{π/6< Δφ-π <π/3,SR} dΔφ ($\frac{1}{N^a} \frac{dN^{ab}}{d\Delta\phi}$)	
0-20%	0.4-1.0	(2.04 ± 0.25 + 0.51 - 0.52) × 10 ⁻¹	(2.25 ± 0.17 + 0.31 - 0.32) × 10 ⁻¹	(3.36 ± 0.32 + 0.45 - 0.45) × 10 ⁻¹
	1.0-1.5	(1.17 ± 0.11 + 0.35 - 0.21) × 10 ⁻¹	(5.59 ± 0.72 + 1.85 - 1.24) × 10 ⁻²	(1.22 ± 0.15 + 0.34 - 0.20) × 10 ⁻¹
	1.5-2.0	(8.45 ± 0.57 + 1.22 - 1.23) × 10 ⁻²	(1.34 ± 0.38 + 0.68 - 0.69) × 10 ⁻²	(4.14 ± 0.78 + 1.05 - 1.05) × 10 ⁻²
	2.0-2.5	(3.05 ± 0.29 + 0.56 - 0.57) × 10 ⁻²	(5.22 ± 1.93 + 2.97 - 3.02) × 10 ⁻³	(1.61 ± 0.40 + 0.53 - 0.53) × 10 ⁻²
	2.5-3.0	(2.27 ± 0.16 + 0.28 - 0.28) × 10 ⁻²	(2.67 ± 1.02 + 1.42 - 1.43) × 10 ⁻³	(8.61 ± 2.15 + 2.74 - 2.74) × 10 ⁻³
	3.0-4.0	(2.22 ± 0.12 + 0.20 - 0.20) × 10 ⁻²	(4.01 ± 0.74 + 1.01 - 1.01) × 10 ⁻³	(3.22 ± 1.46 + 1.98 - 1.98) × 10 ⁻³
	4.0-5.0	(8.47 ± 0.52 + 0.72 - 0.72) × 10 ⁻³	(2.09 ± 0.32 + 0.36 - 0.36) × 10 ⁻³	(1.68 ± 0.60 + 0.72 - 0.72) × 10 ⁻³
	5.0-7.0	(5.76 ± 0.36 + 0.48 - 0.48) × 10 ⁻³	(1.40 ± 0.22 + 0.24 - 0.24) × 10 ⁻³	(7.07 ± 3.55 + 4.85 - 4.85) × 10 ⁻⁴
7.0-10.0	(8.24 ± 1.30 + 2.29 - 2.29) × 10 ⁻⁴	-	-	
20-40%	0.4-1.0	(2.53 ± 0.21 + 0.98 - 0.56) × 10 ⁻¹	(2.15 ± 0.14 + 0.57 - 0.39) × 10 ⁻¹	(3.22 ± 0.27 + 0.81 - 0.36) × 10 ⁻¹
	1.0-1.5	(1.11 ± 0.09 + 0.23 - 0.21) × 10 ⁻¹	(3.78 ± 0.60 + 1.52 - 1.41) × 10 ⁻²	(9.89 ± 1.21 + 1.65 - 1.61) × 10 ⁻²
	1.5-2.0	(6.54 ± 0.48 + 1.32 - 1.37) × 10 ⁻²	(1.08 ± 0.32 + 0.80 - 0.84) × 10 ⁻²	(9.71 ± 6.42 + 9.33 - 9.41) × 10 ⁻³
	2.0-2.5	(3.40 ± 0.25 + 0.53 - 0.47) × 10 ⁻²	(4.62 ± 1.66 + 3.02 - 2.66) × 10 ⁻³	(6.14 ± 3.33 + 4.50 - 4.41) × 10 ⁻³
	2.5-3.0	(2.14 ± 0.14 + 0.30 - 0.23) × 10 ⁻²	(5.97 ± 0.93 + 1.53 - 1.18) × 10 ⁻³	(5.03 ± 1.83 + 3.03 - 2.32) × 10 ⁻³
	3.0-4.0	(2.14 ± 0.11 + 0.17 - 0.17) × 10 ⁻²	(6.53 ± 0.72 + 0.88 - 0.89) × 10 ⁻³	(3.25 ± 1.28 + 1.67 - 1.67) × 10 ⁻³
	4.0-5.0	(8.49 ± 0.52 + 0.70 - 0.70) × 10 ⁻³	(2.57 ± 0.33 + 0.35 - 0.35) × 10 ⁻³	(8.49 ± 4.99 + 6.95 - 6.95) × 10 ⁻⁴
	5.0-7.0	(6.82 ± 0.42 + 0.42 - 0.42) × 10 ⁻³	(2.12 ± 0.25 + 0.21 - 0.21) × 10 ⁻³	(6.51 ± 3.10 + 4.23 - 4.23) × 10 ⁻⁴
7.0-10.0	(7.18 ± 1.78 + 1.93 - 1.93) × 10 ⁻⁴	-	-	
40-60%	0.4-1.0	(2.07 ± 0.19 + 0.44 - 0.45) × 10 ⁻¹	(1.57 ± 0.13 + 0.27 - 0.28) × 10 ⁻¹	(1.92 ± 0.24 + 0.32 - 0.32) × 10 ⁻¹
	1.0-1.5	(1.15 ± 0.08 + 0.55 - 0.16) × 10 ⁻¹	(6.97 ± 0.55 + 2.79 - 0.94) × 10 ⁻²	(6.58 ± 1.07 + 5.46 - 1.43) × 10 ⁻²
	1.5-2.0	(6.80 ± 0.44 + 0.90 - 0.93) × 10 ⁻²	(2.40 ± 0.29 + 0.51 - 0.53) × 10 ⁻²	(1.59 ± 0.57 + 0.77 - 0.77) × 10 ⁻²
	2.0-2.5	(3.61 ± 0.23 + 0.41 - 0.42) × 10 ⁻²	(1.59 ± 0.16 + 0.22 - 0.22) × 10 ⁻²	(1.37 ± 0.30 + 0.38 - 0.39) × 10 ⁻²
	2.5-3.0	(1.96 ± 0.14 + 0.22 - 0.22) × 10 ⁻²	(5.31 ± 0.89 + 1.14 - 1.15) × 10 ⁻³	(1.59 ± 1.64 + 2.18 - 2.18) × 10 ⁻³
	3.0-4.0	(2.18 ± 0.12 + 0.15 - 0.15) × 10 ⁻²	(7.76 ± 0.79 + 0.78 - 0.78) × 10 ⁻³	(3.08 ± 1.25 + 1.52 - 1.52) × 10 ⁻³
	4.0-5.0	(8.98 ± 0.63 + 0.58 - 0.58) × 10 ⁻³	(3.18 ± 0.41 + 0.29 - 0.29) × 10 ⁻³	(1.24 ± 0.51 + 0.58 - 0.58) × 10 ⁻³
	5.0-7.0	(6.63 ± 0.91 + 0.25 - 0.25) × 10 ⁻³	(1.87 ± 0.32 + 0.13 - 0.13) × 10 ⁻³	(7.67 ± 4.11 + 2.54 - 2.54) × 10 ⁻⁴
7.0-10.0	(6.68 ± 2.15 + 0.77 - 0.77) × 10 ⁻⁴	-	-	
60-92%	0.4-1.0	(1.84 ± 0.18 + 0.44 - 0.39) × 10 ⁻¹	(1.48 ± 0.13 + 0.25 - 0.24) × 10 ⁻¹	(1.62 ± 0.23 + 0.39 - 0.30) × 10 ⁻¹
	1.0-1.5	(1.20 ± 0.08 + 0.19 - 0.15) × 10 ⁻¹	(7.38 ± 0.55 + 1.02 - 0.90) × 10 ⁻²	(5.49 ± 0.99 + 1.74 - 1.26) × 10 ⁻²
	1.5-2.0	(5.16 ± 0.43 + 0.71 - 0.69) × 10 ⁻²	(3.01 ± 0.31 + 0.38 - 0.37) × 10 ⁻²	(2.17 ± 0.55 + 0.70 - 0.67) × 10 ⁻²
	2.0-2.5	(3.69 ± 0.26 + 0.35 - 0.35) × 10 ⁻²	(1.95 ± 0.18 + 0.18 - 0.19) × 10 ⁻²	(1.11 ± 0.29 + 0.33 - 0.33) × 10 ⁻²
	2.5-3.0	(2.21 ± 0.17 + 0.20 - 0.20) × 10 ⁻²	(9.52 ± 1.14 + 1.00 - 1.01) × 10 ⁻³	(5.62 ± 1.56 + 1.95 - 1.95) × 10 ⁻³
	3.0-4.0	(1.91 ± 0.16 + 0.16 - 0.16) × 10 ⁻²	(1.17 ± 0.12 + 0.08 - 0.08) × 10 ⁻²	(1.77 ± 1.09 + 1.60 - 1.60) × 10 ⁻³
	4.0-5.0	(8.40 ± 1.03 + 0.72 - 0.72) × 10 ⁻³	(5.09 ± 0.88 + 0.36 - 0.36) × 10 ⁻³	(4.09 ± 7.55 + 7.19 - 7.19) × 10 ⁻⁴
	5.0-7.0	(8.14 ± 1.23 + 0.73 - 0.73) × 10 ⁻³	(3.07 ± 0.73 + 0.36 - 0.36) × 10 ⁻³	< 7.3 × 10 ⁻⁴
7.0-10.0	(7.30 ± 3.43 + 0.33 - 0.33) × 10 ⁻⁴	-	-	
p+p	0.4-1.0	(1.89 ± 0.03 + 0.06 - 0.03) × 10 ⁻¹	(1.51 ± 0.02 + 0.03 - 0.02) × 10 ⁻¹	(9.83 ± 0.28 + 0.65 - 0.35) × 10 ⁻²
	1.0-1.5	(9.88 ± 0.13 + 0.14 - 0.14) × 10 ⁻²	(6.74 ± 0.10 + 0.07 - 0.07) × 10 ⁻²	(3.47 ± 0.12 + 0.14 - 0.14) × 10 ⁻²
	1.5-2.0	(5.93 ± 0.08 + 0.08 - 0.08) × 10 ⁻²	(3.79 ± 0.07 + 0.04 - 0.04) × 10 ⁻²	(1.54 ± 0.07 + 0.08 - 0.08) × 10 ⁻²
	2.0-2.5	(3.58 ± 0.06 + 0.04 - 0.04) × 10 ⁻²	(2.12 ± 0.05 + 0.02 - 0.02) × 10 ⁻²	(7.89 ± 0.44 + 0.39 - 0.39) × 10 ⁻³
	2.5-3.0	(2.08 ± 0.05 + 0.02 - 0.02) × 10 ⁻²	(1.29 ± 0.04 + 0.01 - 0.01) × 10 ⁻²	(4.68 ± 0.29 + 0.25 - 0.25) × 10 ⁻³
	3.0-4.0	(2.24 ± 0.05 + 0.02 - 0.02) × 10 ⁻²	(1.27 ± 0.04 + 0.01 - 0.01) × 10 ⁻²	(3.58 ± 0.24 + 0.23 - 0.23) × 10 ⁻³
	4.0-5.0	(9.09 ± 0.39 + 0.06 - 0.06) × 10 ⁻³	(5.76 ± 0.28 + 0.03 - 0.03) × 10 ⁻³	(1.25 ± 0.13 + 0.06 - 0.06) × 10 ⁻³
	5.0-7.0	(6.47 ± 0.47 + 0.02 - 0.02) × 10 ⁻³	(3.87 ± 0.29 + 0.01 - 0.01) × 10 ⁻³	(7.23 ± 0.99 + 0.21 - 0.21) × 10 ⁻⁴
7.0-10.0	(1.25 ± 0.44 + 0.00 - 0.00) × 10 ⁻³	-	-	

TABLE XVIII: Pair suppression factor J_{AA} in NR and HR for various $p_T^a \otimes p_T^b$ bins. The systematic uncertainties due to the single particle efficiency are not included ($\sim 17\%$).

$2.0 < p_T^a < 3.0 \text{ GeV}/c$				$3.0 < p_T^a < 4.0 \text{ GeV}/c$			
$\langle p_T^b \rangle \text{ GeV}/c$	$J_{AA}(\Delta\phi < \pi/3)$	$J_{AA}(\Delta\phi - \pi < \pi/6)$	$\langle p_T^b \rangle \text{ GeV}/c$	$J_{AA}(\Delta\phi < \pi/3)$	$J_{AA}(\Delta\phi - \pi < \pi/6)$		
0-20%	0.63	$1.34 \pm 0.01 + 0.52 - 0.25$	$1.17 \pm 0.01 + 0.46 - 0.30$	0.63	$0.88 \pm 0.02 + 0.36 - 0.11$	$0.80 \pm 0.02 + 0.27 - 0.13$	
	1.20	$1.39 \pm 0.01 + 0.32 - 0.22$	$1.03 \pm 0.01 + 0.37 - 0.31$	1.20	$0.87 \pm 0.02 + 0.21 - 0.11$	$0.51 \pm 0.02 + 0.20 - 0.13$	
	1.70	$1.53 \pm 0.02 + 0.24 - 0.19$	$0.83 \pm 0.02 + 0.30 - 0.27$	1.70	$0.94 \pm 0.02 + 0.12 - 0.10$	$0.37 \pm 0.02 + 0.14 - 0.13$	
	2.20	$1.33 \pm 0.02 + 0.17 - 0.13$	$0.52 \pm 0.02 + 0.22 - 0.20$	2.20	$0.77 \pm 0.02 + 0.09 - 0.06$	$0.14 \pm 0.02 + 0.10 - 0.08$	
	2.70	$1.08 \pm 0.02 + 0.17 - 0.09$	$0.25 \pm 0.02 + 0.20 - 0.14$	2.70	$0.60 \pm 0.02 + 0.07 - 0.04$	$0.11 \pm 0.02 + 0.08 - 0.05$	
	3.34	$0.78 \pm 0.02 + 0.08 - 0.05$	$0.14 \pm 0.01 + 0.09 - 0.07$	3.34	$0.48 \pm 0.02 + 0.03 - 0.03$	$0.06 \pm 0.01 + 0.03 - 0.03$	
	4.38	$0.50 \pm 0.02 + 0.04 - 0.04$	$0.06 \pm 0.02 + 0.04 - 0.04$	4.38	$0.39 \pm 0.03 + 0.03 - 0.03$	$0.06 \pm 0.02 + 0.02 - 0.02$	
	5.75	$0.30 \pm 0.02 + 0.04 - 0.04$	$0.02 \pm 0.02 + 0.04 - 0.03$	5.75	$0.25 \pm 0.02 + 0.03 - 0.03$	$0.04 \pm 0.02 + 0.02 - 0.02$	
	8.18	$0.20 \pm 0.05 + 0.11 - 0.08$	—	8.17	$0.41 \pm 0.10 + 0.06 - 0.06$	—	
20-40%	0.63	$1.67 \pm 0.01 + 0.58 - 0.49$	$1.34 \pm 0.01 + 0.61 - 0.58$	0.63	$1.24 \pm 0.02 + 0.43 - 0.32$	$1.06 \pm 0.02 + 0.37 - 0.32$	
	1.20	$1.55 \pm 0.01 + 0.47 - 0.44$	$1.15 \pm 0.01 + 0.63 - 0.64$	1.20	$1.07 \pm 0.02 + 0.30 - 0.26$	$0.68 \pm 0.02 + 0.33 - 0.32$	
	1.70	$1.60 \pm 0.02 + 0.46 - 0.38$	$0.91 \pm 0.02 + 0.61 - 0.57$	1.70	$1.11 \pm 0.02 + 0.30 - 0.19$	$0.57 \pm 0.02 + 0.36 - 0.28$	
	2.20	$1.35 \pm 0.02 + 0.47 - 0.22$	$0.57 \pm 0.02 + 0.58 - 0.37$	2.20	$0.90 \pm 0.02 + 0.12 - 0.13$	$0.28 \pm 0.02 + 0.17 - 0.18$	
	2.70	$1.19 \pm 0.02 + 0.27 - 0.15$	$0.41 \pm 0.02 + 0.35 - 0.26$	2.70	$0.79 \pm 0.03 + 0.09 - 0.10$	$0.25 \pm 0.02 + 0.14 - 0.15$	
	3.34	$0.92 \pm 0.02 + 0.12 - 0.12$	$0.27 \pm 0.02 + 0.17 - 0.18$	3.34	$0.66 \pm 0.02 + 0.05 - 0.06$	$0.19 \pm 0.02 + 0.06 - 0.06$	
	4.38	$0.70 \pm 0.03 + 0.07 - 0.07$	$0.19 \pm 0.02 + 0.08 - 0.08$	4.38	$0.57 \pm 0.04 + 0.04 - 0.04$	$0.18 \pm 0.02 + 0.03 - 0.03$	
	5.70	$0.49 \pm 0.03 + 0.06 - 0.06$	$0.15 \pm 0.03 + 0.06 - 0.06$	5.70	$0.49 \pm 0.04 + 0.03 - 0.03$	$0.21 \pm 0.03 + 0.03 - 0.03$	
	8.10	$0.48 \pm 0.08 + 0.09 - 0.09$	—	8.15	$0.45 \pm 0.11 + 0.08 - 0.08$	—	
40-60%	0.63	$1.34 \pm 0.01 + 0.42 - 0.30$	$1.05 \pm 0.01 + 0.42 - 0.36$	0.63	$1.18 \pm 0.03 + 0.28 - 0.22$	$1.00 \pm 0.02 + 0.24 - 0.21$	
	1.20	$1.26 \pm 0.01 + 0.36 - 0.26$	$0.95 \pm 0.01 + 0.45 - 0.38$	1.20	$1.02 \pm 0.02 + 0.17 - 0.17$	$0.75 \pm 0.02 + 0.20 - 0.20$	
	1.70	$1.30 \pm 0.02 + 0.24 - 0.22$	$0.89 \pm 0.02 + 0.33 - 0.33$	1.70	$1.02 \pm 0.03 + 0.14 - 0.12$	$0.66 \pm 0.03 + 0.19 - 0.18$	
	2.20	$1.19 \pm 0.02 + 0.15 - 0.15$	$0.78 \pm 0.02 + 0.23 - 0.24$	2.20	$0.80 \pm 0.02 + 0.09 - 0.07$	$0.46 \pm 0.03 + 0.11 - 0.10$	
	2.71	$1.10 \pm 0.02 + 0.13 - 0.12$	$0.65 \pm 0.03 + 0.18 - 0.18$	2.71	$0.86 \pm 0.03 + 0.06 - 0.07$	$0.50 \pm 0.04 + 0.09 - 0.09$	
	3.35	$0.91 \pm 0.02 + 0.08 - 0.07$	$0.53 \pm 0.02 + 0.11 - 0.10$	3.36	$0.78 \pm 0.03 + 0.04 - 0.05$	$0.36 \pm 0.03 + 0.04 - 0.05$	
	4.38	$0.85 \pm 0.04 + 0.06 - 0.06$	$0.43 \pm 0.03 + 0.06 - 0.06$	4.39	$0.81 \pm 0.05 + 0.05 - 0.05$	$0.29 \pm 0.03 + 0.04 - 0.04$	
	5.70	$0.68 \pm 0.04 + 0.06 - 0.06$	$0.41 \pm 0.04 + 0.06 - 0.06$	5.70	$0.60 \pm 0.05 + 0.05 - 0.04$	$0.37 \pm 0.05 + 0.04 - 0.03$	
	8.12	$0.61 \pm 0.11 + 0.11 - 0.11$	—	8.07	$0.79 \pm 0.19 + 0.08 - 0.08$	—	
60-92%	0.63	$1.04 \pm 0.01 + 0.23 - 0.15$	$0.89 \pm 0.01 + 0.20 - 0.17$	0.63	$0.95 \pm 0.02 + 0.21 - 0.11$	$0.85 \pm 0.02 + 0.16 - 0.11$	
	1.20	$0.98 \pm 0.01 + 0.17 - 0.11$	$0.89 \pm 0.01 + 0.19 - 0.16$	1.20	$0.92 \pm 0.02 + 0.16 - 0.07$	$0.86 \pm 0.03 + 0.14 - 0.09$	
	1.70	$1.00 \pm 0.01 + 0.10 - 0.09$	$0.87 \pm 0.02 + 0.14 - 0.14$	1.71	$0.89 \pm 0.03 + 0.07 - 0.07$	$0.80 \pm 0.03 + 0.09 - 0.09$	
	2.21	$0.94 \pm 0.02 + 0.06 - 0.06$	$0.88 \pm 0.02 + 0.09 - 0.10$	2.21	$0.82 \pm 0.03 + 0.05 - 0.06$	$0.64 \pm 0.03 + 0.06 - 0.07$	
	2.71	$0.94 \pm 0.02 + 0.06 - 0.07$	$0.79 \pm 0.03 + 0.08 - 0.09$	2.71	$0.80 \pm 0.03 + 0.05 - 0.05$	$0.65 \pm 0.04 + 0.06 - 0.06$	
	3.36	$0.87 \pm 0.02 + 0.05 - 0.05$	$0.67 \pm 0.03 + 0.06 - 0.07$	3.38	$0.84 \pm 0.03 + 0.04 - 0.04$	$0.62 \pm 0.04 + 0.03 - 0.04$	
	4.39	$0.87 \pm 0.04 + 0.06 - 0.06$	$0.58 \pm 0.04 + 0.06 - 0.06$	4.40	$1.05 \pm 0.07 + 0.05 - 0.05$	$0.59 \pm 0.06 + 0.04 - 0.04$	
	5.70	$0.84 \pm 0.05 + 0.06 - 0.06$	$0.74 \pm 0.06 + 0.05 - 0.05$	5.73	$0.89 \pm 0.08 + 0.05 - 0.05$	$0.77 \pm 0.09 + 0.04 - 0.04$	
	8.01	$0.71 \pm 0.14 + 0.14 - 0.14$	—	8.01	$0.47 \pm 0.18 + 0.22 - 0.22$	—	

TABLE XIX: Pair suppression factor J_{AA} in NR and HR for various $p_T^a \otimes p_T^b$ bins. The systematic uncertainties due to the single particle efficiency are not included ($\sim 17\%$).

$4.0 < p_T^a < 5.0 \text{ GeV}/c$				$5.0 < p_T^a < 10.0 \text{ GeV}/c$			
$\langle p_T^b \rangle \text{ GeV}/c$	$J_{AA}(\Delta\phi < \pi/3)$	$J_{AA}(\Delta\phi - \pi < \pi/6)$	$\langle p_T^b \rangle \text{ GeV}/c$	$J_{AA}(\Delta\phi < \pi/3)$	$J_{AA}(\Delta\phi - \pi < \pi/6)$		
0-20%	0.63	$0.48 \pm 0.02 + 0.10 - 0.07$	$0.52 \pm 0.02 + 0.09 - 0.07$	0.63	$0.28 \pm 0.04 + 0.07 - 0.07$	$0.39 \pm 0.03 + 0.05 - 0.06$	
	1.20	$0.47 \pm 0.02 + 0.07 - 0.07$	$0.32 \pm 0.02 + 0.08 - 0.08$	1.20	$0.31 \pm 0.03 + 0.09 - 0.06$	$0.21 \pm 0.03 + 0.07 - 0.05$	
	1.70	$0.50 \pm 0.02 + 0.05 - 0.05$	$0.21 \pm 0.02 + 0.06 - 0.05$	1.70	$0.37 \pm 0.03 + 0.05 - 0.05$	$0.09 \pm 0.03 + 0.05 - 0.05$	
	2.20	$0.44 \pm 0.02 + 0.05 - 0.04$	$0.06 \pm 0.02 + 0.04 - 0.04$	2.20	$0.22 \pm 0.02 + 0.04 - 0.04$	$0.06 \pm 0.02 + 0.04 - 0.04$	
	2.70	$0.39 \pm 0.03 + 0.04 - 0.04$	$0.03 \pm 0.02 + 0.03 - 0.03$	2.70	$0.28 \pm 0.02 + 0.03 - 0.03$	$0.05 \pm 0.02 + 0.03 - 0.03$	
	3.34	$0.38 \pm 0.02 + 0.03 - 0.03$	$0.09 \pm 0.02 + 0.02 - 0.02$	3.35	$0.26 \pm 0.01 + 0.02 - 0.02$	$0.08 \pm 0.02 + 0.02 - 0.02$	
	4.38	$0.27 \pm 0.03 + 0.02 - 0.02$	$0.06 \pm 0.02 + 0.02 - 0.02$	4.40	$0.24 \pm 0.02 + 0.02 - 0.02$	$0.09 \pm 0.02 + 0.02 - 0.02$	
	5.76	$0.31 \pm 0.04 + 0.03 - 0.03$	$0.11 \pm 0.02 + 0.02 - 0.02$	5.79	$0.23 \pm 0.02 + 0.02 - 0.02$	$0.09 \pm 0.02 + 0.02 - 0.02$	
	8.12	$0.37 \pm 0.18 + 0.06 - 0.06$	—	8.03	$0.17 \pm 0.07 + 0.05 - 0.05$	—	
20-40%	0.63	$0.67 \pm 0.03 + 0.31 - 0.13$	$0.67 \pm 0.03 + 0.25 - 0.15$	0.63	$0.57 \pm 0.05 + 0.22 - 0.13$	$0.60 \pm 0.04 + 0.16 - 0.11$	
	1.20	$0.63 \pm 0.03 + 0.16 - 0.10$	$0.39 \pm 0.03 + 0.17 - 0.13$	1.20	$0.47 \pm 0.04 + 0.10 - 0.09$	$0.24 \pm 0.04 + 0.10 - 0.09$	
	1.70	$0.66 \pm 0.03 + 0.12 - 0.08$	$0.33 \pm 0.03 + 0.13 - 0.11$	1.70	$0.47 \pm 0.04 + 0.09 - 0.10$	$0.12 \pm 0.04 + 0.09 - 0.09$	
	2.20	$0.62 \pm 0.03 + 0.07 - 0.07$	$0.18 \pm 0.03 + 0.07 - 0.08$	2.20	$0.40 \pm 0.03 + 0.06 - 0.06$	$0.09 \pm 0.03 + 0.06 - 0.05$	
	2.71	$0.57 \pm 0.04 + 0.06 - 0.06$	$0.13 \pm 0.03 + 0.05 - 0.06$	2.71	$0.43 \pm 0.03 + 0.06 - 0.05$	$0.20 \pm 0.03 + 0.05 - 0.04$	
	3.35	$0.56 \pm 0.03 + 0.04 - 0.04$	$0.19 \pm 0.02 + 0.04 - 0.04$	3.36	$0.40 \pm 0.02 + 0.03 - 0.03$	$0.22 \pm 0.02 + 0.03 - 0.03$	
	4.39	$0.47 \pm 0.04 + 0.03 - 0.03$	$0.25 \pm 0.03 + 0.03 - 0.03$	4.40	$0.40 \pm 0.03 + 0.03 - 0.03$	$0.19 \pm 0.03 + 0.03 - 0.03$	
	5.72	$0.44 \pm 0.06 + 0.04 - 0.04$	$0.14 \pm 0.03 + 0.03 - 0.03$	5.77	$0.45 \pm 0.04 + 0.03 - 0.03$	$0.23 \pm 0.03 + 0.02 - 0.02$	
	8.06	$0.59 \pm 0.28 + 0.04 - 0.04$	—	8.00	$0.24 \pm 0.10 + 0.07 - 0.07$	—	
40-60%	0.63	$0.85 \pm 0.04 + 0.24 - 0.14$	$0.81 \pm 0.04 + 0.19 - 0.14$	0.63	$0.62 \pm 0.06 + 0.13 - 0.14$	$0.58 \pm 0.05 + 0.10 - 0.11$	
	1.20	$0.85 \pm 0.04 + 0.12 - 0.12$	$0.66 \pm 0.04 + 0.13 - 0.13$	1.20	$0.66 \pm 0.05 + 0.31 - 0.09$	$0.58 \pm 0.05 + 0.23 - 0.08$	
	1.70	$0.85 \pm 0.04 + 0.08 - 0.08$	$0.56 \pm 0.04 + 0.09 - 0.10$	1.70	$0.65 \pm 0.04 + 0.09 - 0.09$	$0.36 \pm 0.04 + 0.08 - 0.08$	
	2.21	$0.76 \pm 0.04 + 0.07 - 0.07$	$0.38 \pm 0.04 + 0.06 - 0.07$	2.21	$0.57 \pm 0.04 + 0.07 - 0.07$	$0.42 \pm 0.04 + 0.06 - 0.06$	
	2.71	$0.87 \pm 0.05 + 0.06 - 0.06$	$0.44 \pm 0.04 + 0.05 - 0.05$	2.71	$0.53 \pm 0.04 + 0.06 - 0.06$	$0.23 \pm 0.04 + 0.05 - 0.05$	
	3.37	$0.70 \pm 0.04 + 0.05 - 0.05$	$0.26 \pm 0.03 + 0.04 - 0.04$	3.39	$0.55 \pm 0.03 + 0.04 - 0.04$	$0.35 \pm 0.04 + 0.03 - 0.03$	
	4.40	$0.53 \pm 0.05 + 0.04 - 0.04$	$0.33 \pm 0.05 + 0.04 - 0.03$	4.41	$0.56 \pm 0.05 + 0.04 - 0.04$	$0.31 \pm 0.04 + 0.03 - 0.03$	
	5.71	$0.69 \pm 0.09 + 0.04 - 0.04$	$0.39 \pm 0.07 + 0.03 - 0.03$	5.74	$0.58 \pm 0.09 + 0.02 - 0.02$	$0.27 \pm 0.05 + 0.02 - 0.02$	
	8.13	$0.59 \pm 0.30 + 0.13 - 0.13$	—	8.09	$0.30 \pm 0.14 + 0.03 - 0.03$	—	
60-92%	0.63	$0.70 \pm 0.04 + 0.27 - 0.13$	$0.75 \pm 0.04 + 0.20 - 0.12$	0.63	$0.70 \pm 0.07 + 0.17 - 0.15$	$0.70 \pm 0.06 + 0.12 - 0.11$	
	1.20	$0.67 \pm 0.04 + 0.08 - 0.08$	$0.66 \pm 0.04 + 0.09 - 0.09$	1.21	$0.86 \pm 0.06 + 0.14 - 0.11$	$0.78 \pm 0.06 + 0.11 - 0.10$	
	1.71	$0.80 \pm 0.04 + 0.07 - 0.07$	$0.58 \pm 0.05 + 0.08 - 0.08$	1.71	$0.62 \pm 0.05 + 0.09 - 0.08$	$0.57 \pm 0.06 + 0.07 - 0.07$	
	2.21	$0.75 \pm 0.05 + 0.07 - 0.06$	$0.52 \pm 0.05 + 0.06 - 0.05$	2.22	$0.74 \pm 0.05 + 0.07 - 0.07$	$0.65 \pm 0.06 + 0.06 - 0.06$	
	2.71	$0.84 \pm 0.06 + 0.07 - 0.07$	$0.54 \pm 0.06 + 0.06 - 0.06$	2.72	$0.76 \pm 0.06 + 0.07 - 0.07$	$0.52 \pm 0.06 + 0.06 - 0.06$	
	3.39	$1.00 \pm 0.07 + 0.05 - 0.05$	$0.62 \pm 0.06 + 0.04 - 0.04$	3.38	$0.61 \pm 0.05 + 0.05 - 0.05$	$0.66 \pm 0.07 + 0.05 - 0.05$	
	4.42	$0.76 \pm 0.08 + 0.05 - 0.05$	$0.52 \pm 0.08 + 0.04 - 0.04$	4.41	$0.66 \pm 0.09 + 0.06 - 0.06$	$0.63 \pm 0.11 + 0.04 - 0.04$	
	5.74	$0.83 \pm 0.13 + 0.05 - 0.05$	$0.79 \pm 0.16 + 0.04 - 0.04$	5.79	$0.90 \pm 0.15 + 0.08 - 0.08$	$0.56 \pm 0.14 + 0.07 - 0.07$	
	7.99	$1.06 \pm 0.58 + 0.10 - 0.10$	—	8.10	$0.41 \pm 0.24 + 0.02 - 0.02$	—	

-
- [1] R. Baier, Y. L. Dokshitzer, A. H. Mueller, S. Peigne and D. Schiff, Nucl. Phys. B **484**, 265 (1997)
 - [2] M. Gyulassy, I. Vitev, X. N. Wang and B. W. Zhang, nucl-th/0302077;
 - [3] A. Kovner and U. A. Wiedemann, hep-ph/0304151.
 - [4] K. Adcox *et al.* [PHENIX Collaboration], Phys. Rev. Lett. **88**, 022301 (2002)
 - [5] S. S. Adler *et al.* [PHENIX Collaboration], Phys. Rev. Lett. **91**, 072301 (2003)
 - [6] J. Adams *et al.* [STAR Collaboration], Phys. Rev. Lett. **91**, 172302 (2003)
 - [7] S. S. Adler *et al.* [PHENIX Collaboration], Phys. Rev. C **69**, 034910 (2004)
 - [8] C. Adler *et al.* [STAR Collaboration], Phys. Rev. Lett. **90**, 082302 (2003)
 - [9] S. S. Adler *et al.* [PHENIX Collaboration], Phys. Rev. Lett. **96**, 202301 (2006)
 - [10] S. S. Adler *et al.* [PHENIX Collaboration], Phys. Rev. C **75**, 024909 (2007)
 - [11] B. I. Abelev *et al.* [STAR Collaboration], Phys. Rev. Lett. **97**, 152301 (2006)
 - [12] J. Adams *et al.* [STAR Collaboration], Phys. Rev. Lett. **97**, 162301 (2006)
 - [13] A. Adare *et al.* [PHENIX Collaboration], Phys. Rev. C **77**, 011901(R) (2008)
 - [14] T. Renk and K. J. Eskola, Phys. Rev. C **75**, 054910 (2007)
 - [15] A. Majumder, J. Phys. G **34**, S377 (2007)
 - [16] J. Adams *et al.* [STAR Collaboration], Phys. Rev. C **73**, 064907 (2006)
 - [17] J. Adams *et al.* [STAR Collaboration], Phys. Rev. Lett. **95**, 152301 (2005)
 - [18] S. S. Adler *et al.* [PHENIX Collaboration], Phys. Rev. Lett. **97**, 052301 (2006)
 - [19] A. Adare *et al.* [PHENIX Collaboration], Phys. Rev. Lett. **98**, 232302 (2007)
 - [20] J. Adams *et al.* [Star Collaboration], Phys. Rev. C **75**, 034901 (2007)
 - [21] S. A. Voloshin, Nucl. Phys. A **749**, 287 (2005)
 - [22] C. B. Chiu and R. C. Hwa, Phys. Rev. C **72**, 034903 (2005)
 - [23] N. Armesto, C. A. Salgado and U. A. Wiedemann, Phys. Rev. Lett. **93**, 242301 (2004)
 - [24] P. Romatschke, Phys. Rev. C **75**, 014901 (2007)
 - [25] A. Majumder, B. Muller and S. A. Bass, Phys. Rev. Lett. **99**, 042301 (2007)
 - [26] E. V. Shuryak, Phys. Rev. C **76**, 047901 (2007)
 - [27] C. Y. Wong, Phys. Rev. C **76**, 054908 (2007)
 - [28] V. S. Pantuev, arXiv:0710.1882 [hep-ph].
 - [29] C. Chiu and R. Hwa, Phys. Rev. C **74**, 064909 (2006)
 - [30] N. Armesto, C. A. Salgado and U. A. Wiedemann, Phys. Rev. C **72**, 064910 (2005)
 - [31] I. Vitev, Phys. Lett. B **630**, 78 (2005)
 - [32] A. D. Polosa and C. A. Salgado, Phys. Rev. C **75**, 041901 (2007)
 - [33] I. M. Dremin, JETP Lett. **30**, 140 (1979)
 - [34] V. Koch, A. Majumder and X. N. Wang, Phys. Rev. Lett. **96**, 172302 (2006)
 - [35] J. Casalderrey-Solana, E. V. Shuryak and D. Teaney, J. Phys. Conf. Ser. **27**, 22 (2005); hep-ph/0602183.
 - [36] H. Stoecker, Nucl. Phys. A **750**, 121 (2005);
 - [37] P. F. Kolb and R. Rapp, Phys. Rev. C **67**, 044903 (2003)
 - [38] D. Molnar and S. A. Voloshin, Phys. Rev. Lett. **91**, 092301 (2003)
 - [39] R. C. Hwa and C. B. Yang, Phys. Rev. C **70**, 024905 (2004)
 - [40] R. J. Fries, B. Muller, C. Nonaka and S. A. Bass, Phys. Rev. C **68**, 044902 (2003)
 - [41] V. Greco, C. M. Ko and P. Levai, Phys. Rev. Lett. **90**, 202302 (2003)
 - [42] R. J. Fries, S. A. Bass and B. Muller, Phys. Rev. Lett. **94**, 122301 (2005)
 - [43] S. Afanasiev *et al.* [PHENIX Collaboration], arXiv:0712.3033 [nucl-ex].
 - [44] S. S. Adler *et al.* [PHENIX Collaboration], Phys. Rev. D **74**, 072002 (2006)
 - [45] K. Adcox *et al.* [PHENIX Collaboration], Nucl. Instrum. Meth. A **499**, 469 (2003).
 - [46] A. Adare *et al.* [PHENIX Collaboration], Phys. Rev. Lett. **97**, 252002 (2006)
 - [47] K. Adcox *et al.* [PHENIX Collaboration], Nucl. Instrum. Meth. A **499**, 489 (2003).
 - [48] K. Adcox *et al.* [PHENIX Collaboration], Phys. Rev. Lett. **86**, 3500 (2001)
 - [49] K. Adcox *et al.* [PHENIX Collaboration], Phys. Rev. C **69**, 024904 (2004)
 - [50] S. S. Adler *et al.* [PHENIX Collaboration], Phys. Rev. C **73**, 054903 (2006)
 - [51] S. S. Adler *et al.* [PHENIX Collaboration], Phys. Rev. Lett. **95**, 202001 (2005)
 - [52] A. M. Poskanzer and S. A. Voloshin, Phys. Rev. C **58**, 1671 (1998)
 - [53] S. S. Adler *et al.* [PHENIX Collaboration], Phys. Rev. Lett. **91**, 182301 (2003)
 - [54] S. S. Adler *et al.* [PHENIX Collaboration], Phys. Rev. C **72**, 024901 (2005)
 - [55] N. Borghini, P. M. Dinh and J. Y. Ollitrault, Phys. Rev. C **64**, 054901 (2001)
 - [56] N. Borghini, P. M. Dinh and J. Y. Ollitrault, Phys. Rev. C **62**, 034902 (2000)
 - [57] M. Miller and R. Snellings, arXiv:nucl-ex/0312008.
 - [58] R. S. Bhalerao and J. Y. Ollitrault, Phys. Lett. B **641**, 260 (2006)
 - [59] S. Manly *et al.* [PHOBOS Collaboration], Nucl. Phys. A **774**, 523 (2006)
 - [60] X. I. Zhu, M. Bleicher and H. Stoecker, Phys. Rev. C **72**, 064911 (2005)
 - [61] J. Adams *et al.* [STAR Collaboration], Phys. Rev. Lett. **93**, 252301 (2004)
 - [62] B. Alver *et al.* [PHOBOS Collaboration], Int. J. Mod. Phys. E **16**, 3331 (2008)
 - [63] P. Sorensen [STAR Collaboration], J. Phys. G **34**, S897 (2007)
 - [64] A. A. Affolder *et al.* [CDF Collaboration], Phys. Rev. D **65**, 092002 (2002).
 - [65] D. E. Acosta *et al.* [CDF Collaboration], Phys. Rev. D **71**, 052002 (2005)
 - [66] T. Sjostrand, L. Lonnblad and S. Mrenna, arXiv:hep-ph/0108264.
 - [67] N. N. Ajitanand *et al.*, Phys. Rev. C **72**, 011902 (2005)
 - [68] S. S. Adler *et al.* Phys. Rev. C **71**, 051902 (2005)
 - [69] C. Loizides, Eur. Phys. J. C **49**, 339 (2007)

- [70] A. Adare *et al.* [PHENIX Collaboration], Phys. Lett. B **649**, 359 (2007)
- [71] Note that the pseudo-rapidity coverage of PHENIX is smaller than that used in STAR, thus the amount of ridge yield seen in PHENIX is also smaller. The projected near-side jet shape in $\Delta\phi$ may also depends on the pseudo-rapidity coverage.
- [72] T. Renk and J. Ruppert, Phys. Rev. C **73**, 011901 (2006)
- [73] J. F. Owens, E. Reya and M. Gluck, Phys. Rev. D **18**, 1501 (1978).
- [74] D. Teaney, J. Lauret and E. V. Shuryak, Phys. Rev. Lett. **86**, 4783 (2001)
- [75] P. Huovinen, Nucl. Phys. A **715**, 299 (2003)
- [76] J. Jia [PHENIX Collaboration], arXiv:nucl-ex/0703047.
- [77] H. Zhang, J. F. Owens, E. Wang and X. N. Wang, Phys. Rev. Lett. **98**, 212301 (2007), and private communications with authors.
- [78] M. Ploskon [CERES Collaboration], Nucl. Phys. A **783**, 527 (2007)
- [79] J. W. Cronin, H. J. Frisch, M. J. Shochet, J. P. Boymond, R. Mermod, P. A. Piroue and R. L. Sumner, Phys. Rev. D **11**, 3105 (1975).
- [80] C. A. Salgado and U. A. Wiedemann, Phys. Rev. Lett. **93**, 042301 (2004)
- [81] The condition of Eq. A6 can be violated by some experimental effects, such as ghost-pair tracking artifacts at small angles. We recover the result of Eq. A6 by applying pair cuts to remove such artifacts identically to same-event and mixed-event pairs. Pair cuts affect the integrands in the numerator and denominator of Eq. A10 equally and so leave the end result of Eq. A11 intact.
- [82] J. Jia [PHENIX Collaboration], Nucl. Phys. A **783**, 501 (2007)
- [83] B. B. Back *et al.*, Phys. Rev. Lett. **91**, 052303 (2003)
- [84] A. Adare *et al.* [PHENIX Collaboration], Phys. Rev. Lett. **98**, 162301 (2007)